Title
Solution-Processed Polymer and Perovskite Emitters for Novel Light Emitting Applications

Author
Chou, Shu-Yu

Publication Date
2017

Peer reviewed|Thesis/dissertation

UNIVERSITY OF CALIFORNIA

Los Angeles

Solution-Processed Polymer and Perovskite Emitters for Novel Light Emitting Applications

A dissertation submitted in partial satisfaction of the

requirements for the degree Doctor of Philosophy

in Materials Science and Engineering

by

Shu-Yu Chou

2017

ABSTRACT OF THE DISSERTATION

Solution-Processed Polymer and Perovskite Emitters

for Novel Light Emitting Applications

by

Shu-Yu Chou

Doctor of Philosophy in Materials Science and Engineering

University of California, Los Angeles, 2017

Professor Qibing Pei, Chair

According to recent research reports, the global market for display and lighting products is expected to grow to 169.17 billion USD by the year 2022. Display technologies include the light emitting diode (LED), liquid crystal display (LCD), organic light-emitting diode (OLED), quantum dot light emitting diode (QDLED), and electronic paper display (EPD), whereas LEDs have been the dominant lighting solution in the past two decades due to their long lifetime and use of non-hazardous materials. However, the growth in revenue for LED technology is predicted to slow down due to the advancement in OLED technology. OLEDs are known to be more energy efficient, have higher picture quality, and are more lightweight than LEDs. The bottleneck for OLEDs is their high production cost, which restrains it from the mass market. Fortunately, the development of conjugated polymer emitters shifts the manufacturing process from vacuum thermal evaporation to a solution processed methodology (i.e. ink-jet printing, roll-to-roll printing,

screen printing, etc.) which is much more cost-effective. The resulting OLED, also referred to as a polymer light emitting diode (PLED), shows enormous potential in the future of display technologies. Alongside the PLED, a new class of solution-processable emitters, the organometal halide perovskite, has also shown promising performance in lighting applications.

Despite their advantages, solution-processed emitters have also shown lower device performance when compared to thermal vapor evaporated OLEDs. Due to the limitation of solution-processed materials to withstand the solvent attack from advancing layers, solution-processed light emitting devices usually have overly simple structures; this results in poor device performance, which can be attributed to the imbalance of charge injection. This dissertation focuses on improving the efficiency and stability of light emitting devices based on conjugated polymer emitters and organometal halide perovskite emitters by employing novel device architectures. In addition, based on the beneficial characteristics of the perovskite and polymer blend film, multifunctional devices including light emitting touch-responsive devices and stretchable perovskite light emitting diodes are also demonstrated here.

To begin, a white conjugated polymer emitter was applied on a flexible silver nanowire (AgNW)-nanoparticle composite electrode, which resulted in a high out-coupling efficiency with a 95% enhancement. The flexible nanocomposite electrode was made with silver nanowire electrode and barium strontium titanate (BST) nanoparticles. The high out-coupling efficiency is achieved by replacing the ITO electrode with AgNW and by incorporating BST nanoparticles. Replacement of the ITO avoids light trapping inside the ITO caused by the mismatch of the refractive index, and the BST nanoparticles serve as the light scattering center that changed the path of the trapped light inside the substrate. The use of white conjugated polymer emitters on the light extraction substrate

demonstrates a means to fabricate high-efficiency flexible PLEDs with low fabrication cost. The white PLED achieved an external quantum efficiency of 27.3%.

The white conjugated polymer emitter was also used in a new type of optoelectronic device, the organic light emitting transistor (OLET). The white OLET combines both phosphorescent PLED and a transistor with a highly capacitive electrolyte dielectric material. By varying the gate potential, the luminance of the white OLET could be modified from 0.1 to 10,000 cd/m^2. This work reveals the possibility of achieving a cost-effective active matrix display based on solution processed materials and a simple device structure.

Next, the organometal halide perovskite emitter is introduced. In one application, it was used to demonstrate a light emitting touch-responsive device (LETD) which could provide instantaneous visualization of pressure mapping. The new LETD incorporates perovskite-polymer composite film as the emitter and a flexible AgNW-polyurethane as the top electrode. The perovskite LETD emitted an intense green luminescence when a local pressure was applied on the AgNW-polyurethane due to the formation of a Schottky contact between the AgNW and the perovskite emissive layer. The fabrication of the perovskite LETD was simple and based on an all-solution processed procedure.

I also used the perovskite emitter to achieve a stretchable perovskite light emitting diode (PeLED). The PeLED integrates an intrinsically stretchable perovskite emissive layer and a stretchable AgNW-polyurethane composite electrode. The stretchable perovskite emissive layer incorporates polyethylene glycol diacrylate (PEG), siliconized acrylate (PDMS) and methylammonium lead bromide. The PEG polymer helps to control the perovskite grain size and achieve a uniform perovskite grain film, while the PDMS polymer serves as the elastic connection that holds the film

together and provides stretchability to the film. The composite electrode, AgNW-polyurethane, provides high transparency, high conductivity, and high stretchability. With these elements combined, the PeLED could be stretched up to 60% strain while displaying a green electroluminescence.

Both conjugated polymer emitters and organometal halide perovskite emitters have been successfully demonstrated in various light applications as a proof of concept. A highly efficient PLED was achieved by employing nanoparticles in the substrate to scatter the trapped light into the air. In addition, by adjusting the three-terminal system to a suitable bias condition, the device luminance increased drastically due to the balance of electrons and holes in the OLET device. A robust and stable perovskite emissive layer was achieved by incorporating a PEO polymer, and an LETD was created that enables instantaneous pressure mapping. By adding an elastic polymer into the perovskite, a stretchable PeLED was also demonstrated. The results verify the potential of both conjugated polymer emitters and perovskite emitters for large-scale, low-cost lighting applications and for commercial use.

The dissertation of Shu-Yu Chou is approved.

Dwight Christopher Streit

Yunfeng Lu

Qibing Pei, Committee Chair

University of California, Los Angeles

2017

Dedicated to my parents,
Michael Chou and Jane Chen

my husband,
Sammy Ng

and my brother,
Brian Chou

for their unconditional love and support

Table of Contents

List of Figures

Acronyms

AFM	Atomic force microscope
AgNW	Silver nanowire
BST	Barium strontium titanate
CIE	Commission Internationale de l’Eclairage
CNT	Carbon nanotube
CV	Cyclic voltammetry
DMF	N,N-dimethylformamide
EInGa	Eutectic indium-gallium metal
EL	Electroluminescence
EML	Emissive layer
EQE	External quantum efficiency
ETL	Electron transporting layer
FDTD	Finite-difference time-domain
FET	Field-effect transistor
FWHM	Full width at half maximum

HOMO	Highest energy occupied molecular orbital
HTL	Hole transporting layer
IPA	2-Propanol alcohol
IQE	Internal quantum efficiency
ITO	Indium tin oxide
LED	Light emitting diode
LEP	Light emitting polymers
LETD	Light emitting touch-responsive device
LUMO	Lowest energy unoccupied molecular orbitals
OLED	Organic light emitting diode
OLET	Organic light emitting transistor
OSC	Organic semiconductor
PE	Polymer electrolyte
PEDOT:PSS	poly(3,4-ethylenedioxythiophene): poly(styrenesulfonate)
PeLED	Perovskite light emitting diode
PEO	Poly (ethylene oxide)
Pero	Perovskite

PET	Polyethylene terephthalate
PL	Photoluminescence
PLEC	Polymer light-emitting electrochemical cell
PLED	Polymer light emitting diode
PU	Polyurethane
QDLED	Quantum dot light emitting diode
RIML	Refractive index modulation layer
SCE	Saturated calomel electrode
SCP	Single component polymer
SEM	Scanning electron microscope
SMOLED	Small-molecule light emitting diode
V_g	Gate voltage

Acknowledgements

As I near the completion of my PhD degree, I can't help but recall my 5-year journey here at UCLA. I think the most apt description of these years would be a thrilling roller coaster ride – full of ups and downs. There were moments when I didn't know when the ride would end, and whether I was moving forward or backwards. But through it all, I am grateful to have had a group of amazing people surround me.

First and foremost, I would like to show my appreciation for my advisor, Professor Qibing Pei, for his continued support and guidance. Without his mentorship throughout these years, the completion of this dissertation would not be possible.

I would like to thank Professor Dwight Streit, Professor Jenn-Ming Yang, and Professor Yunfeng Lu for serving as members of my committee. Your expertise in your respective fields and your counsel were instrumental in my research.

My fellow associates from Professor Qibing Pei's group, Dr. Jiajie Liang, Dr. Fangchao Zhao, Dr. Rujun Ma, Dr. Xiaofeng Liu, Dr. Jiang Liu, Dr. Huibin Sun, Dr. Wei Hu, Dr. Chao Liu, Dr. Yan Xiong, Kwing Tong, Yunfei Li, and Hanhui Liu all deserve my deepest gratitude for their invaluable discussions and never-ending support in the lab. Your companionship and encouragement made even the latest nights in the lab seem like light-hearted banter amongst friends. I will most certainly miss you all.

I also want to acknowledge Dr. Adam Stieg, Dr. Sergey Prikhodko, and Dr. Ignacio Martini for their training on multiple characterization skills in Material Science. Your thoughtful instruction guided me through numerous challenges throughout my experiments.

Chapter Three is reprinted with permission from *Liu, J.; Chou, S.-Y.; Tong, K.; Luan, X.; Zhao, F.; Pei, Q. Study of White Electroluminescence from a Single-Component Polymer Using an Electrolyte-Gated Diode. J. Phys. Chem. C, 2017(121): 10112-10118.* Copyright 2017, American Chemical Society. Chapter Four is reprinted with permission from *Chou, S.-Y.; Ma, R.; Li, Y.; Zhao, F.; Tong, K.; Yu, Z.; Pei, Q. A Transparent Perovskite Light Emitting Touch-Responsive Device. Submitted for publication.* Prof. Qibing Pei is the direction for all projects involved in these segments.

To Dr. Dian Yu, Dr. Huier Gao, Dr. Zhi Ren, Dr. Jesse Ko, Po- Yuan Wang, Ya-Hsuan Chuang, Christine Young, and Chun-Han Lai, my wonderful colleagues who have become dear friends, I want to express my heartfelt gratefulness. Your camaraderie and console helped me through difficult times and having someone to relate to made this adventure that much easier and exciting.

S.C., C.L., A.L., R.Y., J.W., L.L., and J.E.: without you all, my life in Los Angeles would not have been the same. You reminded me how to enjoy the little things even when circumstances didn't allow it.

To S. Ng, thank you so much for keeping me motivated and encouraging me throughout all these years. Without your support and understandings, this dissertation would not be possible.

Lastly, I cannot thank my family enough – especially my parents, without their unconditional love and encouragement, I may have never made it to the end of this ride.

Vitas

2009 B.S., Biomedical and Chemical Engineering, Carnegie Mellon University, PA, USA

2010 M.S., Biomedical and Chemical Engineering, Yale University, CT, USA

2010-2012 Senior Process Engineer, AU Optronics, Taiwan

2012-2017 Ph.D Student at Department of Material Science & Engineering, University of California at Los Angeles, CA, USA

Publication

Chou, S.-Y.; Ma, R.; Li, Y.; Zhao, F.; Tong, K.; Yu, Z.; Pei, Q. A Transparent Perovskite Light Emitting Touch-Responsive Device. Submitted for publication.

Chou, S.-Y.; Li, Y.; Zhao, F.; Liu, C.; Pei, Q. A Stretchable Perovskite Light Emitting Diode based on Intrinsically Stretchable Perovskite Light Emitting Layer. In preparation.

Liu, J.*; Chou* (*co-first author), S.-Y.; Tong, K.; Luan, X.; Zhao, F.; Pei, Q. Study of White Electroluminescence from a Single-Component Polymer Using an Electrolyte-Gated Diode. J. Phys. Chem. C, 2017 (121): 10112-10118.

Li, L.; Liang, J.; Chou, S.-Y.; Zhu, X.; Niu, X.; Yu, Z.; Pei, Q.; A Solution Processed Flexible Nanocomposite Electrode with Efficient Light Extraction for Organic Light Emitting Diodes. Sci. Rep. 2014 (4): 4307.

Chapter 1 . Introduction

1.1 Solution-Processed Emitters

Incandescent, fluorescent, and light-emitting diodes (LED) have been the dominant and well-established technologies for lighting applications. Over the past two decades, the semiconductor light emitting diode (LED), also commonly referred to as an inorganic LED in the research field, has been touted as the obvious light solution in solid-state lighting due to its superior lifetime and the benefit of having no hazardous mercury over conventional incandescent and fluorescent devices. Unfortunately, inorganic LEDs utilize single crystal silicon and gallium arsenide, which are both difficult to fabricate into large-area devices. For lighting applications, inorganic LEDs require luminaries to diffuse the point source into large area lighting, which greatly reduces the lighting efficiency. With the emergence of conducting polymers, a special class of LEDs, the organic light emitting diode (OLED), has risen in the last decade to remedy the drawbacks of the traditional inorganic LED. An OLED consists of organic emitters with semiconductor properties. OLEDs can be categorized as a small-molecule light emitting diode (SMOLED) or as a polymer light emitting diode (PLED). SMOLEDs consist of small-molecule emitters, whereas PLEDs have polymer emitters. Although both OLEDs can be made into large area displays, SMOLEDs require thermal evaporation. Thermal evaporation is an expensive, high-temperature, high-vacuum process that makes SMOLEDs uneconomical for large-area display applications. In contrast, PLEDs are fabricated with solution process, which makes it a great candidate for larger area devices. Furthermore, within the past three years, a new class of material called organometal halide perovskite has also shown promising results in light emission applications. Due to the organic cation portion in its structure, organometal halide perovskite emitters allow solution process. Thus,

both polymer emitters and perovskite emitters have become appealing candidates for low-cost and large-area optoelectronic applications.

1.1.1 Conjugated Polymer for Light Emission

Organic emissive materials can be categorized into two main groups: small molecule emitters and polymer emitters. The current commercial OLEDs utilize small molecule emissive materials, but they require thermal evaporation for manufacturing process. Thermal evaporation has low utilization rate and poor scalability, which leads to high capitol cost. In order to achieve low-cost light application, the fabrication process has shifted from thermal evaporation to solution process. Because of this, the semiconducting polymer garnered a great deal of interest; they have the ability to dissolve in common organic solvents and to be cast into a film by spin-coating, screen printing, or roll-to-roll printing methods. This allows semiconducting polymers to be used in lightweight, flexible, and large area displays, which permits up-scaling production. Recently, the research on building soluble small molecule emitters has risen, but it is still under the development stage. Therefore, this work will only be focused on conjugated polymer emitters from this point on[1].

1.1.1.1 History of the Conjugated Polymer

It is generally recognized that the first conductive polymer was discovered in 1977 by Alan J. Heeger, Alan MacDiarmid, and Hideki Shirakawa[2]. They uncovered that a polyacetylene film could be doped with iodine vapors and turned into a conductor with a 7 order magnitude increase in its conductivity. This discovery and development of conductive polymers earned them the Nobel Prize for Chemistry in 2000. Although polyacetylene failed to find practical application, it opened new doors to synthesize conjugated polymers. Since then, other conductive polymers have been studied; several of these polymers include polypyrrole, polyaniline, polythiophene, and

polyphenylenevinylene. The progression of conjugated polymers has been remarkable; it has the ability to combine the mechanical properties of polymers with the electronic and optical properties of metals and semiconductors. In the 1980s, a new class of display technology, OLED, emerged and it incorporated conjugated polymers. These materials are also used for other optical applications such as photodetectors, solar cells, field-effect transistors (FET), and lasers.

1.1.1.2 Structure Characteristic of a Conjugated Polymer

A polymer must meet the following characteristics to be able to use it as a light emitting material: electrical conductivity and high photoluminescence (PL) efficiency[3]. The design of the polymer emitter is crucial to light emitting device performance. Key properties such as processability, color emission, luminance efficiency, purity, balance of charge carrier mobility, and thermal stability are important to achieve high performance PLED devices in lighting applications[4]. Unlike conduction in metals, organic semiconductors do not have free electrons. Instead, they utilize shared electrons in a conjugated system. Generally speaking, conjugated polymers include at least one chain of alternating single and double bonds. When a double bond is formed between two carbons, each carbon is sp^2 hybridized and forms three σ bonds and leaves one unpaired p_z orbital, which is perpendicular to the sp^2 hybridization plane and forms a π-bond[5]. The π electrons are delocalized along the polymer chain and form a set of bonding molecular orbitals. The delocalized electrons in the highest energy occupied molecular orbital (HOMO) are easily to be excited to the lowest energy unoccupied molecular orbital (LUMO); this process is called the π-π^* transition. The energy gap of a conjugated polymer is defined between the π (bonding) and π^* (antibonding) states; this is the minimum energy for the π electrons to undergo the π-π^* transition[3].

A conjugated polymer system can include functional backbone units, electron affinity units, hole affinity units, or emissive units. Backbone units are usually selected from wide bandgap structures. To control the emission color of a conjugated polymer, an emissive unit can be introduced to the polymer chain. As the status quo, semiconductor polymers can cover the full range of the visible spectrum from 1.5 eV to 3 eV with different molecular structures of single-polymers and copolymers. In general, by adding electron withdrawing side groups, the conductive polymer's HOMO and LUMO can be lowered. Additionally, the band gap can be increased by attaching bulky side groups to the main chains. The common conjugated polymer emitters are poly(*p*-phenylenevinylene)s (PPVs), polyphenylenes (PPPs), polyfluorenes (PFs) and polythiophenes (PTs). PPVs and PFs have high PL yields and tunable emissions, which make them good candidates among conjugated polymer emitters in OLED applications[1].

I. Poly(*p*-phenylenevinylene)s (PPVs)

Soluble green emitter, MEH-PPV, was first synthesized in 1991 and since then, PPV derivatives including alkyl-, alkoxy-, cyano-, silyl-, and phenyl-substituted PPVs have been reported. Figure 1.1 exhibits the common PPV derivatives.

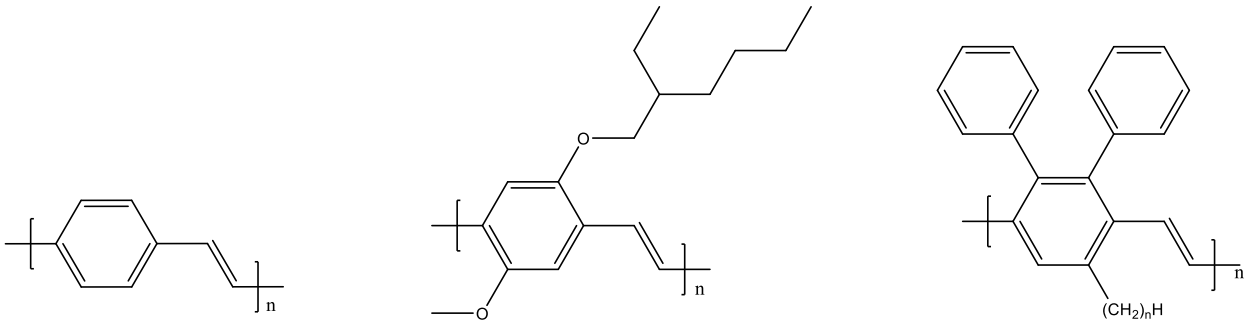

PPV MEH-PPV Phenyl-substituted PPV

Figure 1.1: Molecular structure of PPV and representative of PPV derivatives.

II. Polyphenylenes (PPPs)

Polyphenylenes (PPPs) attract great attention due to its ability to emit blue light. A drawback, however, is that unsubstituted PPPs are insoluble in solvents. In order to synthesize soluble PPPs, alkyl-, aryl-, or alkoxyl- solubilizing groups were incorporated into PPPs' side chains. Figure 1.2 demonstrates the common PPP derivatives.

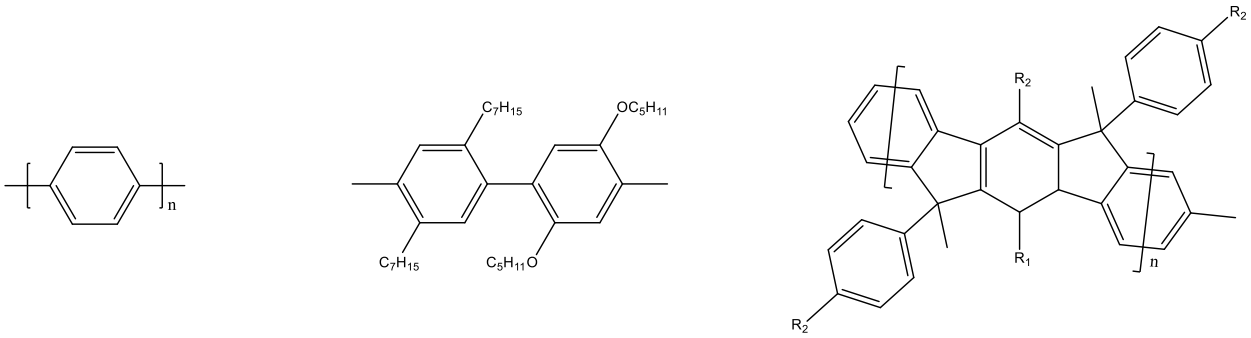

PPP PPPs Derivatives Ladder-type polyparaphenylene (LPPP)

Figure 1.2: Molecular structures of PPP and representative of PPP derivatives.

III. Polyfluorenes (PFs)

PF derivatives and copolymers are conjugated polymers that exhibit blue, green, and red emissions. A high PL yield has been reported with PFs, and PF derivative emitters are soluble in conventional organic solvents. Figure 1.3 shows the representative PF derivatives.

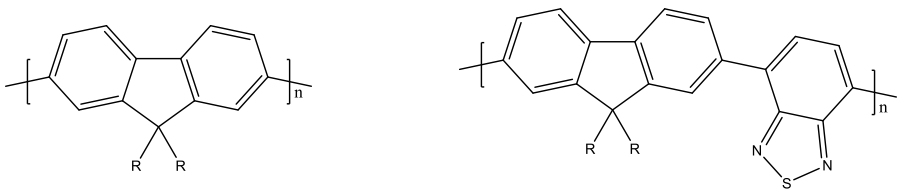

PF FB8T

Figure 1.3: Molecular structures of PF and PF copolymers.

IV. Polythiophenes (PTs)

Unsubstituted polythiophenes (PTs) have low PL yield; therefore, PT derivatives that are incorporated with cyclohexyl-, or alkyl- substitutes are used in PLEDs. The emission wavelength is blue-shifted, and the representative PT derivatives can be found in Figure 1.4.

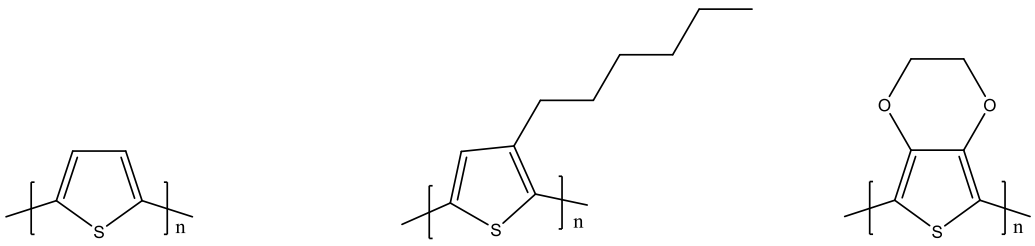

PT P3HT PEDOT

Figure 1.4: Molecular structures of PT and representative of PT derivatives.

1.1.1.3 Electrical Characteristic of Conjugated Polymers

The traditional polymers with sp^3 hybridization have valence electrons covalently bonded to carbon atoms and form σ bonds. Theses σ-bonding electrons do not contribute to the electrical conductivities of the polymer materials due to their low mobility. Conjugated polymers have sp^2 hybridized carbons, which leave unpaired Pz orbitals to combine with one another to create a conjugated orbital and form a one-dimensional electronic band as shown in Figure 1.5.

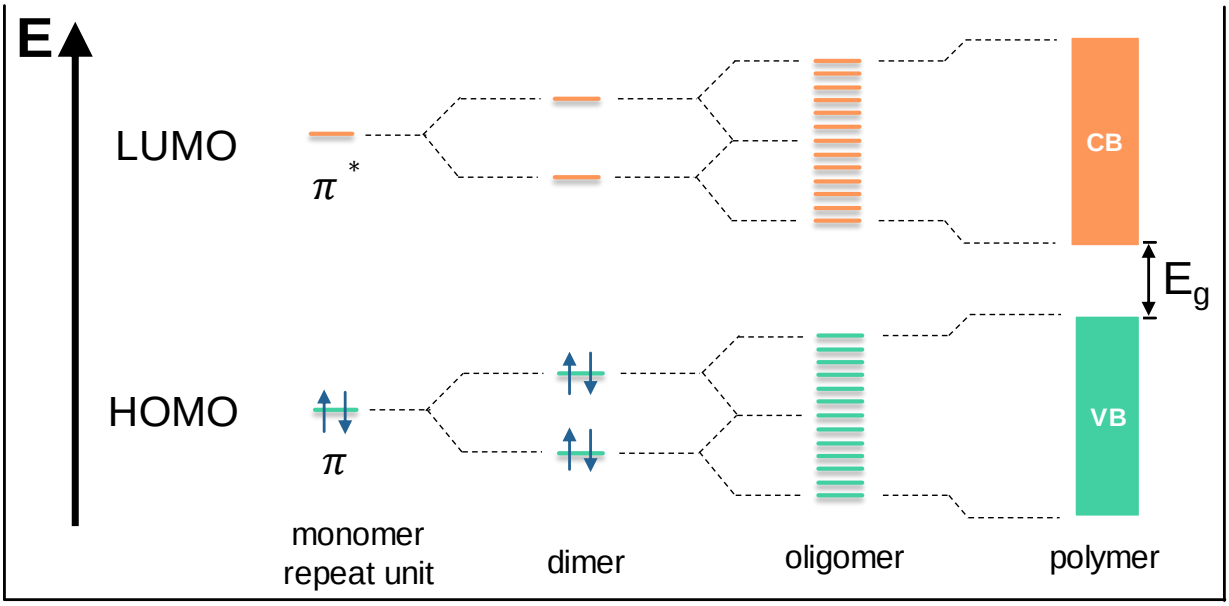

Figure 1.5: The formation of energy bands in conjugated polymers.

When a conjugated material is doped, the delocalized electrons in conjugated orbitals have high mobility. Pristine conjugated polymers are usually semiconductors or insulators with bandgap >2 eV. By only adding less than 1 wt % of dopant into conjugated polymers, the electrical conductivity of the conjugated polymers can increase several orders. There are two doping processes: oxidation

(p-doping) and reduction (n-doping). In a p-doping process, electrons are removed from polymer chains, whereas in a n-doping process, electrons are added. Band transport and hopping transport are the two mechanisms in a conjugated polymer's charge transport, and in both, charges are transported within and between polymer chains. Band transport's conductivity depends on the number of phonons existing in the polymer chains, whereas hopping transport requires external energy to move charges from one state to another excited state[3].

1.1.1.4 Applications of Conjugated Polymers

Conjugated polymers combine the benefits of mechanical properties and processing advantages from polymers along with electrical and optical properties from metals and semiconductors. These advantages allow conjugated polymers to be used in optical and electronic applications such as photodetectors, solar cells, field-effect transistors, lasers, sensors, PLED, light-emitting electrochemical cells (LEC), and organic light emitting transistors (OLET). Among all these applications, conjugated polymers are most widely researched in PLED fields.

1.1.2 Organic-Inorganic Halide Perovskite Materials for Light Emission

Next generation light emitting devices require not only high efficiency, high color quality, and the ability of color tunability, but also economical manufacturing costs achieved by applying low-temperature solution processing. Although the inorganic LED has progressed significantly in energy savings, it still requires high temperature and expensive vacuum processing for epitaxial growth of semiconductor materials. PLEDs have been the frontier to replace inorganic LEDs; but recently, organometallic halide perovskites have attracted great attention in light emitting materials due to their outstanding intrinsic optoelectronic properties and their ability in low temperature solution process.

In addition, as display technologies advance, the demand to see vivid and lifelike images continues to increase. Therefore, research has been focused on developing emitting materials that emit light with narrow full width at half maximum (FWHM). An inorganic-organic halide perovskite emitter is an excellent candidate due to its high color purity; it provides a lower FWHM compared with other inorganic and organic emitters.

1.1.2.1 Crystal Structure and Material Properties

The name perovskite initially referred to calcium titanate crystal structure ($CaTiO_3$). The class of hybrid organic-inorganic halide perovskite takes a similar crystal structure and has a chemical formula AMX_3, where A is a monovalent organic cation (i.e., $CH_3NH_3^+$, $HC(NH_2)_2^+$), M is a divalent metal cation (i.e., Pb^{2+}, Sn^{2+}, Ge^{2+}), and X is typically a halide anion (i.e., Cl^-, Br^-, I^-). The organic part A serves as the scaffold and contributes to the solution processability of the material. In a typical structure, the three-dimensional perovskite network has part M occupying the center of an octahedral cluster, while A is a 12-fold cuboctahedral coordinated with X anions, as shown in Figure 1.6. The M site in hybrid perovskites can be occupied by group IVA metals in their divalent oxidation state, however, lead has proven to have better performance and stability over group IVA metals. The stability of the divalent metal decreases as it moves up in group IVA in the periodic table.[6] The halide anion occupies the X site in the hybrid perovskite. The atomic size of the halide element increases when proceeding down group VIIA (Cl→I). As the elemental size increases, the absorption spectra shifts to a longer wavelength (red shift). The Goldschmidt tolerance factor (t) and the octahedral factor (μ) can be used to estimate whether a perovskite structure can be formed.[7] Here, t is determined by the ionic radii (r) of the molecules in A, M, and X sites with the following relationship: $t = (r_A + r_X) / \sqrt{2}\,(r_M + r_X)$; μ is the octahedral factor and is defined as r_M / r_X. According to the tolerance factor ($0.85 < t < 1.11$) and octahedral factor

($\mu > 0.442$), only the incorporation of small ions will result in halide perovskite crystal. Thus, only small organic molecules with less than 2 or 3 C-C or C-N bonds can be used in site A[8][9].

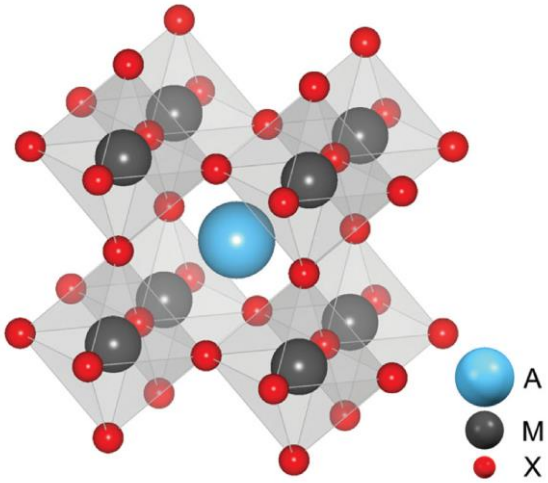

Figure 1.6: Crystal structure of cubic metal halide perovskites with the generic chemical formula ABX3. Monovalent organic cation occupies position A (blue), metal cations occupy position M (gray), and halide anions occupy position X (purple). (Photos citation:[10])

Due to the unique structure of perovskite, it possesses characteristics such as high absorption coefficient, wide absorption range, tunable bandgaps, high ambipolar charge mobility, and extended charge carrier lifetime. For LED applications, perovskite provides high color purity, which gives full width at half maximum at around 20nm regardless of the crystal size; this is due to the intrinsic crystal structure, which is similar to multiple quantum well. These make organic-inorganic halide perovskite an attractive material for light emitting diode application.

1.1.2.2 Color Tunability of Hybrid Perovskite

Hybrid perovskite has high structural flexibility, which enables bandgap tuning during synthesis. Color tuning of perovskite material can be easily manipulated through (1) changing of halide anion sources and (2) substituting monovalent cations.

Anion-Based Color Tuning. $CH_3NH_3Cl_3$, $CH_3NH_3Br_3$, and $CH_3NH_3I_3$ with bandgap at 3.11 eV, 2.3 eV, and 1.55 eV, respectively, has been successfully demonstrated; they prove color tuning can be accomplished through halide substitution. By carefully adjusting the ratio and stoichiometry of parent halide sources, perovskite material with PL emission across the visible spectrum can be obtained.[11]

Cation-Based Color Tuning. Distinct from anion color tuning, cation substitution tunes much smaller wavelengths. For example, by substituting Cs^+ to $CH_3NH_3^+$ and modifying $CsPbBr^3$ to $CH_3NH_3PbBr_3$, the PL emission shifts from 510.2 nm to 525.4 nm[12]. This is contributed to the larger cation ($CH_3NH_3^+$) substitution, which results in a slite lattice expansion[13].

1.1.2.3 Film Formation and Film Morphology

Organic-inorganic halide perovskite has versatile processability. Research groups have utilized different techniques to form perovskite film; these include one-step solution processing, two-step sequential deposition, vapor deposition, and vapor assisted solution processing.

One-step solution processing is achieved by spin-coating a precursor solution of a mixture of PbX_2 and CH_3NH_3X in a polar solvent. It is the simplest technique and has the potential to upscale in a manufacturing setting.[14] In contrast, a two-step sequential deposition method proves to have

better control of perovskite morphology. It is achieved by first spin-coating PbX_2 precursor, and then spin coating or dipping CH_3NH_3X solution to form a perovskite film.[15] The grain size is controlled by the concentration of CH_3NH_3X, and generally, a lower concentration leads to a bigger grain size. Besides the spin-coating method, spray coating and baked coating have also been used to achieve high surface coverage under ambient conditions.[16] Other than the solution process method, Vapor deposition, and Chemical vapor deposition (CVD) methods have also been performed to deposit dense and uniform perovskite film.[17]

In a one-step solution processed method, a perovskite film with poor surface coverage was formed due to the fast crystallization of $CH_3NH_3PbX_3$. Researchers have discovered that chloride has a striking influence on the morphology of perovskite thin film.[18] By incorporating a volatile chloride additive, NH_4Cl, in the reaction system shown in equation (1.1)[18], it was found that NH_4Cl effectively slowed down the crystallization and provided more relaxation time, which resulted in a uniform perovskite thin film.

$$PbX_2 + CH_3NH_3X + x \cdot NH_4Cl \leftrightarrow CH_3NH_3PbX_3 \cdots x \cdot NH_4Cl \qquad (1.1)$$

It has been found that alkyl halide additives can influence the film morphology of perovskite. The C-X bond of alkyl halide can easily dissociate during the process of thermal annealing, which produces free X^- ions to affect the coordination with Pb^{2+} in the film formation process.[16] This helps to improve crystallinity and produces better surface coverage of the film. In addition, organic halide salts were found to have a similar function in forming a uniform perovskite film.[18]

It was also discovered that the use of butylphosphonic acid 4-ammonium chloride (4-ABPACl) could result in a smooth perovskite film. The 4-AMPACl molecules serve as the crosslink agent between neighboring perovskite grains by inserting the $–NH_3^+$ group into the empty A site of the perovskite and anchoring perovskite through the other end group of $–PO(OH)_2$.[19]

Thermal annealing is also an important factor to crystallize perovskite into thin film. Studies have found that after spin-coating the mix precursor, a metastable crystalline precursor was formed and then transformed into a 3D perovskite structure at a thermal annealing temperature of 80°C.[20] One group studied the effect of annealing temperature on perovskite film formation, and it was found that 80°C was enough to fully form a $CH_3NH_3PbX_3$ perovskite. If the temperature was too low, solvents wouldn't be removed completely and resulted in an incomplete conversion of $CH_3NH_3PbX_3$ crystals. These results indicate that the reaction between PbX_2 and CH_3NH_3X was an endothermic reaction. On the other hand, if the annealing temperature was too high, it would result in the formation of PbX_2, which would worsen the device performance.[20]

The solvent engineering technique has also confirmed to improve perovskite film morphology. This strategy utilizes a proper solvent of perovskite and an anti-solvent of perovskite. For instance, perovskite precursor in N,N-dimethylformamide (DMF) can first be spin coated onto the substrate, then immediately exposed to a second solvent. The second solvent usually is a poor solvent (i.e., chlorobenzene, xylene, toluene, 2-propanol (IPA), or chloroform) for perovskite, which would reduce the solubility of perovskite and result in fast nucleation and the growth of perovskite.[21]

Polymer additive is a novel and simple method to improve film morphology of perovskite. It can be achieved with a one-step spin-coating method. Recently, poly(ethylene oxide) (PEO) additives have been found to form a smooth and uniform perovskite film.[22][23][24] PEO additives have the following functions: First, due to the hydrophilicity of PEO, it facilitates perovskite precursor solution to spread out smoothly, which helps to increase the nucleation density of perovskite. Second, PEO hinders diffusivity of perovskite precursor at the solvent drying stage during the spin coating process, which leads to small grain size and a smoother surface. Third, PEO helps to slow down the growth and aggregation of perovskite crystals, which helps to form a smooth and uniform

film as well.[16] Both solar cells and LEDs have been demonstrated with this method. Polyimide additive has also been studied to form a pin-hole free and uniform film; it is used to fill the surrounding voids to block nonradiative current losses.[25]

1.1.2.4 Perovskite Nucleation and Growth

Nucleation and growth of perovskite crystal have been studied by Anaya et. El.; in their study, in situ analysis of perovskite's photophysical and structural properties are reported.[26] The perovskite precursor contained PbX_2 planes intercalated with PbX_2 and CH_3NH_3X molecules, which separated the crystallographic planes of the inorganic material. During the spin-coating procedure, the nucleation process took place and perovskite crystallites formed. As DMF molecules evaporated, PbX_2 planes were brought closer together. Afterwards, more crystallites formed at the expense of the precursor and once the solvent fully evaporated, the grain boundaries appeared. Grain boundaries introduce trap sites and cause nonradiative decay. The following stage was the actual crystal growth, where different small crystals coalesced and grew into large domains. Finally, the last stage was reached where the perovskite crystal became stable.[26]

Humidity also plays an important role in crystallization and film morphology of a perovskite film. It has been found in studies that a fast nucleation followed by slow crystal growth yields a high-quality perovskite film. To achieve fast nucleation, high supersaturation is required; moisture would decrease the degree of supersaturation, therefore, it is most ideal to perform the spin-coating stage in a 0% humidity environment. On the other hand, at the annealing stage, with the presence of water, low supersaturation would result in slow crystal growth and form a smooth and uniform perovskite film.[27]

During the one step spin-coating process, as the solvent evaporates, supersaturation is reached and atoms start to precipitate out. Due to the concentration gradient and thermal motion, atoms will diffuse onto the substrate to lower the Gibbs free energy of the system. Next, the atoms will aggregate together and form nucleation sites. According to thin film growth theory, increasing the degree of supersaturation will result in small critical nucleus radius and high nucleation density.[27] In order to achieve high supersaturation, fast solvent evaporation is required. It is known that CH_3NH_3X phase is hydroscopic, and if the spin-coating stage is completed under a humid environment, the film would absorb water, which would increase the amount of residual solvent and delay the solvent evaporation time, thereby decreasing the degree of supersaturation.[27]

1.2 Polymer Light Emitting Diodes

The first efficient and low-voltage OLED was achieved by Tang and VanSlykte at Kodak in 1987. The initial device utilized vacuum evaporation to deposit two-layer thin films, and the p-n heterostructure SMOLED was presented[28]. The double layered structure yielded green electroluminescent devices with a driving voltage lower than 10 V and brightness over 1000 cd/m^2. Three years later, another breakthrough was achieved when the University of Cambridge discovered electroluminescence from a thin layer of conjugated polymer (PPV)[29]. Electroluminescence (EL) is the process of a material emitting light when it is electrically driven[3]. Since then, PLED has attracted immense attention in both academic and industrial fields, and other soluble forms of conjugated polymers have been developed. The key advantages of PLED include a self-emitting property, high luminance efficiency, a wide viewing angle, high contrast, low power consumption, light weight, ability for full color display, and solution processability for low cost displays.

1.2.1 Conjugated Polymer for Light Emission

The basic structure of PLED consists of a thin layer of polymer film sandwiched between two electrodes, as shown in Figure 1.7. The bottom electrode, known as the anode, is usually transparent and the top electrode, known as the cathode, is usually made with metal. The self-emitting conjugated polymers are almost like insulators- absent of donors or acceptors. Therefore, the carriers in the operational PLED must be injected from the electrodes. When voltage is applied between the two electrodes, holes are injected from the anode to the HOMO of the polymer and electrons are injected from the cathode to the HUMO of the material. Then, both charges hop between localized states of the polymer material and recombine radiatively to give off light[30]. The color emission is determined by the bandgap of the conjugated polymer; in this case, it is the energy difference between the HOMO and the LUMO. Other than the intrinsic properties of the material, the process of electron-hole recombination is crucial to the device performance.

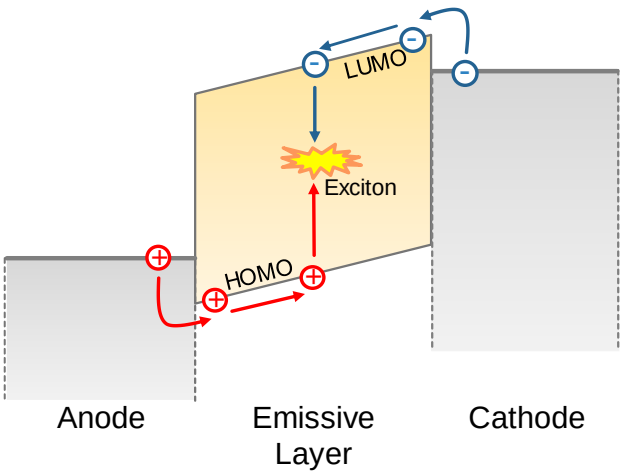

Figure 1.7: Schematic illustration of the energy diagram of the simplest OLED. Electrons are injecting into the emissive layer from cathode and holes are injecting from the anode.

1.2.2 Electrical Properties of PLED

In an ideal PLED device, there would be no restriction for injecting electrons and holes from the electrodes to the polymer emitter. Once the electrons and holes are in the polymer layer, hole and electron mobility are the same; the balance of both carriers results in high EL performance. Unfortunately, reality is far from the ideal world; not only do charge injection barriers exist for both carriers, but the imbalanced mobility of electrons and holes in the conjugated polymer is also present. In general, hole mobility is several times higher than electron mobility inside the conjugated polymer emitter.[31]

The total current in a PLED can be defined by equation (1.2):

$$J \propto P_{inj} \times M_{bulk} \qquad (1.2)$$

Where P_{inj} is dominated by the device injection current and M_{bulk} is related to the transport current in the polymer bulk. If the charge injection barriers are large, then the total device current is limited by the charge injection current, regardless of how well the transport property is in the bulk material. On the other hand, if the metal-polymer contact is ohmic, the total device current would be limited by the transport current of the bulk polymer.

In the case of large injection barriers, when the PLED is under forward bias, charges can tunnel through the barriers due to band bending under the applied field. Another possible injection path is via thermionic emission, where the charge carriers from the electrodes are given enough thermal energy to overcome the barriers at the metal-polymer contact and inject into the LUMO and HOMO of the polymer emitter. The resulting current could be a result of the contribution of the

two. Alternatively, in the situation when an ohmic contact is present at the interface, the total current is limited by the space-charge-limited currents.[31]

1.2.3 PLED Device Performance

To achieve high device performance, it is important to minimize the charge barriers between the electrode and the polymer material. When the electrodes are well matched to the bands of the polymer material, the injection barrier is minimized and the injection ability of both electrons and holes are enhanced. Once the electrons and holes are injected into the polymer layer, they must meet each other to recombine radiatively to emit light. The low mobility of charge carriers in undoped conjugated polymers plays an advantage in charge carrier recombination; the slow drift of charge carriers inside the polymer film increases the chance for electrons and holes to encounter and recombine. If one type of carrier is injected more efficiently than the other, the majority carriers might cross through the polymer layer without recombining with the minority carriers. This problem can be avoided by carefully selecting the correct electrode; one where the fermi level of the anode is close to the π-band, and the fermi level of the cathode is close to the π^*-band.

Although a monolayer PLED can be functional in principle, it provides poor device performance due to large injection barriers and unbalanced charge carriers. Since the first discovery of the PLED, its device structure has been evolving, and it was found that the multilayer PLED could suppress the injection barrier and help balance the charge carriers. A schematic illustration of a typical multilayer PLED is shown in Figure 1.8. Holes are injected from the anode into the hole transporting layer (HTL) and electrons are injected from the cathode into the electron transporting layer (ETL). ETL and HTL are selected based on their HOMO and LUMO, which reduce the injection barriers at each interface and result in higher charge injection.

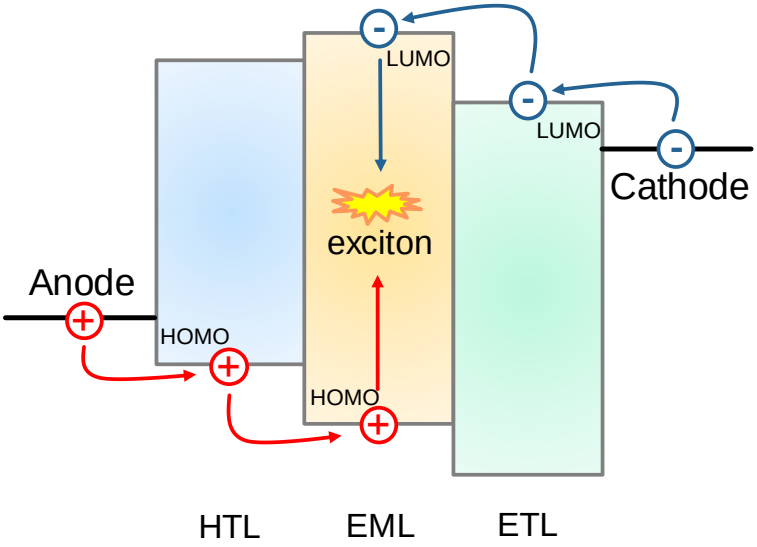

Figure 1.8: Schematic illustration of an energy diagram of a multilayer PLED.

1.3 Perovskite Light Emitting Diodes

In 2012, the first three-dimensional $CH_3NH_3PbBr_3$ nanoparticles were reported, and in 2014, the first perovskite light emitting diode (PeLED) was demonstrated. In less than three years, perovskite LEDs progressed from 1% to 8% in external quantum efficiency (EQE).[32] Although PeLEDs have not yet met the industrial standards for lighting applications, its rapid growth and advancement show the potential it has for future lighting devices. Figure 1.9 shows the comparison in device performance between OLEDs, quantum dot light emitting diodes (QDLEDs), and PeLEDs. It clearly indicates that the current efficiency and luminance of PeLEDs are fast approaching OLEDs and QDLEDs.[10]

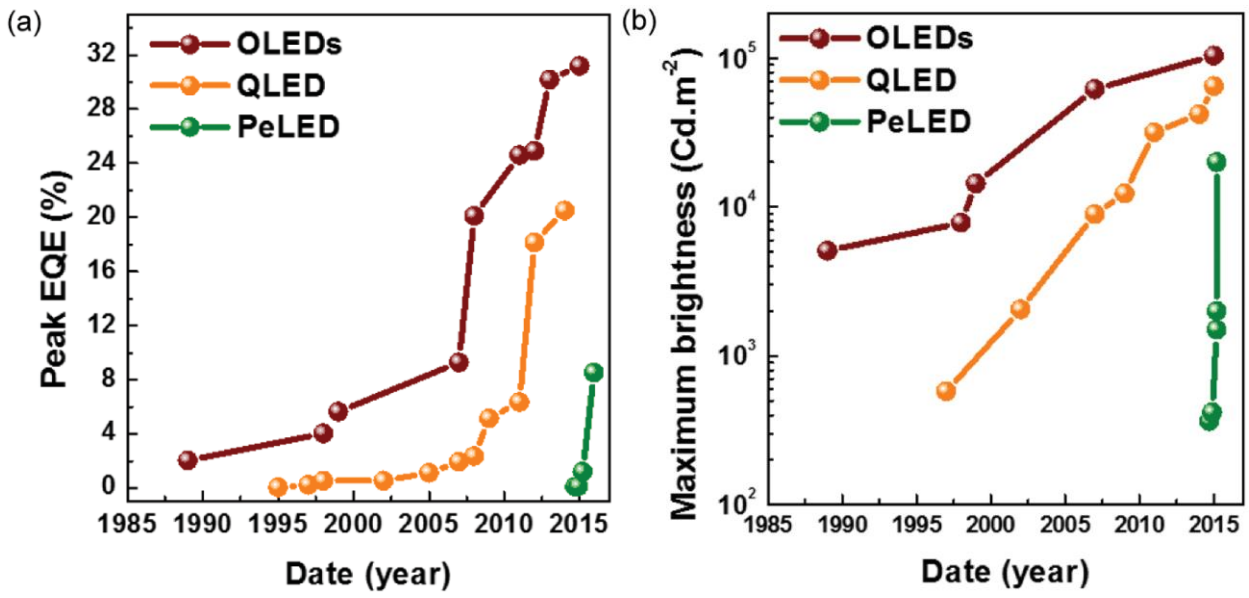

Figure 1.9: Comparison between OLEDs, QLEDs, and PeLEDs in (a) representative EQE and b) representative brightness. Source: Adapted with permission from Ref. [10]

1.3.1 Perovskite Light Emitting Diode Architectures

PeLEDs rely on charge injection, carrier transport, and radiative recombination. The PeLED device needs to be carefully designed to achieve a balance of charge injection and maximize the radiative recombination rate. In general, PeLED consists of a transparent anode electrode, a hole-transporting layer (HTL), a perovskite emitter, an electron-transporting layer (ETL) and a reflective metal as the cathode electrode. Another architecture of PeLED can fabricated as cathode/ETL/emitter/HTL/anode; the difference is that the generated photons go out from the cathode electrode instead of the anode electrode. The common materials and their energy levels for HTL, emitter, and ETL are listed in Figure 1.10. Details on how to choose the correct materials for each individual layer will be discussed in the following section.

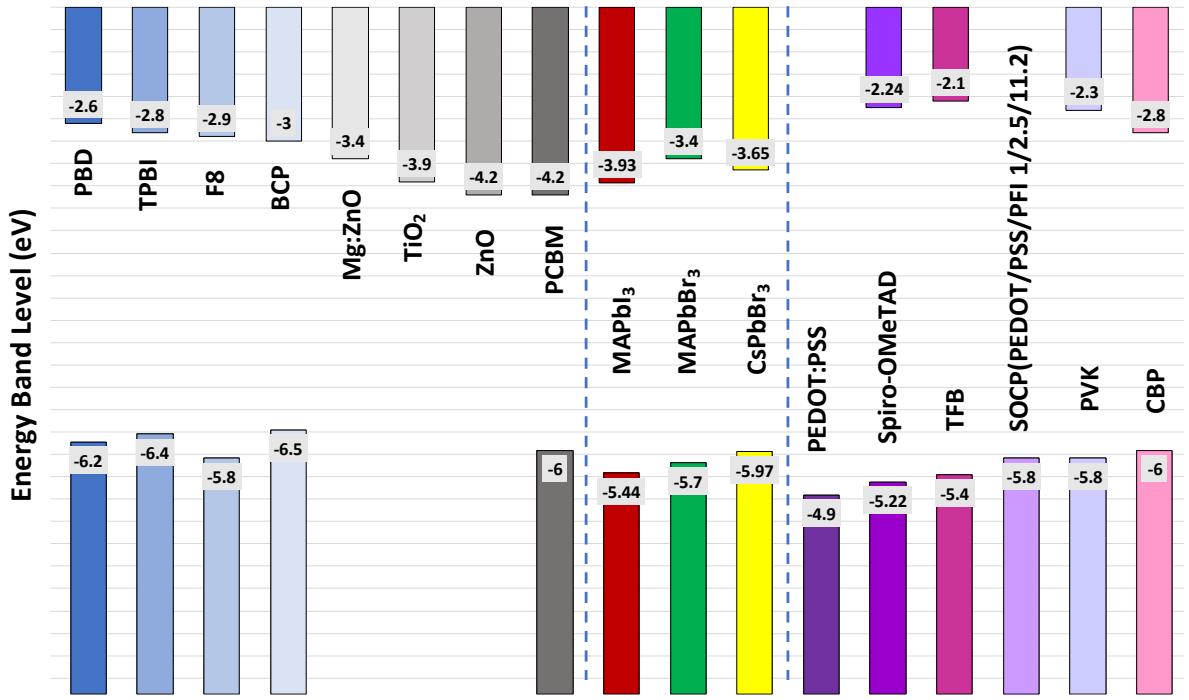

Figure 1.10: Common ETL materials (left), 3D perovskite emitters (middle), and HTL materials (right) and their corresponding bandgap.[10]

1.3.2 Enhancing PeLED Device Efficiency

Similar to a PLED operational mechanism, when holes and electrons are both injected into the perovskite emitters layer, both carriers meet, recombine radiatively, and emit light. The efficiency can be optimized by carefully designing the device structure and by properly selecting materials while considering charge injection, charge transport, and carrier recombination[10]. Once the charges are injected into the emitter layer, the transport property of the emitter plays a key role in

device efficiency. Perovskite emitters as ambipolar materials with a good ability to transport both holes and electrons make them a great candidate for light emitting material.

It was demonstrated that PeLEDs, without any HTL and ETL interlayers, had poor efficiency due to severe exciton quenching and large charge injection barriers[33]. To enhance charge injection to the perovskite emitter, appropriate ETL and HTL interlayers play an important role. Band alignments and solvent compatibility with the layers below are two factors to consider when choosing the interlayers. HTL serves as the hole transport layer with the ability to block electrons, whereas ETL serves as the electron transport layer with the ability to block holes. When the correct interlayers are applied, energy barriers between the electrode and the emitters are minimized, and charge injection into the emitter enhances, which lead to an efficient PeLED.

Having a pin-hole free, small grain, and uniform perovskite emitting layer is also pertinent in achieving a high efficiency PeLED. Methods such as adding acid to the precursor solution to lower the crystallization rate, and polymer additives to slow down crystal growth have demonstrated great success in achieving a uniform perovskite film.

1.3.3 Current Challenges and Future Direction

Hybrid perovskite emitters possess high color purity, low material cost, and simple processability; these all open perovskite to wide applications. However, there are still many challenges in developing PeLED with high efficiency and high stability. Currently, the PeLED can only reach 8% EQE, which is much lower than the efficiency of QDLEDs (~20%) and PLEDs (~30%). In order to boost the EL efficiency, research should be conducted to move toward reducing the grain size of perovskite to exciton Bohr diameter (D_B). Bohr diameter of $CH_3NH_3PbBr_3$ can be calculated according to equation (1.3):

$$r_B = \frac{\varepsilon_r m_0}{\mu} 0.053 \approx 5\ nm \qquad (1.3)$$

where r_B is the Bohr radius, ε_r is the dielectric contestant of $CH_3NH_3PbBr_3$, which is around 16, and μ is the reduced mass of $CH_3NH_3PbBr_3$ (~0.12 m_0). By reducing the grain size to D_B, the EQE can be maximized[32].

Another direction that can be taken to improve the efficiency is to employ light extraction techniques. Perovskite film has a higher refractive index ($n_{perovskite}$>2) when compared with organic films ($n_{organic}$~1.7) and substrates (n_{sub}~1.5). Due to total internal reflection, light is severely trapped inside the device, which reduces the EL efficiency; therefore, by optimizing the substrates with light extraction techniques such as microslens arrays, index matching, and nanostructures, the EL efficiency of PeLEDs can be enhanced.

Other than device performance issues, the stability of perovskite materials also requires further investigation. Perovskite degrades when there is a presence of water; this leads to the formation of lead metal. Not only is lead metal toxic, but the presence of lead would result in nonradiative recombination. As a result, there is a need to replace lead with other elements. Lead-free perovskite will allow it to be used in the bio-imaging industry. Currently, Sn and Bi have been studied as the replacement for lead, but they are still in their infant stage, and much more work needs to be done before they can be considered as viable substitutes. As for thermal stability, inorganic cation (Cs^+) has been studied as an alternative for small organic cation ($CH3NH3^+$); promising results have been demonstrated.

Despite the current challenges with PeLEDs, the high color purity and low material cost of perovskite emitters make it extremely attractive for industry. Deeper understanding of perovskite's

charge-transport mechanism, size- and shape-dependent PL, and substitute materials are required to overcome the remaining obstacles and bring PeLEDs to commercial products.

1.4 Organic Light Emitting Transistors

Since the discovery of conjugated polymers, this class of organic semiconductor materials have been widely studied in organic electronics such as OLED, OPV, and organic field-effect transistors (OLETs). Rapid advances in OLED, OPV, and OFET have made them the forefront of the lighting industry, however, a new class of organic electronics is introduced: the OLET. An organic light-emitting transistor (OLET) integrates both OFET's electrical switching capability and OLED's light emitting ability into one single device. OLETs do not require the complicated fabrication techniques of conventional active-matrix OLED displays, where FET is needed to switch individual pixels on and off. From a practical standpoint, OLETs have a bright future in low cost light emitting applications. In this chapter, the working mechanism of an OLET will be introduced, and the details in material selection and device structures will also be discussed.

1.4.1 Working Principle of OLETs

A typical OLET utilizes similar materials and device geometry as an OFET; the device is constructed with an organic semiconductor film, a dielectric layer, and three electrodes (the source, the drain, and the gate). The distance between the source and the drain is called the channel, and the gate is laid out between the source and the drain, which is separated by the insulating dielectric film, as shown in Figure 1.11. With this device structure, OLET demonstrates efficient radiative

recombination of electron and holes in the organic semiconductor (OSC) film under certain biasing conditions, which results in light emission from the channel.

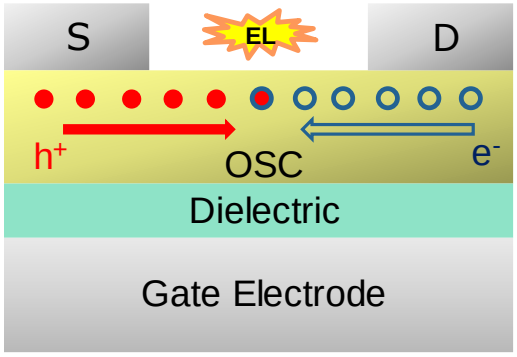

Figure 1.11: An illustration of an ideal single-component ambipolar OLET and its light generation mechanism.

The first OLET was discovered accidentally in 2003 by Heep et al; light emission was discovered from an OFET in a unipolar tetracene organic semiconductor film[34]. The p-type OFET device was fabricated with a tetracene active layer deposited onto Si/SiO_2 substrate and gold electrodes as the drain and source. As shown in Figure 1.12a, EL was observed unexpectedly in the channel next to the drain electrode, which indicated the holes and electrons recombined radiatively. The authors explained that the possibility of injection of electrons from the drain was due to imperfections of electrode fabrication. The poor electrical contact resulted in injection of electrons in the p-type accumulation mode and resulted in light emission in the tetracene film near the drain. The illustration of an OLET architecture and possible mechanism is shown in Figure 1.12b.

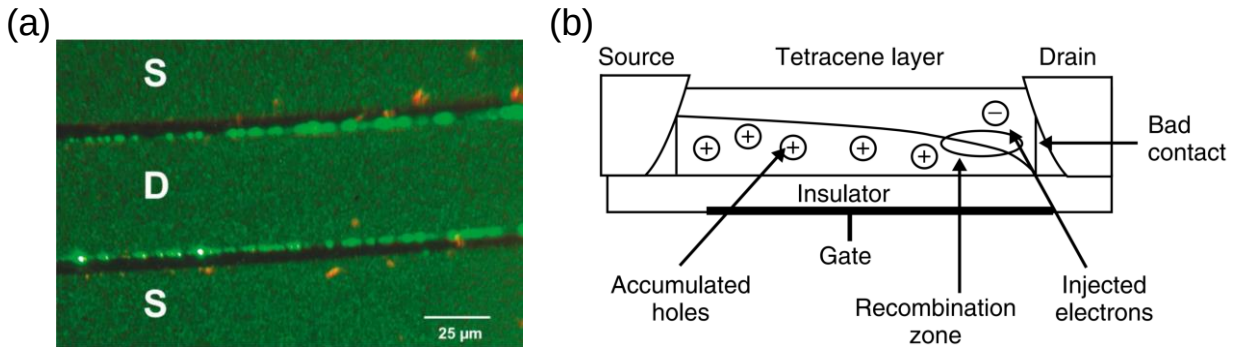

Figure 1.12: (a) Optical image of the first OLET with tetracene active layer. (b) Illustration of device architecture and possible light emitting mechanism. Source: Adapted with permission from Ref. [34]

In an ideal single-layer ambipolar OLET, the active layer has the ability to transport both electrons and holes. The electrons and holes are injected from opposite electrodes of the device according to the controlled bias. Once both types of carriers are injected into the organic active layer, an in-plane transport process is confined in the interface of the dielectric layer and the organic active layer; this is a result of the field-effects imposed by the gate voltage, V_g. Under a suitable bias condition in the three-terminal system, the electrons and holes in the channel encounter one another and recombine to emit light. Here, an ambipolar OLET built by Swensen and Yuen was used to understand the operational principle of the device[35]. The device architecture of the OLET is shown in Figure 1.13, where Au was used as the hole injection source electrode and Ca was used as the electron injection source electrode. Super-Yellow (SY), a conjugated polymer, was used here as the OSC layer, and a polypropylene-co-1-butene (PPcB)/ silicon nitride (SiN_x) bilayer was used as the gate dielectric. A thin passivation layer of polypropylene-co-1-butene (PPcB) was

applied on top of the dielectric layer to minimize the electron trapping density. Lastly, the high doped silicon wafer was used as the gate electrode.

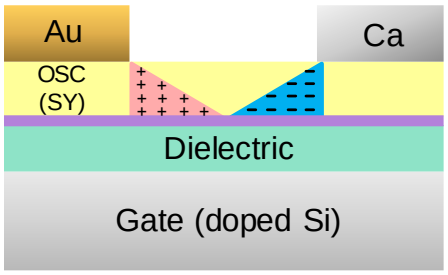

Figure 1.13: Schematic illustration of the ambipolar OLET where holes are injected from gold electrode to the super yellow OSC layer, and electrons are injected from the calcium electrode to the SY OSC layer. The thin purple layer is the polypropylene-co-1 butene passivation layer. The red triangle in the channel is the hole accumulation layer whereas the blue triangle represents the electron accumulation layer.[35]

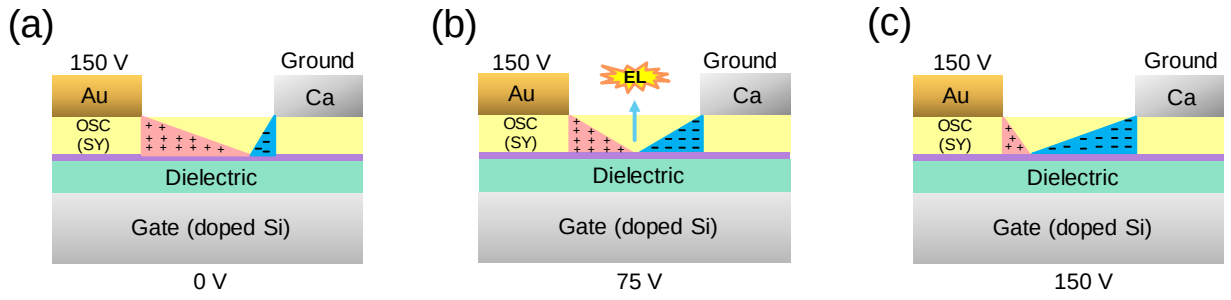

Figure 1.14: Device physics of single component-based ambipolar OLETs. (a) When $V_g < V_{ds}/2$, hole transport dominates. (b) When $V_g \sim V_{ds}/2$, ambipolar dominates. (c) When $V_g > V_{ds}/2$, electron transport dominates.[35]

As shown in Figure 1.14a, when a constant positive voltage of 150 V was applied between the Au and Ca electrode and 0 V was supplied to the gate, a layer of holes accumulated at the interface between the SY and the PPcB/dielectric layers due to the voltage drop between the gate electrode and the Au electrode. As a result, hole current dominated and flowed from the Au to the Ca electrode. As the gate voltage swept to around 75 V, as shown in Figure 1.14b, the voltage drop between the gate electrode and the Au electrode decreased, and ambipolar transport dominated. The hole accumulation layer reduced in magnitude and its extension along the active channel. At the same time, electron accumulation formed in similar magnitude and extension as the voltage drop between the gate and Ca electrode increased. In this case, the electrons and holes had the opportunity to meet in the active channel to form excitons and emit light. As the gate electrode continued to sweep to 150 V, the voltage drop between the gate and the Ca electrode continued to increase, and a layer of electrons accumulated at the interface of the SY/dielectric; as a result, the electron transport is now dominant[35] (Figure 1.14c). By carefully manipulating the biases between the three electrodes, the emission location and the area was able to be controlled[36].

1.4.2 Key Building Blocks of OLET

To obtain highly efficient OLETs, the material selection of the key elements of the device is crucial. A basic OLET device is constructed with three main components: a dielectric layer, an active layer, and the electrodes. Individual elements will be discussed in detail.

Dielectric Layer: the dielectric layer is usually sandwiched between the gate electrode and the OSC layer; the geometry creates a gate/dielectric interface and a dielectric/OSC interface. A good dielectric material needs to have the following features: high capacitance, low leakage, easily processed, compatible with electrode and OSC materials, high reliability, and stability[37]. The

voltage required to create an accumulation layer in OLET is determined by the capacitance of the dielectric layer. The charges induced on the OSC layer can be represented in Equation (1.4) below:

$$Q = CV = (k\varepsilon_0 \frac{A}{t})V \qquad (1.4)$$

where *k* is the dielectric constant of the material, A is the area, ε_0 is the permittivity of free space (8.85 x 10^{-12} F/m), and *t* is the distance between the gate electrode to the OSC layer[37]. From equation (1.4), it is obvious to see that in order to increase the capacitance, a larger *k* material or thinner dielectric material is required. Although high-*k* dielectric materials provide higher charge density, an increase in charge density does not enhance light generation. This is due to the low mobility in high-*k* dielectric materials. Researchers have proved that an increase in the mobility of low-*k* materials can compensate the decrease in charge density[38]. Out of all the dielectric materials, poly(methyl methacrylate) (PMMA) has been found to be the best due to its good dielectric features (ε = 3.6) and its solubility in solvents. In addition, PMMA is free of -OH group, which helps avoid electron trapping in the dielectric layer[36]. As an alternative, electrolyte dielectrics can be used in OLET. Due to their intrinsic properties as ionic conductors, electrolyte dielectrics enable rapid motion of positive and negative ions under electric fields and create strong accumulation layers at the interface of dielectric/OSC[39]. In addition, a new class of solid polymer electrolytes called ion gels have also been discovered to show good operational stability under ambient conditions[37].

Emissive Ambipolar Organic Semiconductors. In OLED, the emitters do not need to be concerned with high mobility since the channel length is exceedingly short, within tens of nanometers. In the case of OLETs, the channel lengths are generally a couple of micrometers wide, therefore, the OSC materials must have good mobility. A good OSC material for an OLET should have good

mobility, great EL properties, and ambipolar abilities. However, high mobility and good EL properties are two conflicting features, thus developing good OSC materials has remained a challenge. In general, π-conjugated polymers in an amorphous state tend to have good EL properties, but low carrier mobility. In contrast, in a well-ordered packing structure of a conjugated polymer, π-π stacking provides high mobility but lead to luminescence quenching in the OSC materials. Many molecular design strategies have been utilized to develop a OSC material with high mobility and good EL by tuning intermolecular packing, overlap, and interaction. One example of the many techniques to improve the light emission of an OLET is to add carbon nanotube (CNT) into conjugated polymers. It has been shown the presence of CNT significantly decreases the contact resistance between the electrode and the OSC layer, therefore more carriers are injected, which lead to higher ambipolar currents and light emission intensities[40].

Charge Injecting Electrodes. For typical OFETs, both source and drain use the same material as the electrodes. The symmetric source-drain electrodes possess the same work function. In the case of OLETs, balance of carrier injection is one of the keys to achieving a high efficiency device; however due to the wide bandgap of the OSC material, having the same work function for both source and drain electrodes make it impossible to achieve balanced carriers. The key factor controlling the charge injection process is the energy barriers that carriers need to overcome to inject into the OSC. The general rule is to minimize the energy barriers between the electron/hole-sourcing electrode and the LUMO/HOMO of the OSC material. With this in mind, applying asymmetric electrodes for source and drain could match the energy level of the OSC materials, which has proved to be an effective method to achieving charge balance in electrons and holes. It has been established that a low work function material, such as Al, can be used as an effective electron-sourcing electrode, and a high work function material, such as Au, can be an effective

hole-sourcing electrode[35]. However, it is important to keep in mind that by applying asymmetric electrodes, the fabrication process becomes more complex and costly.

1.4.3 OLET Device Structure

Although unipolar OLETs were discovered first, the luminance efficiency hits a bottleneck due to the quenching of excitons near the minority carriers-sourcing electrode. Therefore, ambipolar OLETs became the focus for future applications. Innovative device structures have been reported to achieve high efficiency single-component ambipolar OLETs. One example is the split-gate (SG) OLET introduced by Hsu et al., where one can individually control carrier injection, transport, and recombination within the channel.[41] As shown in Figure 1.15a, an equal length of accumulation layers of holes and electrons are formed when V_{G1} and V_{G2} were set to 0 V and -150 V. By further tuning both gate electrodes, the emission location and intensity changes, as illustrated in Figure 1.15.

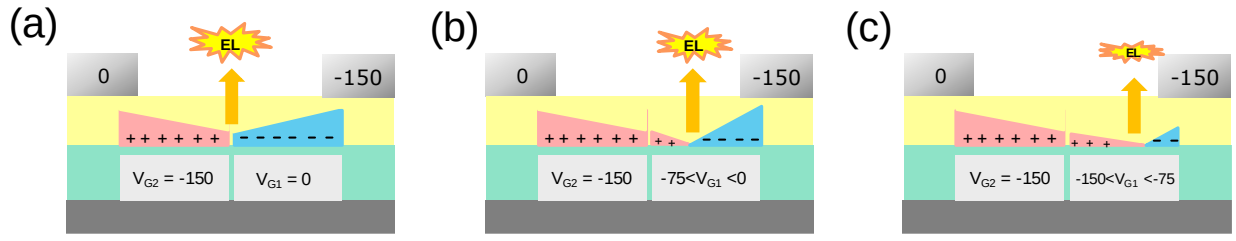

Figure 1.15: Schematic illustration of the SG-OLETs and shifting of recombination zone under various bias.[41]

Unfortunately, given the challenges in designing a single component active layer with excellent mobility and superior EL properties, a single-component ambipolar OLET's efficiency is limited. An alternative approach to improve the device efficiency is to apply heterojunction structure in ambipolar OLETs; this includes bulk, layered, and laterally arranged heterojunctions, as shown in Figure 1.16.

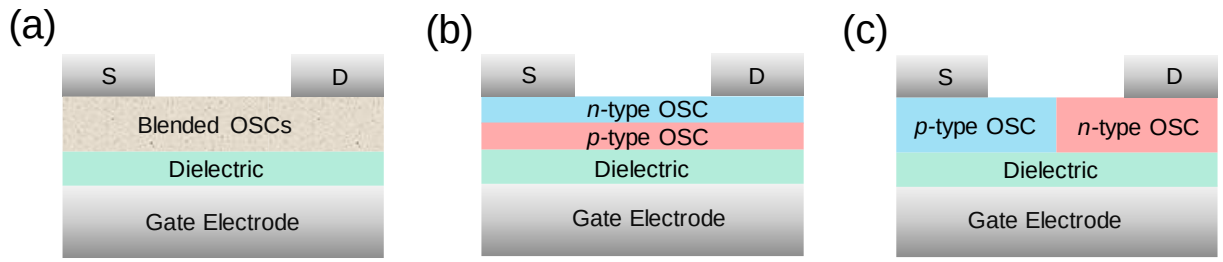

Figure 1.16: A schematic illustration of (a) bulk heterojunction, (b) layered heterojunction, (c) laterally arranged heterojunction of OLETs.

Bulk Heterojunctions: Researchers have found by blending n-type OSC with p-type OSC in an appropriate ratio, the enhanced EL intensity is due to the increase in balance of carrier mobilities. Although some advances have been seen, in this blended single layer, it is difficult for holes to flow in the electron transporting material and for electrons to flow in the hole transporting layer. Thus, the probability of electron-hole recombination is reduced.

Layered heterojunction structure: Another method is to physically separate the electron and hole and confine both carriers in the active layer. Ever since the first OLET was discovered in 2003, they suffered from low EQE due to exciton quenching and material impediments. It wasn't until 2010 when Capelli et al. designed a trilayer ambipolar OLET that successfully achieved a 5% EQE.

As shown in Figure 1.17, the trilayer ambipolar OLET consists of an active layer sandwiched between an electron transporting layer and a hole transporting layer. By keeping the recombination zone far away from the metal contact, it minimized the quenching of excitons. In the study, Capelli et al also successfully demonstrated that both emission area and location can be tuned by voltage.[42] The authors explained that this phenomenon was possible by avoiding the holes and electrons accumulation in the OSC layer so the excitons could spread across the entire channel, which resulted in light emission in the entire channel of OLETs.

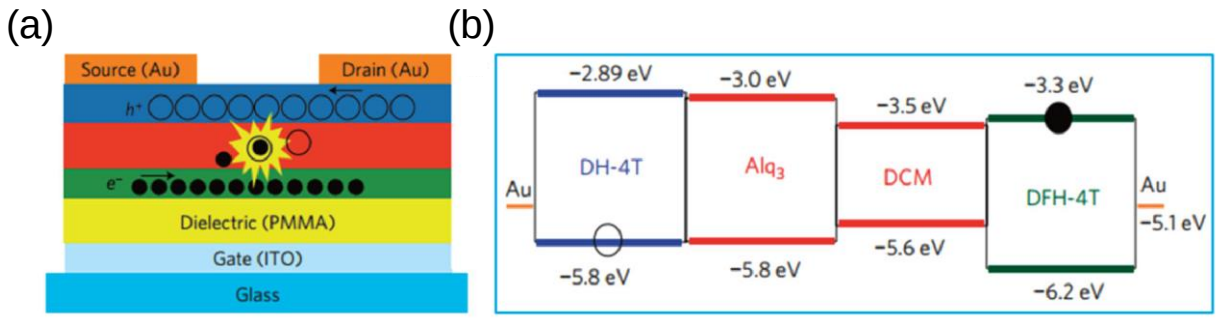

Figure 1.17: High performance trilayered heterojunction. (a) Schematic illustration of a tri-layered ambipolar OLET and the light emission mechanism. (b) Energy level of feature materials. Source: Adopted with permission from Ref.[42]

Laterally Arranged Heterojunction Structure: Another important architecture is the laterally arranged heterojunction structure of ambipolar OLETs, as shown in Figure 1.16c. The advantage of this structure is that by overlapping n-type and p-type OSCs, the recombination zone is confined inside the channel and light is generated at the interface of the n-type and p-type OSCs. The recombination zone is far from the electrodes and avoid exciton quenching.

Although heterojunction structure of OLETs show advancement in device performance, all the previously introduced device architectures require high voltage to achieve light emission due to the low mobility of OSC materials and long channel length. A new class of OLETs with a vertical structure could be operated under low voltage because it has an exceptionally short distance between source, drain and gate electrodes as shown in Figure 1.18[36]. Just like an OLED, a vertical OLET could operate at low voltage, which is attractive for lighting applications.

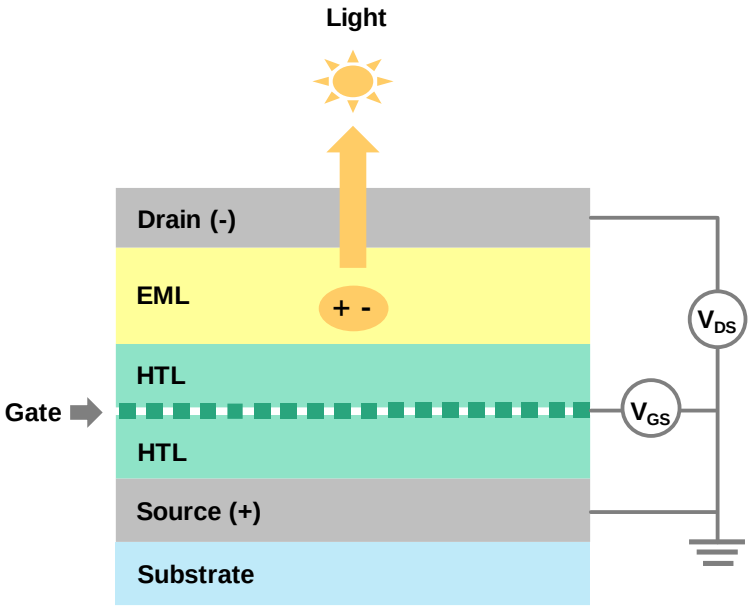

Figure 1.18: Schematic illustration of a vertical ambipolar OLET and its working mechanism.

1.5 Motivation and Research Scope

Solid state lighting is in need of cost effective electroluminescence candidates; conjugated polymers and organometal halide perovskite emitters have great potential due to their ability to be solution processed. However, solution-processed light emitting devices have poor device performance due to their overly simple structures. There are limited materials that can withstand solvent attack from the approaching layers; this constrained choice of materials makes it difficult to achieve a balance of electron and hole injection. As a result, lower efficiency is found in solution-processed light-emitting devices compared to conventional thermal-evaporated SMOLED.

The first part of my dissertation focuses on methods to solve the poor efficiency of conjugated polymer based light emitting devices. By employing a substrate incorporated with nanoparticles as the anode of the PLED, I have demonstrated a flexible PLED with high device efficiency. The nanoparticles inside the substrate cause photons to scatter and change the light path to redirect the trapped photons into the air. An alternative approach to enhance device efficiency is by applying an OLET device architecture. Under appropriate bias conditions in the three-terminal system of the OLET, the balance of electrons and holes in the conjugated polymer emitter can be improved, resulting in an increase in device efficiency compared with the conventional PLED device structure.

The second part of the dissertation investigated methods to improving a perovskite emitter's film stability and demonstrated multifunctional light emitting devices including an LETD and a stretchable PeLED. Unlike a continuous polymer film, a perovskite film is composed of individual grains. Much effort has been put in to achieving a high coverage perovskite film to avoid device

shorting. A high coverage film along with small perovskite grains was established by integrating a polymer additive. A polymer matrix not only facilitates the growth of small grains, but also achieves a pinhole free perovskite film. The robust perovskite-polymer film was assimilated into the LETD and provided instantaneous pressure mapping. In addition, by incorporating an elastomer, a stretchable perovskite film was made possible and a stretchable peLED was established.

Based on the work completed during my PhD study, this dissertation is divided into six chapters:

Chapter 1, the current chapter, provides a brief introduction and the state of the art in both conjugated polymers and organomental halide perovskite emitters. In addition, the device mechanisms of OLEDs, PeLEDs, and OLETs are introduced.

Chapter 2 presents the work on high efficiency white PLEDs based on the light extraction nanocomposite electrode. Subjects covered include the design of the transparent flexible nanocomposite electrode, the mechanism of the light extraction effect, and both the simulation and experimental results based on the white PLED device structure.

Chapter 3 describes the new device structure of OLETs that incorporate a white conjugated polymer emitter as the OSC layer. The novel vertical structure OLET demonstrates that by modifying the gate bias, the luminance of the device can be optimized. This work paves a new path in developing low-cost lighting devices by combining solution-processable conjugated polymer emitters and the two-in-one OLET device structure.

Chapter 4 introduces the first light emitting touch-responsive device (LETD), which provides instantaneous visualization of pressure mapping. This work presents the design concept and

fabrication of the LETD. In addition, it demonstrates the potential applications of the LETD. A perovskite composite emitter is chosen as the active layer based on its economic benefit. The entire device was fabricated by a solution process under ambient conditions with humidity levels at approximately 30-40%.

Chapter 5 demonstrates a functional stretchable PeLED based on a composite perovskite emitting layer and a transparent stretchable electrode. The design and characterization of the composite perovskite film is also exhibited, and the stretchable PeLED remained functional up to 60% stretchability.

Chapter 6 summarizes the dissertation and provides outlook for future research in cost-effective optoelectronics.

Chapter 2 . Flexible Polymer Light Emitting Diodes with Efficient Extraction for General Lighting Application

2.1 Introduction

PLEDs have been intensively studied due to their potential for low manufacturing cost in large-area flat panel displays and solid states lighting.[43][44] PLEDs are created with solution process technologies such as ink-jet printing, roll-to-roll printing, and screen printing. All these processes enable the scalability of the displays and they do not require shadow mask, which would significantly reduce the overall cost when going into mass production. In addition, PLEDs have potential to be used in flexible lighting applications due to their mechanical flexibility.[45–47]

2.1.1 Problem Statement of Light Losses

The introduction of phosphorescent dopants into the emitter molecules sanctions disallowed phosphorescence emission, which enables both singlet and triplet exciton energy and opens the possibility of obtaining 100% internal quantum efficiency in OLEDs.[48–51] Even though IQE can now reach 100% in principle, it is studied that the external quantum efficiency (EQE) of OLED is less than 20%.[52–54] External quantum efficiency is defined as the ratio of the total number of photons emitted from the device in all directions to the number of electrons injected. Due to the large difference in the refractive index (n) value between individual layers of the OLED devices,

a large portion of photons generated in the emissive layer are trapped in the device. This low out-coupling efficiency is the main limitation in fabricating high efficiency OLEDs.

2.1.1.1 Fundamental Principle

The external quantum efficiency is the ratio of the number of photons emitted from the device over the total number of electrons injected. It can be expressed in equation (2.1) below:

$$EQE = \gamma \cdot \chi \cdot \eta_r \cdot \eta_{out} = \eta_{int} \cdot \eta_{out} \qquad (2.1)$$

where EQE is the product of the factor of charge carrier balance, γ, the exciton spin factor, χ, the photoluminescence quantum efficiency, η_r, and the light out-coupling efficiency, η_{out}. In addition, the charge carrier balance factor, the exciton spin factor, and the photoluminescence efficiency are summarized as the internal quantum efficiency (IQE).[53]

The charge carrier balance factor, γ, represents the probability of an electron-hole recombine and form an exciton. The charge carrier balance can be maximized by balancing the charge mobility through applying a charge injection layer. The typical hole injection layer is poly(3,4-ethylenedioxythiophene): poly(styrenesulfonate) (PEDOT:PSS), and the LiF is one example used to improve electron injection ability. By balancing the mobility of both electron and holes, it is possible to obtain a charge carrier factor of 100%. When an unbalanced charge mobility is present, it is possible for both electrons and holes to travel through the entire device without meeting to form excitons, which would result in large current leakage and low IQE.[55]

The spin factor, χ, represents the spin statistics of the formed excitons. The excitons in OLED have a singlet-to-triplet ratio of 1:3, and there will only be singlets decay to the ground state when using a fluorescence emitter because the relaxation of the triplet states to their ground state is spin

forbidden. However, when phosphorescence emitters are used, both singlet and triplet state excitons are free to relax to their ground states due to strong spin-orbit coupling, evidenced by a 100% value of χ. [53]

The photoluminescence quantum efficiency, η_r, represents the probability of the radiative recombination of excitons. It can be denoted as equation (2.2) below:

$$n_r = \frac{K_r}{K_r + K_{nr}} = \frac{number\ of\ emitted\ photons}{number\ of\ total\ generated\ excitons} \qquad (2.2)$$

where K_r and K_{nr} represent the rate constants of the radiative and non-radiative decay of excitons.[53] The value of 100% η_r could be achieved in principle with high-purity organic materials. In theory, IQE could reach 100% in a perfectly designed system. However, the majority of the light is not able to be out-coupled through the transparent substrate. Due to the out-coupling loss, the EQE of a conventional OLED device cannot exceed 20%.

2.1.1.2 Light Out-Coupling Efficiency

Figure 2.1 demonstrates the different ways of trapping the photons inside the device. It can be seen that out-coupling losses are through the Surface Plasmon Polaritons (SPPs), the wave-guided mode (WG), and the substrate mode. Due to the presence of SPPs at the interface of the metal and the organic layer (dielectric layer), 20% of the generated light is dissipated as scattered light or as non-radiative emission at the metal region.[53] The surface plasmon polariton is an electromagnetic wave propagating along the interface between a dielectric and a metal, and its electromagnetic field exponentially decays into surrounding media. An OLED is composed of multiple layers and each of them have a different reflective index (n); organic layers usually have a refractive index of 1.7, indium tin oxide (ITO) have a reflective index of 1.9, glass is 1.5, and air is 1. According to

Snell's law, the total internal reflection can occur at the interfaces between glass and ITO and between glass and air. Approximately 40% of the generated light is trapped within the glass/ITO interface and it is categorized as the loss in waveguided mode; another 20% of the generated light is then trapped in the glass/air interface and that is categorized as the loss in substrate mode. Due to the conventional design of OLED, only 20% of the generated light is received by the environment. On-going research is being conducted to develop new methods in extracting light from OLED.

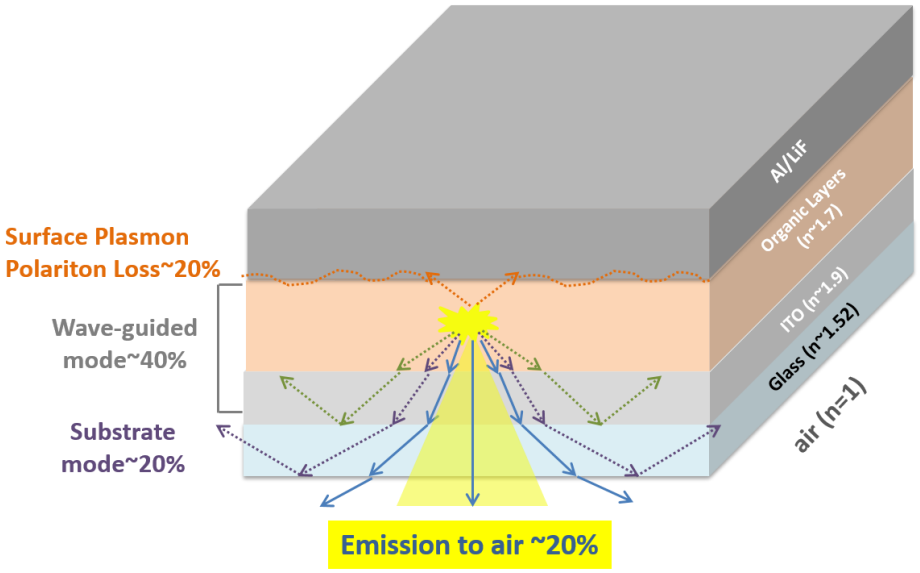

Figure 2.1: Schematic illustration of light out-coupling losses in a conventional OLED.

2.1.1.3 Current Methods

Many techniques have been proposed to resolve the problem and increase light out-coupling efficiency. Here, a few representative works are introduced which include microlens, modulation of refractive index, surface plasmon, and microcavity.

Microlens. A simple method to extract the light in the glass-mode is to apply an array of microlenses to the glass substrate[56]. Due to the corrugated structure of the microlenses, the incident angle from the substrate to air is changed. The light ray, which has an incident angle that is larger than the critical angle that would usually be reflected and trapped in a planar, can now be out-coupled by a microlens array attachment. This mechanism could out-couple the light in the glass mode and result in luminance enhancement.

Modulation of refractive index. Due to the high refractive index of ITO, a large portion of the light is waveguided in the ITO layer. To extract the light inside the waveguide mode, Forrest *et el.* proposed a method that embedded a low refractive index grid between the ITO and the organic layer. One candidate for the low index grid material is silicon oxide (SiO_2), which has a refractive index value of 1.5. This method is effective in extracting the light in the waveguided mode and is independent of wavelength. This results in a 2.3 times out-coupling enhancement compared with a conventional OLED. In addition, by combining the use of microlens array in the back of the substrate, the coupling enhancement could become up to 3.4 times higher than the conventional OLED.[57] Another way to enhance η_{out} through the extraction of light in the waveguided mode was proposed by Lee *et el*; it is to use nanofacet-structured refractive index modulation layers (RIML) between the ITO layer and the glass substrate.[58] The requirement of the RIML is to have its refractive index between the ITO (n=1.9) and the glass (n=1.5). With the insertion of RIMLs,

the light rays that were larger than the original critical angle can now enter the RIML region and be refracted into a direction toward the substrate normal. The presence of the RIMLs significantly increases the critical angle and enables more light to be emitted out to the air.

Surface Plasmon Emission. As indicated earlier, about 20 to 40% of the light is trapped in the SPP mode. Lee *et el.* introduced OLEDs with buckling structures, which can out-couple the light in SPP mode that would otherwise be lost in the metal (ex. Al) cathode layer[59]. In their work, the random orientation of the buckling structure resulted in radiative SPP coupling. The light in SPP mode was scattered by the grating wave vector and resulted in the light escape cone. Thus, the light in SPP mode is being coupled out[60].

Microcavity. To obtain high efficiency OLEDs, a highly transparent electrode is needed. However, a semitransparent electrode can lead to a microcavity effect, which will then improve the optical property of OLEDs. When designing a resonant cavity inside the device structure, OLEDs with a semitransparent electrode at a given wavelength, λ, will obtain an amplified light output that is proportional to the intensity of the light generated inside the active layer by the emitter under no cavity effect ($I_{int}(\lambda)$) and a cavity enhancement factor[61].

2.1.2 Proposed Solution

Although current existing techniques have shown great results in light extraction efficiency, many of them are not compatible with solution-based large-scale processing for flexible light emitting applications. Here, we report a solution to achieve both high out-coupling efficiency and high flexibility of an OLED device by replacing glass and ITO with a flexible polymer nanocomposite

conductor. Silver nanowire (AgNW) is chosen as the transparent electrode due to its characteristic of low sheet resistance at high transmittance and its mechanical flexibility. The nanocomposite substrate is composed of a single layer of AgNW embedded in the surface of a barium strontium titanate (BST) nanoparticles-polymer nanocomposite. With the addition of high refractive index nanoparticles, light extraction is further enhanced through the scattering of the trapped light inside the substrate. By tuning the size and the concentration of the nanoparticle loading, we could further enhance the out-coupling efficiency of PLED. The maximum external quantum efficiency (EQE) of solution-processed white PLED fabricated on the nanocomposite substrate achieved 21.7%. There is a 95% enhancement compared with the white PLED on conventional ITO/glass substrate.

2.2 Experimental Section

2.2.1 Materials

White emissive polymer was provided by Cambridge Display Technology. Aluminum evaporation slug, Cesium Fluoride (CsF), 2,2-dimethoxy-2-phenylacetophenone (photoinitiator), and chlorobenzene were purchased from Sigma-Aldrich. Low conductivity poly(3,4-ethylenedioxythiophene): poly(styrenesulfonate) (PEDOT:PSS) (CleviosTM P VP AI 4083) was purchased from H.C. Starck Inc. 1,3-bis[(4-tert-butylphenyl)-1,3,4-oxidiazolyl]phenylene (OXD-7) was purchased from Lumtec. Silver nanowires were purchased from Zhejiang Kechuang Advanced Materials Co. BST nanoparticles (HBS-2000) were purchased from TPL Inc. Ethoxylated(4) bisphenol-A dimethacrylate monomer (DMA) was provided by Sartomer.

2.2.2 Fabrication of Nanocomposite Substrate

A thin uniform film of AgNW with 20 Ω/□ sheet resistance was prepared by using a Meyer rod to spread a dispersion of AgNW (0.5 wt %) onto a releasing substrate. Then the AgNW film was annealed for 8 minutes at 165°C. Next, liquid monomer solution was mixed with 100 weight parts of DMA and 1 part of photoinitiator. BST nanoparticles were dispersed in the liquid monomer solution at 2 wt%. The resulting BST-dispersed liquid monomer was coated on top of the AgNW film. The coatings were then sent to a UV lamp and cured at 2.5 W/cm^2 intensity. After the film was cured, the AgNW-BST-polymer composite electrode with AgNW incorporated into the BST-containing polymer was peeled off from the releasing substrate. AgNW-polymer composite electrode followed the same fabrication process, except there is no BST dispersed in the liquid monomer solution.

2.2.3 Fabrication of White PLED

White PLEDs were fabricated on AgNW-BST-polymer nanocomposite electrode, AgNW-polymer nanocomposite, and ITO/glass substrates. The ITO/glass substrates (10 ohm/sq) were cleaned subsequently with acetone, detergent water, deionized water, acetone, and 2-propanol (IPA) for 60 minutes with sonication. Then they were dried with air and treated with oxygen plasma at 100 W power for 2 minutes before use. Next, PEDOT:PSS was spin-coated onto all three substrates at 4000 rpm and annealed at 120°C for 20 minutes. The resulting PEDOT:PSS film was ~40nm. The white emissive polymer blend solution was mixed with white emissive polymer and OXD-7 in a weight ratio of 100:40 in chlorobenzene. An emissive polymer blend layer was then spin coated on top of the PEDOT:PSS layers, and the emissive layer was baked under 80°C for 30 minutes. The resulting white emissive layer was ~75nm. Next, a thin layer of CsF (1nm) and a

layer of Aluminum (100nm) were deposited in a vacuum thermal evaporator. The active area of the device was 0.13cm^2.

2.2.4 Characterization of Nanocomposite Substrate and White PLED

Scanning electron microscope (SEM) images were taken by a JEOL JSM-6710F scanning electron microscope. Atomic force microscope (AFM) images were performed by Bruker dimension icon scanning probe microscope. Photoluminescence (PL) spectra were carried out by using Photon Technology International Spectrophotometer.

Luminance-voltage (L-V), current-voltage (I-V) performance were measured with the help of a Keithley 2400 Semiconductor Characterization System and a pre-calibrated silicon photodetector inside a nitrogen filled glovebox with oxygen and moisture levels both less than 0.1 ppm. The EL spectrums were collected with a photoresearch PR655.

2.3 Results and Discussion

2.3.1 Fabrication of AgNW-Polymer and AgNW-BST-Polymer Electrode

Figure 3 illustrates the fabrication process of the AgNW-based nanocomposite substrate. First, the AgNW ink was prepared by mixing the original AgNW ink with methanol and IPA solvents with a volume ratio of 1:2:4, respectively. Methanol was used to improve the film morphology of the AgNW film; other solvents such as ethanol and ethylene glycol have been tested in previous studies and it was found that methanol leads to the most uniform coating[62]. In order to achieve uniform and agglomeration free films, the AgNW solution needed to be well dispersed. To deposit

a film, 30μL AgNW ink was deposited on the glass slide, as shown in Figure 2.2a. Glass substrate was used here to provide a smooth release surface. Then, a Meyer rod rolled over the solution and left a uniform AgNW thin film. This method can be easily scaled up in an industry setting with roll-to-roll, slot-die, or graveur coating. The initial sheet resistance of the wet nanowire mesh was high; this is due to the presence of the thick PVP surfactant layer. Next, the AgNW film was prebaked at 110°C for ten minutes to get rid of the solvents. The final thickness of the dried film was controlled by a concentration of the AgNW ink, AgNW dimensions, and the size of the Meyer rod[62]. Then, the substrate was submerged into deionized (DI) water for 20 minutes to wash away the PVP surfactant inside the meshed network. The coating was then dried at 165°C for 10 minutes, which serves as the annealing step in order to improve the conductivity of the AgNW film.

The reduction in sheet resistance is attributed to the flowing and partial decomposition of PVP surfactant, which allows Ag nanowires to make contact and fuse together[63]. However, it is important to control the annealing time of AgNW. If AgNW is left on annealing temperature for too long, the sheet resistance of the electrode will increase because AgNW will coalesce into disconnected droplets. For AgNW electrode, the charge transport mainly includes two components: (1) along the nanowires and (2) along the junctions. In the previous study, silver was deposited by E-beam lithography to measure the resistance along the wire and the junction resistance. It was found that the line resistance of individual nanowire was around 300 Ω, whereas the junction resistance between the two nanowires was larger than 1 GΩ[62]. Therefore, annealing the AgNW film at high temperatures could fuse the nanowires together and further reduce the sheet resistance. In addition, the denser the AgNW wire network is, the lower the sheet resistance will be. Tuning the size of AgNW could also result in reduction in sheet resistance; the longer and thinner

nanowires will result in denser packing and improve its conductivity. After annealing the AgNW film, the resulting sheet resistance was around 50Ω/□ at 93% transmittance.

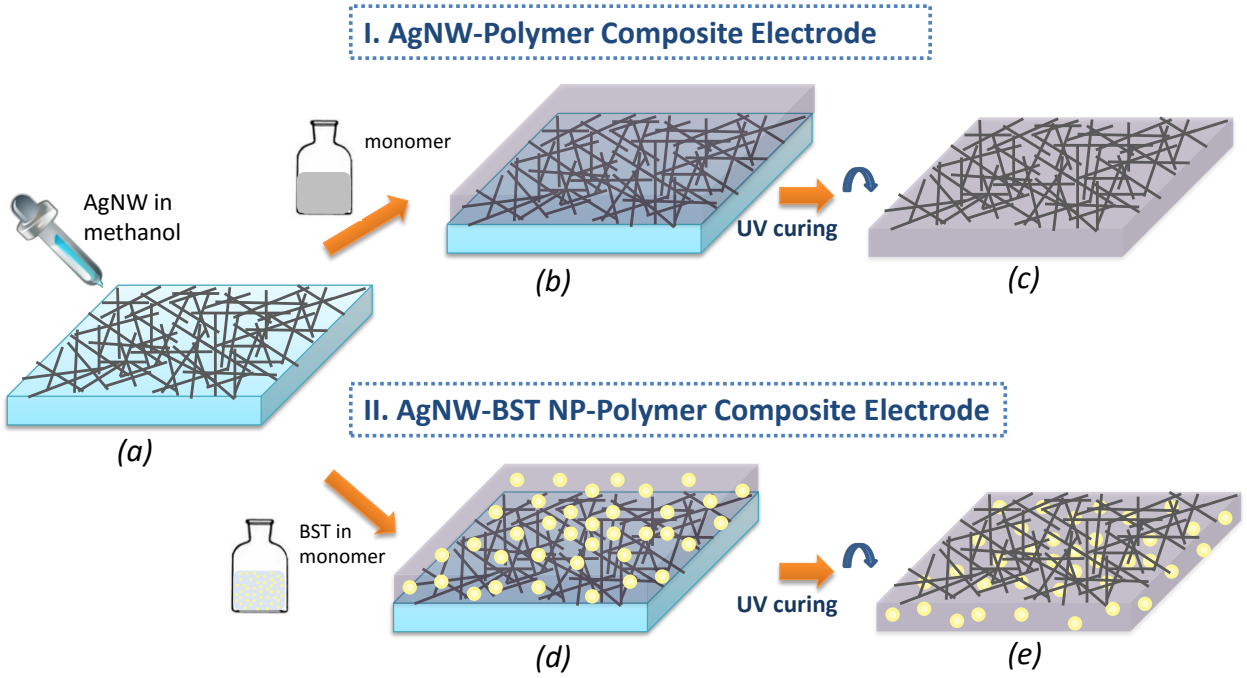

Figure 2.2: Fabrication process flow of (a, b, c) AgNW-Polymer, and (a, d, e) AgNW-BST-Polymer nanocomposite electrode.

As shown in Figure 2.2b, the mixed DMA monomer solution was applied on top of the AgNW film as prepared layers are exposed to ultraviolet radiation to convert the liquid monomer into a solid crosslinked polymer matrix through photochemically initiated free-radical polymerization. Then, the resulting AgNW-polymer film was peeled from the glass substrate, and a flexible transparent conductive electrode was obtained (Figure 2.2c). The AgNW-BST-Polymer

nanocomposite was prepared with a similar procedure, with the exception that 200nm BST nanoparticles were dispersed inside the DMA monomer solution at 2 wt% before being applied onto the AgNW film, as shown in Figure 2.2d and 2.2e. The matrix polymer of the composite electrode was chosen for its high transparency, high flexibility, and excellent bonding force between the polymer and AgNWs. The refractive index of the matrix polymer-only film was measured to be around 1.56, which is comparable to glass at 1.51.

2.3.2 Characterization of the Nanocomposite Electrodes

The distribution of AgNWs and BST nanoparticles in the nanocomposite electrodes were imaged by a SEM. Figure 2.3a shows the SEM image of the embedded AgNWs in the AgNW-polymer nanocomposite electrode, and Figure 2.3b shows the SEM image of the AgNWs polymer substrate incorporated with BST nanoparticles. Both AgNWs and BST nanoparticles were randomly distributed in the surface of the nanocomposite electrodes. The incorporation of 200nm BST nanoparticles enhanced the light out-coupling efficiency by Rayleigh scattering, which occurs when any particle with a size smaller than the wavelength of the light elastically scatters the light. The phenomenon of Rayleigh scattering is a result of the electric polarization of the BST nanoparticles. The light wave can be treated as an oscillating electric field that interferes with the charges within the BST particles and causes them to move in the same frequency. The nanoparticles then become a radiating dipole whose radiation is interpreted as the scattered light. The BST nanoparticles have a high refractive index, and the larger the difference of the refractive indexes between the matrix material and the nanoparticles, the larger the scattering effect. The BST nanoparticles' refractive index is around 2.40 to 2.43, whereas L4 matrix has n = 1.56. In addition, the scattered light is incoherent because the nanoparticles are randomly positioned. The

intensity of the scattered light is the sum of the squares of the amplitudes from individual particles and it can be expressed in equation (2.3) below:

$$I = I_{\circ}\frac{1+\cos^2\theta}{2R^2}\left(\frac{2\pi}{\lambda}\right)^4\left(\frac{n^2-1}{n^2+2}\right)^2\left(\frac{d}{2}\right)^6 \quad (2.3)$$

where R is the distance to the particles and Θ is the scattering angle. The intensity is proportional to the inverse 4th power of the wavelength and directly proportional to the 6th power of its size.

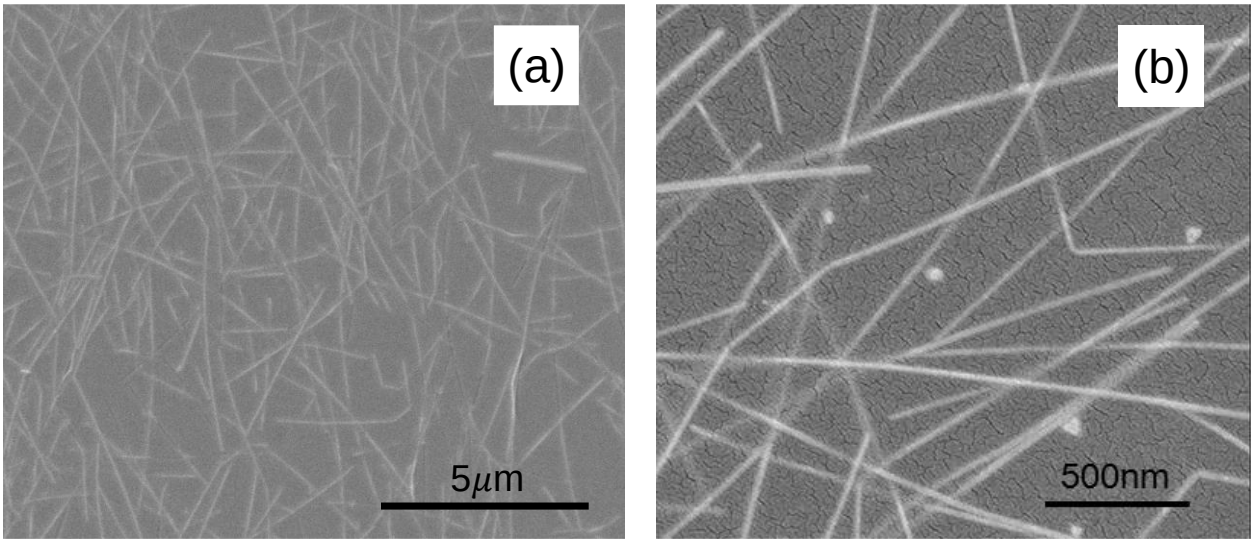

Figure 2.3: (a) SEM image of AgNWs randomly distributed in the polymer matrix; (b) SEM image of the surface of AgNW-BST-polymer nanocomposite.

SEM images show the existence and distribution of both AgNWs and BST nanoparticles on the surface of the nanocomposite substrates, while the morphology of the nanocomposites were studied using an AFM. Figure 2.4a shows the AFM image of the conductive surface of the AgNW-

polymer nanocomposite, and the average roughness of that surface was measured to be 7.62 nm. It is worth noting that the high viscosity of the monomer liquid allows it to fill in the pores of the AgNW network during the coating process, which results in a smooth surface of the AgNW electrode. Our method successfully solved the challenge of high surface roughness of AgNWs mentioned in many literatures. After incorporating BST nanoparticles into the polymer matrix, the conductive surface of the AgNW-BST-polymer nanocomposite substrate shows a smaller surface roughness (R_a~2.3 nm), which is close to ITO/glass (R_a~2.5nm) as shown in Figure 2.4b.

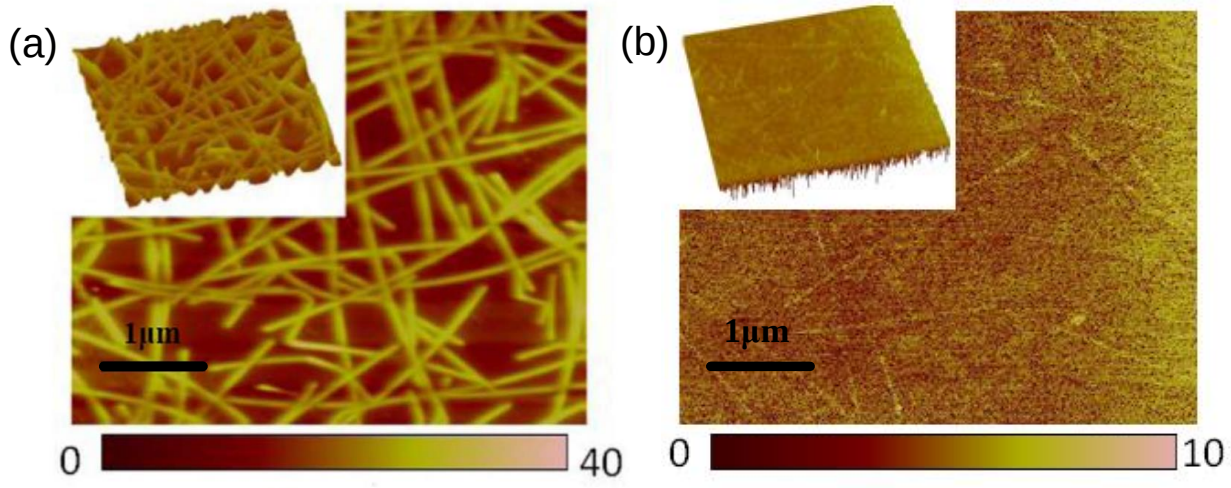

Figure 2.4: Tapping mode AFM images and 3D topographical images (inset) of the conductive surface of (a) AgNW-polymer, and (b) AgNW-BST-polymer nanocomposite. Adopted with permission from ref [64].

2.3.3 FDTD Simulation Result

2.3.3.1 Overview of FDTD

In order to gain some analytical insight on how nanoparticle scattering relate to the out-coupling efficiency of an OLED, the finite-difference time-domain (FDTD) method was employed. FDTD is based on solving Maxwell's equation and uses derivations of it to demonstrate the behavior of electromagnetic fields around a certain material or object.[65][66] In this method, space and time are merged as one entity rather than existing as two separate entities. Therefore, in FDTD solver, there is only one possible electromagnetic field arrangement surrounding an object at a given moment in time. According to Maxwell's equation, the electromagnetic field is composed of an electric field and a magnetic field. Since FDTD uses Maxwell's equation, it can be perceived that the change in an electric field in time is dependent on the change in the magnetic field across space.[67][68] FDTD has gained popularity due to its reputation as the simplest and most efficient way to model the electromagnetic field of a given material or object.

2.3.3.2 FDTD Simulation Setup and Results

In our application with light extraction enhancement studies, we employed the OLED 2-dimensional (2D) structure as shown in Figure 2.5a. In the simulation structure, 2% of 200 nm nanoparticles were randomly dispersed inside the polymer substrate. The refractive index of nanoparticles was set to 2.6. In this FDTD computational domain, the metal cathode was modeled as a perfect electric conductor and the absorption loss was not considered here by selecting the metal boundary condition. All the other materials such as organic layers and our composite substrates were modeled as the perfectly matched layer (PML). PML boundaries can absorb electromagnetic waves. The mesh resolution was 3 nm by 3 nm for the 2D FDTD simulation. The

size of the computational domain was 30,000 nm x 10,000 nm. The far field projection function was applied here and accounted for reflection and refraction that occurred at the far field glass-air interface. The traditional approach for simulating an OLED device utilizes the dipole model, which originated on the propagation of radiowaves above the conducting surface of Earth. The dipole source produces an electromagnetic field in Maxwell's equation. The position and direction of the dipole source is assigned in terms of the center position of their orientation through angles. The calculation assumes each material is a continuous homogeneous material instead of a dish mesh; therefore, we should keep in mind that the simulation result will deviate from theoretical results.

After running the simulation, the far field can be analyzed by averaging all the dipole orientation and locations and the result was obtained by integrating the far field intensity over the desired degree of the light emitted cone. The simulation result is shown in Figure 2.5b, where the x-axis represents the enhancement factor and the y-axis represents the wavelength. From the FDTD simulation result, the average enhancement factor for a PLED based on AgNW-BST-polymer (2 wt%, 200nm BST) nanocomposite substrate is 2.1. In other words, the PLED based on nanocomposite substrate has the potential to be 2.1 times as efficient as an ITO-based PLED.

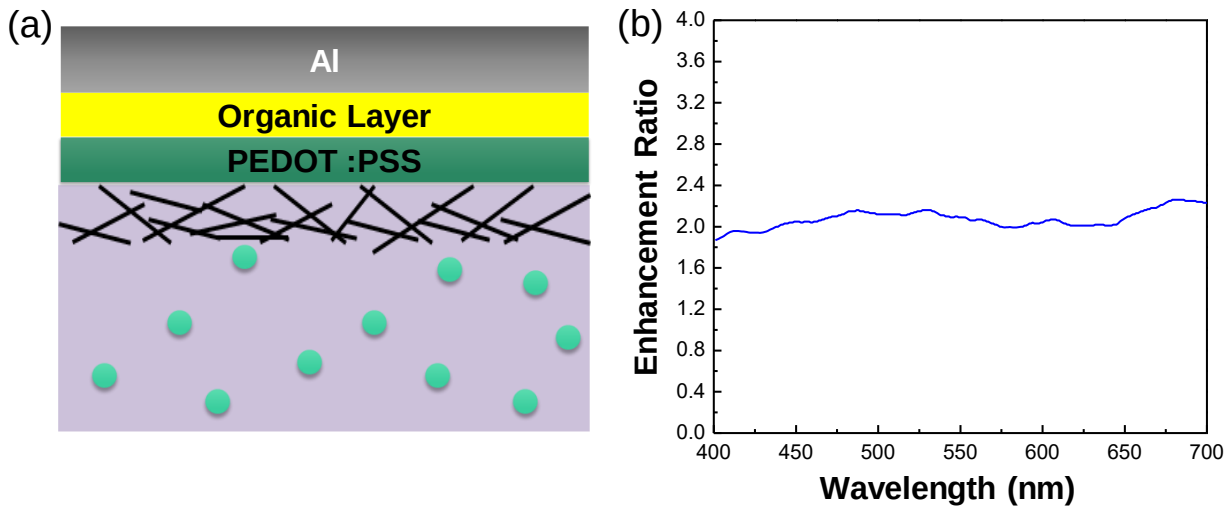

Figure 2.5: (a) Schematic illustration of the PLED structure used in 2D FDTD simulation. (b) Simulated enhancement factor in light extraction efficiency as a function of wavelength.

2.3.4 Light Out-Coupling Mechanism of AgNW-BST-Polymer Nanocomposite

Figure 2.6 shows a schematic representation of the light scattering modes in PLED based on the nanocomposite substrates. The proposed design could extract light that were originally trapped inside both ITO and glass. By replacing ITO with a AgNW electrode, the light that was trapped in the ITO layer due to the mismatch of the refractive index between the ITO and the glass was eliminated. Due to the nature of nanowires, AgNW thin film also serves as a light scattering center, and it is expected that the light be scattered out. In addition, BST nanoparticles will be embedded in the polymer substrate, which will deviate the light that was originally trapped in the substrate mode by changing the light propagation direction due to the presence of a scattering center by Rayleigh scattering mechanism. For a polymer-AgNW composite substrate, enhancement in light

extraction is attributed to high transmittance of the composite electrode and improved optical path length due to scattering of incident light[63].

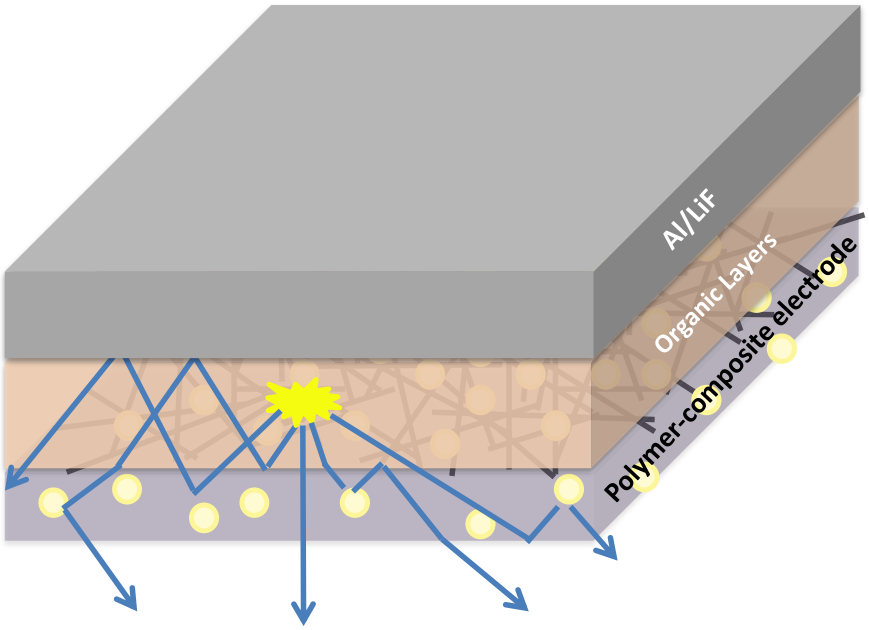

Figure 2.6: Schematic illustration of light scattering by nanoparticles in the AgNW-BST nanocomposite.

2.3.5 White PLED Device Performance

To demonstrate the enhancement in light out-coupling efficiency of the nanocomposite substrate, white PLEDs with a sandwich structure of Al/CsF/W EML/PEDOT:PSS/anode-substrate were fabricated. Here, Al (Aluminum) serves as the cathode, CsF as the electron injection layer, W EML (white emissive polymer) as the emissive layer, and PEDOT:PSS (poly(3,4-

ethylenedioxythiophene): poly(styrenesulfonate)) as the hole injection layer. PLEDs based on three different substrates were fabricated (Figure 2.7): (1) ITO/glass, (2) AgNW-Polymer nanocomposite substrate, and (3) AgNW-BST-Polymer nanocomposite substrate (diameter 200 nm BST nanoparticles, 2 wt%).

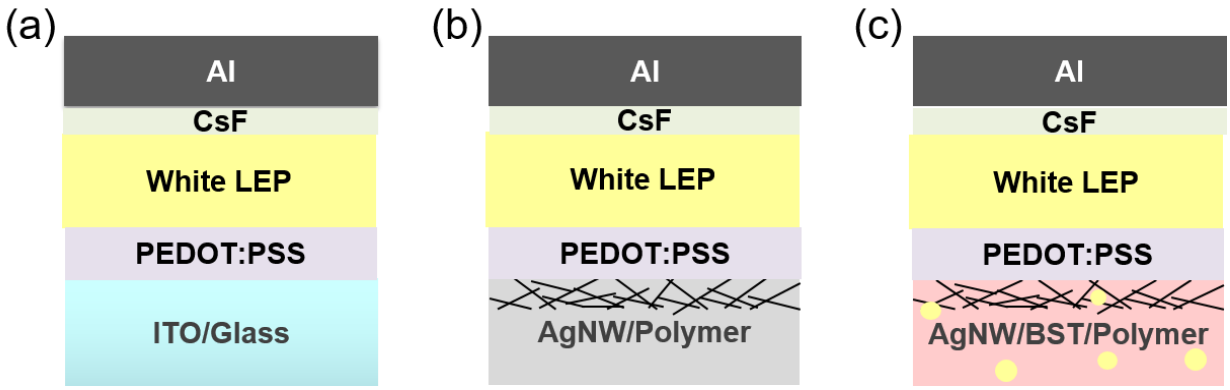

Figure 2.7: White PLED fabricated on (a) ITO/glass substrate, (b) AgNW-polymer substrate, and (c) AgNW-BST-polymer substrate.

Figure 2.8a shows the current density-bias voltage characteristic of the white PLED devices based on three types of substrate. The current density curves are almost identical for all three substrates above the turn-on voltage. However, AgNW-polymer nanocomposite substrate has the highest current density below the turn-on voltage among all devices. The higher leakage current observed in AgNW-polymer substrate is due to the higher surface roughness, as indicated in the AFM image. Above the turn-on voltage, all three PLEDs show exponential increase in current density; this is the result of the dual injection of electrons and holes.[69]

The luminance-bias characteristics of the three white PLEDs are presented in Figure 2.8b. AgNW-polymer based PLED has higher luminance than the ITO/glass-based device, which is a result of the out-coupling of the light that was originally trapped inside the ITO glass. The presence of AgNWs also help to scatter the light out. By adding BST nanoparticles, the luminance further increases, and the turn-on voltage decreases. The AgNW-BST-polymer substrate changes the light propagation path, which results in higher luminance and light extraction efficiency.

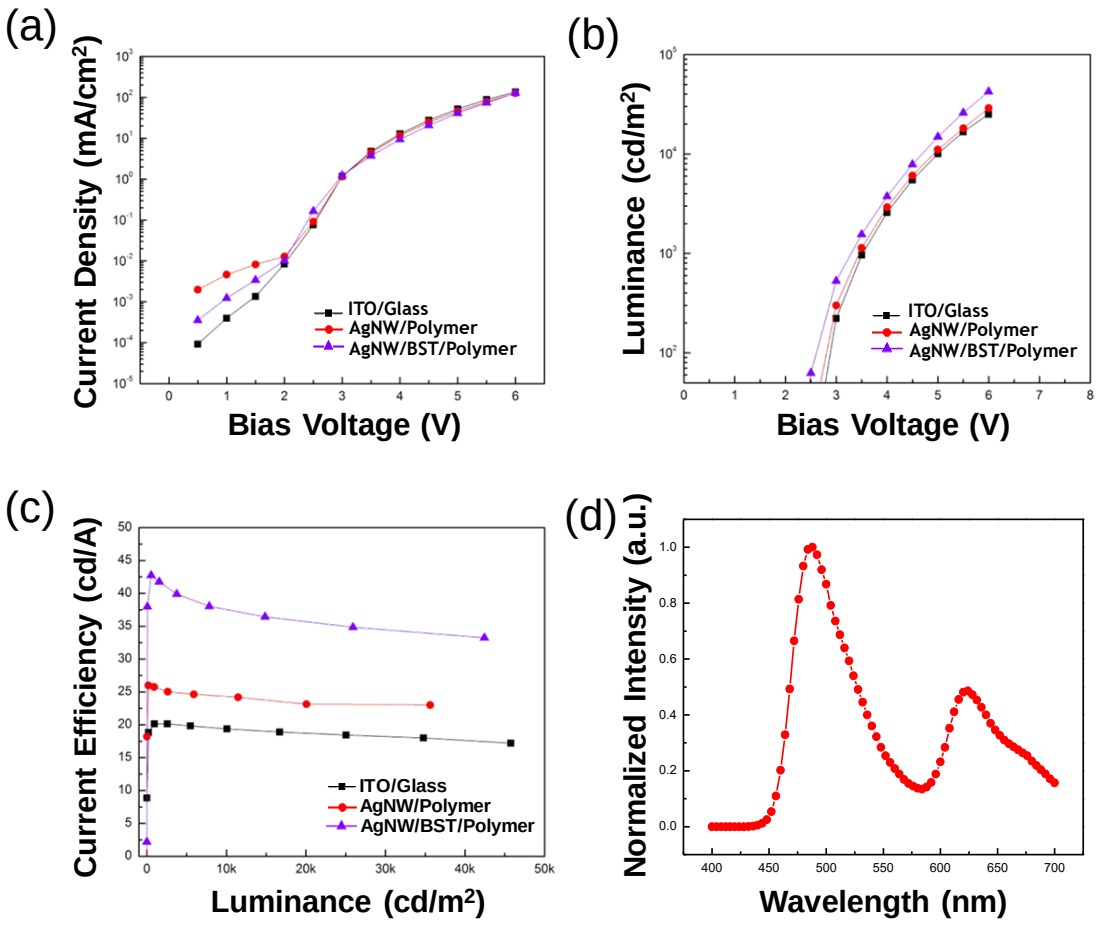

Figure 2.8: (a) I-V characteristic, (b) L-V characteristic, and (c) Current Efficiency vs. Luminance characteristic of white PLEDs on three specified substrates (ITO/glass in black, AgNW/-polymer

nanocomposite in red, and AgNW-BST-polymer nanocomposite in purple. (d) Normalized EL spectra of the white PLED based on AgNW-BST-polymer nanocomposite substrate.

Figure 2.8c shows the current efficiency-luminance characteristics of the white PLEDs, and the results are summarized in Table 2.1. It can be calculated that the improvement of the AgNW-polymer based device compared with ITO/glass based device is a 27% enhancement, and the improvement of the AgNW-BST-polymer based device compared with the ITO/glass based device is a 95% enhancement. Figure 2.8d demonstrates the normalized EL spectrum of the white PLED fabricated on a AgNW-BST-polymer nanocomposite substrate. It can be observed that the blue peak is twice as intense as the red peak in the white PLEDs.

Our experiment shows a 95% enhancement in EQE in AgNW-BST-polymer based PLED over the ITO/glass based PLED. Although the experimental result is similar to the simulated result at 110%, it should be noted that the simulation was done with the 2D FDTD method, which could only provide insights to help design the experiments. To get a more accurate estimation, 3-dimensional (3D) FDTD is required.

Substrate	CE (cd/A)	PE (lm/W)	EQE(%)
ITO/Glass	20.1	18.1	14.0
AgNW/Polymer	25.8	23.0	17.8
AgNW/BST/Polymer	41.7	41.9	27.3

Table 2.1: Device performance of white PLEDs based on specified substrates.

2.4 Conclusion

A flexible polymer based nanocomposite electrode with high light out-coupling efficiency is reported. The nanocomposite substrate incorporates AgNW in the surface of the polymer to provide high conductivity along with low surface roughness. BST nanoparticles (200 nm) were uniformly dispersed in the polymer substrate to serve as the scattering center and change the emitted light propagation path to increase the light coupling efficiency. FDTD simulation results show that the light extraction efficiency of the AgNW-BST-polymer nanocomposite substrate is 210%, which is close to the experimental obtained result of 195%. The maximum current efficiency of the AgNW-BST-polymer based PLED is 27.3 cd/A, and the corresponding power efficiency and EQE are 41.9 lm/W and 27.3%, respectively. The proposed nanocomposite substrate has demonstrated high enhancement in PLED device performance and has enormous potential to be used in future lighting products.

Chapter 3 . Electrolyte-Gated White Polymer Light Emitting Transistor with a Single-Component Polymer for Display.

3.1 Introduction

Solution-processable light emitting polymers (LEPs) are attractive for low-cost and large-size OLED displays and lighting.[45][70] In recent years, efforts have been put into developing a single-component white polymeric emitter by incorporating three-primary-color chromophores (red, green, and blue) or two-color chromophores (blue and yellow) into a single polymer chain.[71–74] This novel strategy prevents phase separation of the materials and overcomes the difficulty of controlling the doping level in the single layer and multilayer polymer-blended method.[70][75] In addition, a single-component white LEP leads to good color reproducibility of devices fabricated in different runs and a full emission spectrum with a broad range of colors that have a higher color rendering index. However, this strategy suffers significant synthetic challenges. Another approach to achieve white electroluminescence (EL) is to incorporate certain moieties that form excimers and electromers in polymer systems.[76–83] For this particular type of polymers, the emission from electromers excited by an electric field can only be detected in an EL spectrum but not in a photoluminescence (PL) spectrum. [76–83]

Although the emission from electric excited electromers has been reported for some conjugated material in a single layer[76–95] and multiplayers[96][97], the mechanism study of their formation is still in the initial stage. Generally, the conformations of molecular moieties are believed to be

changed with driving voltages.[98] This observation is solely based on the EL changes with varied driving voltages.[99][100] Recently, we have developed a three-terminal OLET devices: an electrolyte-gated OLET (EG-OLET), in which the device luminance can be simply controlled by an internal gate electrode at constant diode bias.[101] This approach can eliminate conformation changes caused by the driving voltage, providing an alternative way to investigate the origin of electomers.

Cambridge Display Technology reported Summation range polymers that can produce white EL in the device structure ITO/hole injection layer/interlayer/polymer/cathode. One of these polymers was characterized to be a single-component polymer (SCP) that emits white light in PLED devices through the formation of monomers, excimers, and electromers. Their red, green, and blue (RGB) primary colors were realized through RGB color filters, and the resulting emission spectra and color rendering index were measured and analyzed. This single-component polymer was further investigated in EG-OLET devices with full electrical and optical characterization.

3.2 Experimental Section

3.2.1 Materials

Poly (ethylene oxide) with 6000 g/mol (PEO6k), poly (ethylene oxide) with 300 000 g/mol (PEO300k) 300 000g/mol), and ferrocene were purchased from Alfa-Aesar. $LiCF_3SO_3$ (lithium triflate, 99.995%), and tetrabutylammounium tetrafluoroborate were purchased from Aldrich. Chlorobenzene and Acetonitrile was purchased from Sigma-Aldrich. Single-component polymer (SCP) was purchased from Cambridge Display Technology (Summation Batch number LEC-

White-1 050712.001). PEDOT:PSS (poly(3,4-ethylenedioxythiophene):poly(styrene sulfonate), Clevios 4083) were purchased from Heraeus. Indium–tin-oxide (ITO) glass substrates with a sheet resistance of 10 Ω/sq were purchased from Foshan Meijin Yuan glass technology CO., LTD. All materials were used as received. SCP solution was prepared with 10 mg/mL concentration in Chlorobenzene. Polymer Electrolyte (PE) solution was prepared with PEO(MW: 6k):PEO (MW, 300k) : $LiCF_3SO_3$ in a weight ratio of 1:1:0.2 in acetonitrile, with the concentration of 70 mg/mL.

3.2.2 Device Fabrication

ITO glass substrates were cleaned using sequential ultrasonication in detergent, deionized water, acetone and isopropanol. Each ultrasonic bath lasted for 20 min. After drying under a nitrogen flow, the ITO glass substrates were for 30 min in a UVO cleaner (Model No. 42, Jelight Company. Inc.). Then, PEDOT:PSS solution was spin coated onto ITO glass substrates at 4000 rpm for 60 s and annealed at 120 ˚C for 30 min in air. Subsequently, the SCP solution was spin-coated onto the PEDOT:PPS-coated substrates at 1500 rpm for 60 s and annealed at 120 ˚C for 30 min in a nitrogen-filled glove box with O_2 and H_2O levels below 0.5 ppm. The samples were then transferred into the vacuum deposition system (EcoVap, Mbruan, Inc.), in which a layer of aluminum cathode with or without LiF was deposited on top of SCP. Subsequently, PE solution was coated on top of the cathode at 1000 rpm for 60 s and annealed at 120 ˚C for 10 min in nitrogen atmosphere glovebox. Finally, on top of the electrolyte, a 100 nm aluminum film was deposited as gate electrode by thermal evaporation.

3.2.3 Device Characterization

Optical characterization: Photoluminescence (PL) characterization was performed using a Xenon lamp of 75W excitation power. The Absorption spectra of the mixtures were recorded in the range of 200 to 700 nm using a Shimadzu UV-1700 spectrophotometer.

A cyclic voltammetry (CV) experiment was performed to estimate the oxidation potential of the SCP polymer. A three-electrode system consisting of a platinum counter electrode, an ITO working electrode, and an SCE reference electrode was used here. The scan rate of 10mV/s is optimized to give a clear current-voltage curve. SCP was first dissolved in chlorobenzene and casted onto the ITO substrate to create a uniform film. The electrolyte was made with 0.1M $TBABF_4$ in acetonitrile. A trace of ferrocene is used as an external standard to determine the molecular energy level of SCP film.

The EG-OLET device was electrically contacted using a clamp (3M) with spring loaded Au-plated probes for anode, cathode, and gate contact, which were located in a dark box. All measurements took place inside a nitrogen atmosphere glovebox. A Si photodiode was used to measure the light output. The photocurrent and current density-voltage characterizations, were measured with a Keithley 4200 SCS (semiconductor characterization system. In all measurements, the cathodes of EG-OLETs were held at ground potential. The anode and gate voltage were applied to the ITO and gate Al electrode, respectively.

The EL spectral measurements of SCP diode and EG-OLET were performed using a spectroradiometer (Photo Research, PR655).

3.3 Results and Discussion

3.3.1 Absorption and Photoluminescence Spectra

The SCP (Summation Batch Number LEC-White-1 050712.001, Cambridge Display Technology) was utilized as received.[102] The 10 mg/mL solution of SCP in chlorobenzene was spin-coated onto glass substrates, forming a thin film with a thickness of 200nm. The ultraviolet-visible (UV-vis) absorption spectrum of the as-prepared film was measured to show a blue emission peak at 395nm with an onset at 470 nm (Figure 3.1a), resembling the UV-vis absorption spectra of polyfluorene derivatives.[103][104] The photoluminescence spectrum was also measured to exhibit a strong emission peak at 494 nm mirrored to its absorbance and a broad weak emission at 627 nm when excited at 375 nm. The major emission of the film likely originated from the monomer emission, while the broad weak emission was possible from the excimer emission of the conjugated length of this SCP. Based on UV-vis and photoluminescence spectra of this single-component polymer, we proposed its energy profile as depicted in Figure 3.1b.

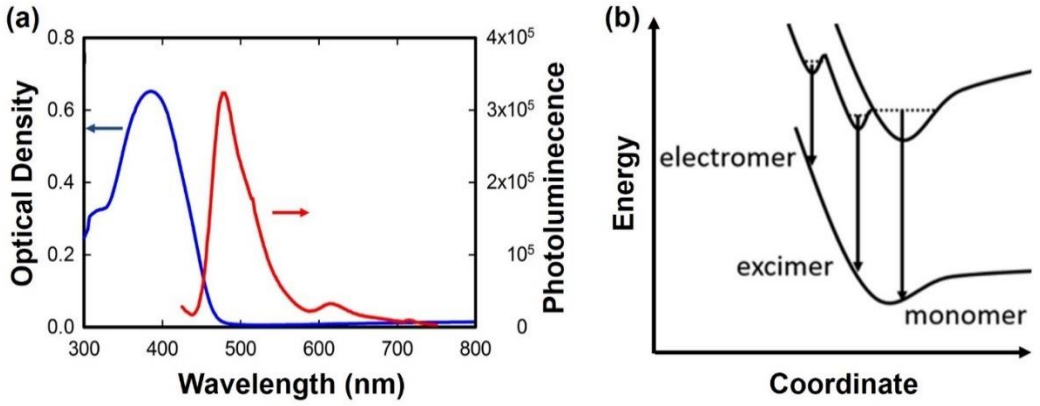

Figure 3.1: (a) UV-Vis absorption (blue curve) and PL (red curve) of SCP thin film (200 nm) on glass substrate. (b) Proposed energy profile of SCP monomer, excimer, and electromer.

3.3.2 Cyclic Voltammetry

Cyclic voltammetry (CV) measurement was performed on the SCP film deposited on ITO substrate, with ITO as the working electrode, platinum as the counter electrode, and a saturated calomel electrode (SCE) as the reference electrode. As shown in Figure 3.2, a major reversible oxidation peak at 1.1 V in reference to SCE was observed. From the onset value of the longest absorption wavelength, λ_{onset}, optical bandgap of SCP can be determined according to equation (3.1)[96]:

$$E_{BG} = 1242/\lambda_{\text{onset}} \qquad (3.1)$$

In Figure 3.1a, the absorption spectrum of SCP exhibits a peak at 385 nm and an absorption onset at 470 nm which correspond to a bandgap of 2.64 eV (3.2 eV for polyfluorene (PFO)).[105] The estimations of HOMO and LUMO of SCP can be made with equation (3.2) and (3.3):

$$\mathrm{E_{HOMO}} = \left[\left(\mathrm{E_{ox}} - \mathrm{E_{\frac{1}{2}(ferrocene)}}\right) + 4.8\right] \mathrm{eV} \qquad (3.2)$$

$$\mathrm{E_{LUMO}} = E_{HOMO} - E_{BG} \qquad (3.3)$$

where E_{ox} = 0.8 eV according to Figure 3.2, $\mathrm{E_{\frac{1}{2}(ferrocene)}} = (0.25 + 0.79)/2$=0.52 eV (ferrocene as the reference electrode). According to equation (2), the energy level of the highest occupied molecular orbit (E_{HOMO}) of this single-component polymer is calculated to be 5.08 eV (5.6 eV for PFO)[105]. From equation (3), the energy level of the lowest unoccupied molecular orbital (E_{LUMO}) of this polymer can be derived to be 2.44 eV (2.2 eV for PFO) [105]. Based on these results, we depict the energy levels of this SCP in Figure 3.3.

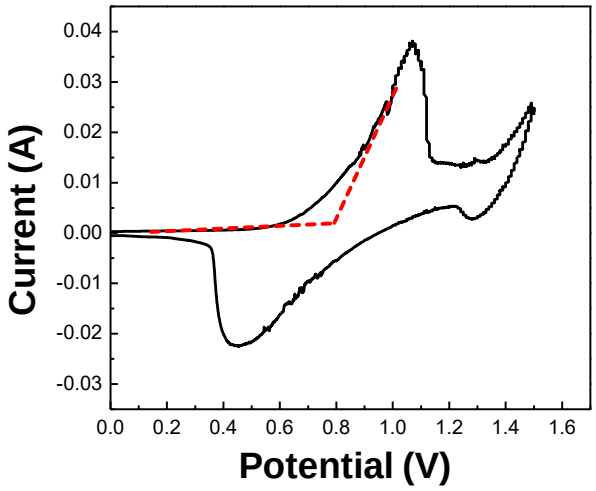

Figure 3.2: Cyclic Voltammogram (CV) of SCP film on ITO glass.

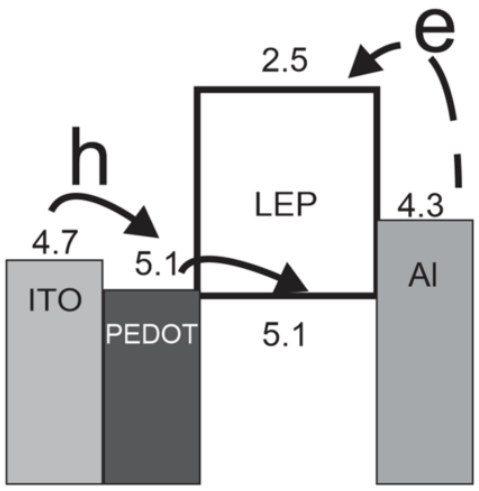

Figure 3.3: Energy alignment of SCP-based OLED.

3.3.3 Electroluminescence

The SCP was fabricated into organic light-emitting diodes with device structure ITO/PEDOT/SCP/Al. Briefly, polymer solution (10 mg/mL in chlorobenzene) was spin-casted onto PEDOT-coated ITO substrate at 1500 rpm, and then 50 nm of Al was thermally evaporated on top of the polymer film. As shown in the energy alignment diagram of the OLED (Figure 3.3), due to the energy mismatch between Al's work function (4.3 eV) and the lowest unoccupied molecular orbital (LUMO, 3.0 eV) of the SCP, the as-fabricated OLEDs gave rise to the weak EL (100 cd/m^2 at 4.3 V and 1000 cd/m^2 at 6.2 V), high turn-on voltage (3.8 V), and low efficiency (0.14 cd/A). A white emission was observed and photographed. Its EL spectrum was recorded using spectrometer PR655 and presented in Figure 3.4. A blue-green emission and a red emission peak at 465 nm and 630 nm are clearly visible in the spectrum. The red emission is remarkably different from the detected excimer emission observed in the PL spectrum. The red emission was then deconvoluted into two component as seen in Figure 3.4.

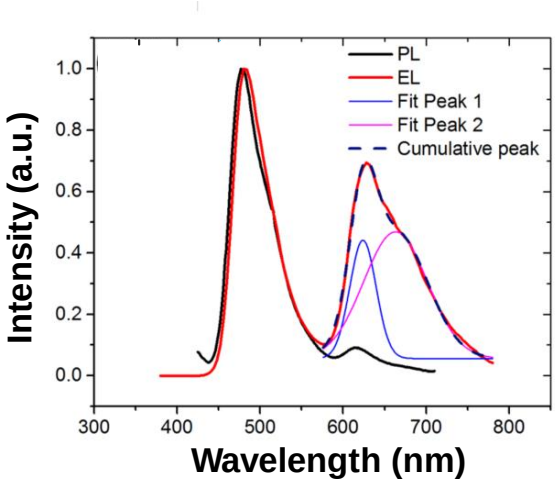

Figure 3.4: Comparison of PL and EL spectra of SCP normalized at blue-green peak. EL spectrum of SCP was deconvoluted into three peaks at 465 nm, 620 nm, and 685 nm, respectively.

One component peaking at 620 nm has the same wavelength rage as the weak excimer emission in the PL spectrum; another component peaking at 685 nm was not observed in PL, which was likely a result of electromer excited by an electric field.[76–95] Even though the wavelength of excimers is similar in both PL and EL, the excimer emission in EL is much stronger than those in PL. This density disparity could be due to the conversion from electromer to excimer in electric excitation, indeed of the conversion from excited monomer to excimer in photo-excitation. This picture can be envisaged in Figure 3.1b. Furthermore, the Commission Internationale de l'Eclairage (CIE) coordinates of the white OLEDs were measured to be (0.36, 0.34), as plotted in the CIE color space chromaticity diagram in Figure 3.5. The light emission of white OLEDs is slightly red to natural white light with a color temperature of 6247K.

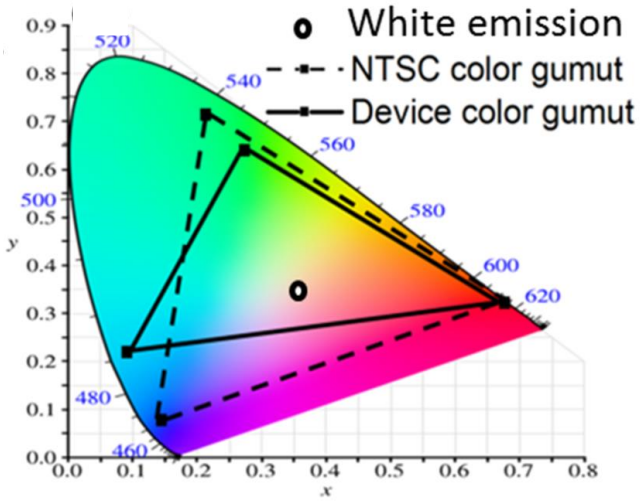

Figure 3.5: CIE color space chromaticity diagram of white EL and three primary colors of SCP diodes with reference to NTSC standard color gamut.

The white light emitted from the device was filtered using red, green, and blue color filters, respectively, in order to emit three primary colors. As the emission spectra shown in Figure 3.6 (device photo images shown in inset), the emitted red light ranges from 560 to 800 nm and peaks at 630 nm; the emitted green light ranges from 480 to 620 nm and peaks at 515 nm; and the emitted blue light ranges from 450 to 540 nm and peaks at 465 nm. The blue and red emission peaks match the white emission peaks of 465 and 630 nm. The CIE coordinates of CIE RGB primaries were measured to be (0.68, 0.32), (0.27, 0.64), and (0.09, 0.22), respectively, as plotted in the color space chromaticity diagram in Figure 2D. The color gamut of this full color OLED is about 73% of the NTSC (National Television System Committee) standard. In order to display colors having higher color gamut, white emission with sharper peaks or color with narrower transmission bandwidths will be needed.[106][43]

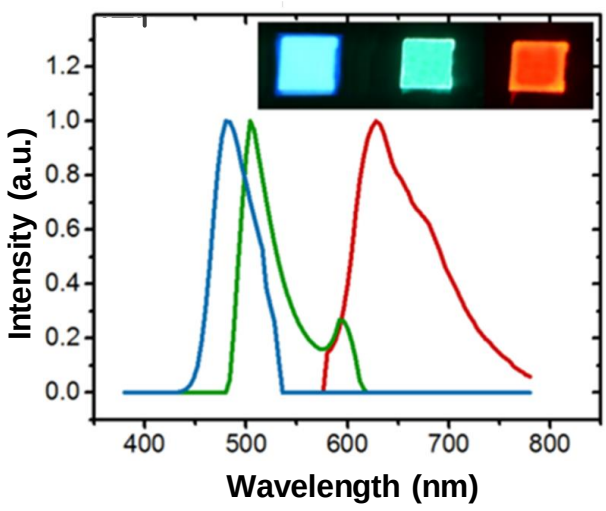

Figure 3.6: Spectra of three primary colors of SCP diode after being filtered with RGB color filters.

3.3.4 Electrolyte-Gated Organic Light-Emitting Transistors

Following our previous EG-OLET technology,[101] we fabricated electrolyte-gated diodes with this SCP. On top of the ITO/PEDOT/SCP stack, a thin porous Al layer was deposited as the cathode of OLED. On top of the porous Al cathode, a solution polymer electrolytes (PE, concentration: 70 mg/mL) comprised of poly(ethylene oxide) (PEO, molecular weight 6000): PEO (molecular weight 300,000): $LiCF_3SO_3$ in a weight ratio of 1:1:0.2 was spin coated. An Al gate electrode was then evaporated on top of the PE layer to form an EG-OLET device as photographed in the inset of Figure 3.7. Figure 3.7 illustrates a three-dimensional device structure. The corresponding circuit is depicted in Figure 3.8, where capacitor (C_s) is physically connected and monolithically integrated to an OLED. Because of the interface between PE and the SCP through a porous Al electrode is adjusted by applied gate voltage to modulate the electron injection, the EG-OLET can be disserted into an n-type driving transistor stacked on the emitting layer monolithically.

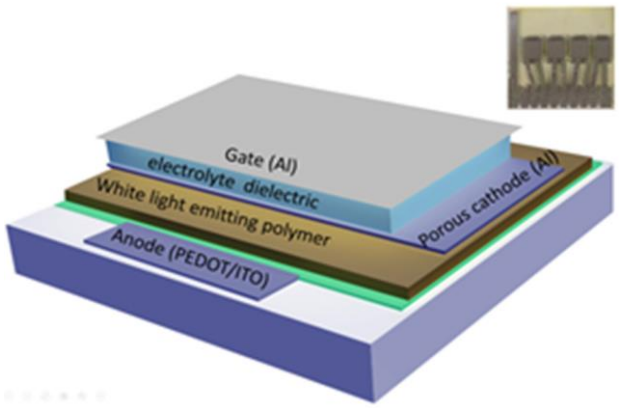

Figure 3.7: Schematic illustration of the three-dimensional EG-OLET device. The inset is the photographic image of the EG-OLET device.

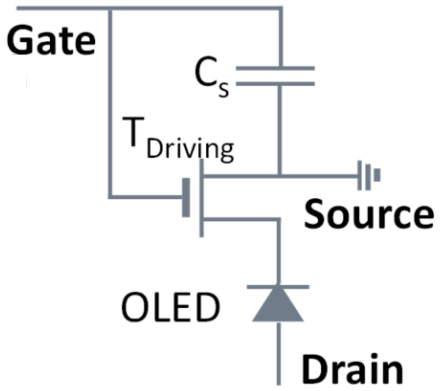

Figure 3.8: The circuit diagram of EG-OLET.

The as-fabricated EG-OLET device was characterized in a nitrogen-filled glovebox using Keithley 4200 semiconductor characterization system. In all measurements, the cathode of the device was held at ground potential. The transfer characteristics was measured by applying 8 V at the ITO anode in reference to cathode and sweeping the voltage at the gate electrode from -4 to 7 V, then from 7 to -4 V. As shown in the transfer curve of current density between drain and source(*J*) and luminance(L) verses gate voltage(V_g) in Figure 3.9a, *J* increased from 10 mA/cm^2 at V_g = -4 V, to around 110 mA/cm^2 at V_g = 7 V, indicating a current on/off ratio of about 10 and an increase of channel conductance by 10 times. The L vale of white emission increased from 0.3 cd/m^2 at -4 V, to around 6500 cd/m^2 at 7 V, with a optical contrast of aournd 20,000. The coresponding current efficiency (C.E.) is plotted in Figure 3.9b, showing a maximum C.E. of 6 cd/A at positive V_g and and a zero efficiency at negative V_g (no emission). These observations can be interpreted by the following: the ions in PE redistributed to stabilize the electrochemical doping of the SCP in the vicinity of porous cathode as a result of applied gate potential.[101] PE acts as dielectrics and forms a capacitor with a gate electrode and OLED cathode. The luminescence modulation is 3 orders of

magnitude greater than the current density modulation of EG-OLET. This can be rationalized as the balanced electron/hole injection is the determinant for efficient device and brightness,[107][108] while the electron injection contributions to current density are limited in hole-dominant diodes.[101]

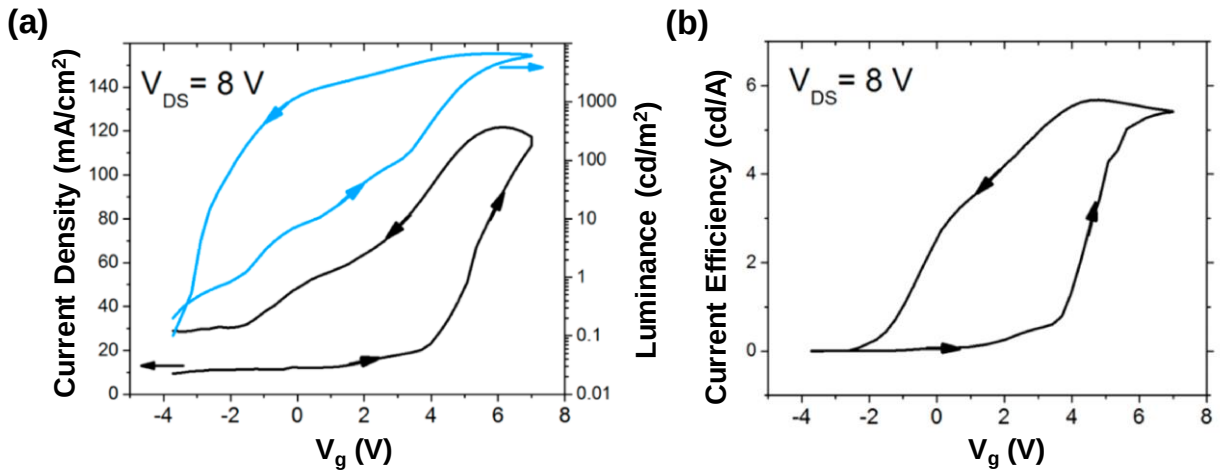

Figure 3.9: (a) Current density and luminance transfer characteristics of EG-OLET under V_{DS} = 7 V. (b) The current efficiency of EG-OLET calculated based on the curve in (a).

The hysteresis of *J* and L in EG-OLET was observed and displayed in Figure 3.9a and Figure 3.9b, which is primarily attributed to the nature of slow ion motion and is also observed in other ion-containing devices, such as electrolyte-gated transistors[109], ion-containing perovskite LEDs[110], and OLED devices incorporating electrolyte materials[111]. The slow ion motion, and thus device response, can be accelerated with elevated temperature.

The output characteristics of EG-OLETs was measured with anode voltage (in reference to cathode) sweeping from 0 V to 8 V with different V_g (-2, 0, 2, 4, 6, and 8 V). The *J*-V curves are shown in Figure 3.10a and the L-V curves in Figure 3.10b. The *J*-V curve shows typical diode rectification behavior, with an increase of *J* verses increased V_g. *J* reaches a maximum value of around 10 mA/cm^2 at V_g = -2 V, and increased to 120 mA/cm^2 at V_g = 8 V. On the other hand, the luminance increased much more significantly: as can be seen from Figure 3.10b, at V_g = -2 V, the maximum L is below 1 cd/m^2; at V_g = 0, 2, 4, 6 and 8 V, the maximum L increased, respectively, to 50 cd/m^2, 450 cd/m^2, 1000 cd/m^2, 5800 cd/m^2, and 6000 cd/m^2. These results are consistent with the above-described transfer characteristics, indicating, again the effective gate modulation of electron injection for tuning carrier balance and consequent electroluminescence tailoring.

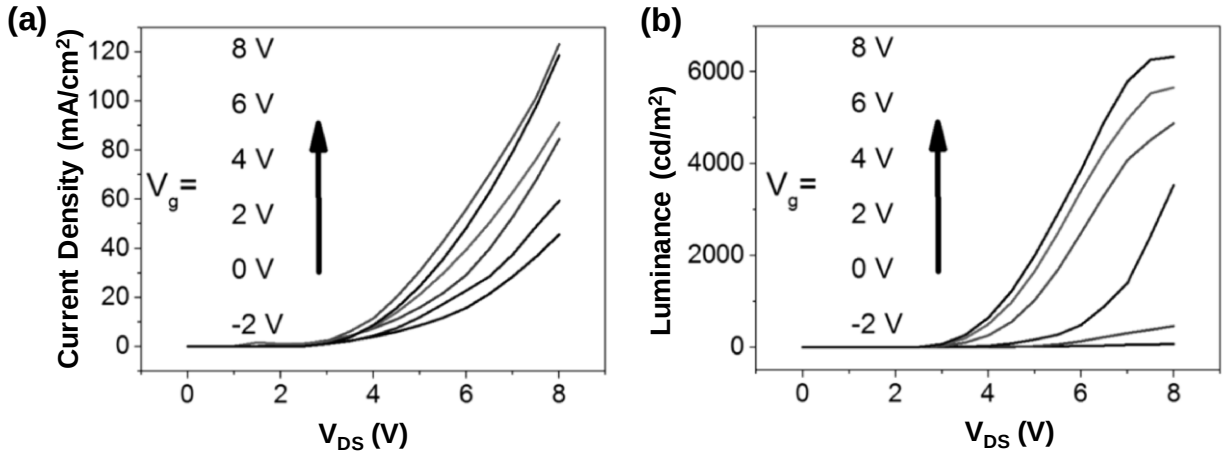

Figure 3.10: The current density (a) and luminance (b) output characteristic of EG-OLET with varied V_g from 0 to 8 V with the interval of 2 V.

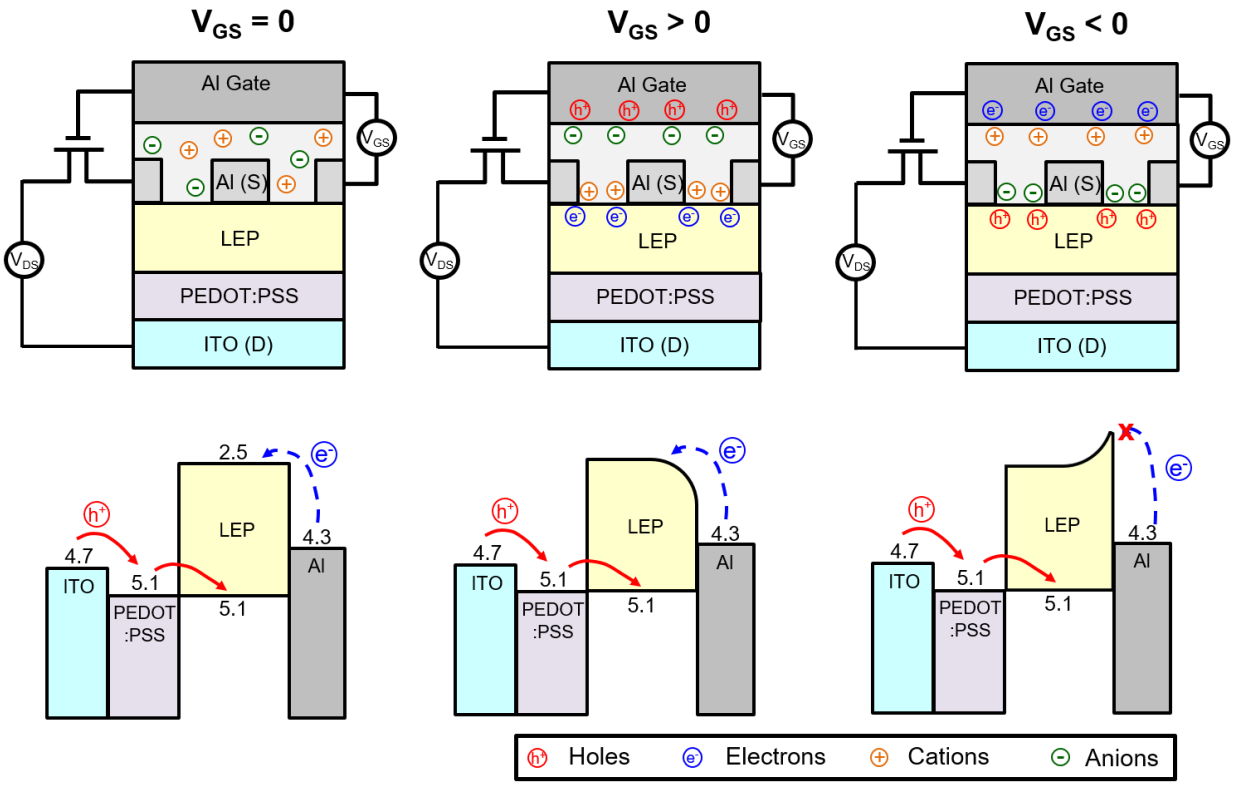

Figure 3.11: Illustration of ion distribution and band diagrams of EG-OLETs for (a, b) $V_{GS} = 0$, (c, d) $V_{GS} > 0$, and (e, f) $V_{GS} < 0$.

3.3.5 Working Mechanism

Figure 3.11 is produced to help better understand the working mechanism of the SCP-based EG-OLET device. When a voltage is applied between the gate electrode and the source electrode (V_{GS}), the ions inside the electrolyte are polarized and arranged themselves forming two Helmholtz electrical double layers (EDLs) at the interface of Al/electrolyte and electrolyte/LEP.[112] Since the Al source is made porous, the electrical double layer was able to interact with the LEP layer. A positive voltage between source and drain electrode is fixed at 8 V (V_{SD} = +8 V). As shown in

Figure 3.11a and 3.11b, when V_{GS} = 0 V, the EG-OLET works like a normal OLED. Here, hole injection barrier is negligible; the work function of PEDOT:PSS is well aligned with the HOMO level of LEP. However, the electron injection is hindered due to the large energy barrier between the work function of Al electrode (4.3 eV) and LUMO of LEP (2.5 eV). Due to limited electron injection, the unbalanced charge carriers result in low device efficiency when V_{GS} = 0 V.

When V_{GS} > 0 V as shown in Figure 3.11c and 3.11d, the electrolyte is polarized and anions inside the electrolyte move to the electrolyte/gate interface due to an attraction from the gate electrode. On the other end, the cations move toward the Al source. Because Al source is porous, the cations are able to transverse the Al source electrode and dope the intrinsic LEP. The electron injection barrier is now lower and lead to efficient electron injection and result in improvement of device electroluminescence.

When V_{GS} < 0 V, due to the excess electrons present in the Al gate film, the cations inside the electrolyte migrate to the electrolyte/gate interface and form a EDL; in the meantime, anions in the electrolyte move to the electrolyte/LEP interface. The formation of EDL at the electrolyte/LEP interface results in p-doping of LEP emitter. The P-doped LEP made the vertical EG-OLET into a hole-only device. The holes injected from ITO hop to PEDOT:PSS, then injected into LEP and finally moved to Al source without combining with any electron. In summary, when V_{GS} > 0 V, it helps to improve electron injection and greatly improves the device performance. When V_{GS} < 0 V, the device performance is greatly decreased due to quenching and imbalanced of electron and holes.

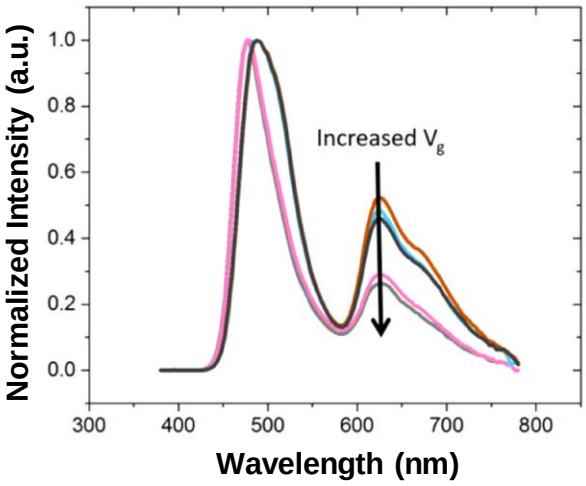

Figure 3.12: Normalized EL spectra at the blue-green peak of EG-OLET with varied V_g from 0 to 8 V with the interval of 2 V.

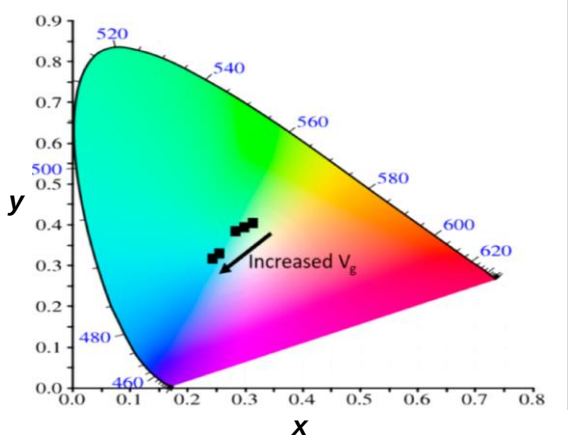

Figure 3.13: The CIE coordinate shift of SCP diode in CIE color space cromaticity diagram with the increase of V_g.

3.3.6 Gate-Modulated Electromers

With gate-modulated EL, the spectra of EL at different gate potential were recorded with PR655. The normalized spectra were measured at different V_g (8, 6, 4, 2 and 0 V), and shown in Figure 3.12. A decrease in red emission ratio was observed with higher V_g (i.e. higher luminance), with the corresponding CIE coordinate change shown in Figure 3.13. As discussed in EL section, these red emissions arose from excimers and electromers. These electric field driven red emissions were measured to exhibit the decrease with increased drain voltage (from 3 to 9 V) in OLETs (Figure 3.12). This could be due to the preferred conformation of blue emissions in the range of 3 to 9 V, similar to those reported results for poly(N-vinylcarbazole) under 12 V.[82] In EG-OLET with consistent drain voltage at 6 V, the red emissions decreased with improved electron injection modulated by increasing gate modulation from 2 to 8 V with the interval of 2 V. This indicates that the formation of electromers is favored in less balanced electron hole condition, which usually leads to low current efficiency. For example, one can expect the formation of electromer when an electron enters into the hole dominant system.[113] With more electrons, and then more balanced electron and hole, the formation of electric excited monomers become prevailing.

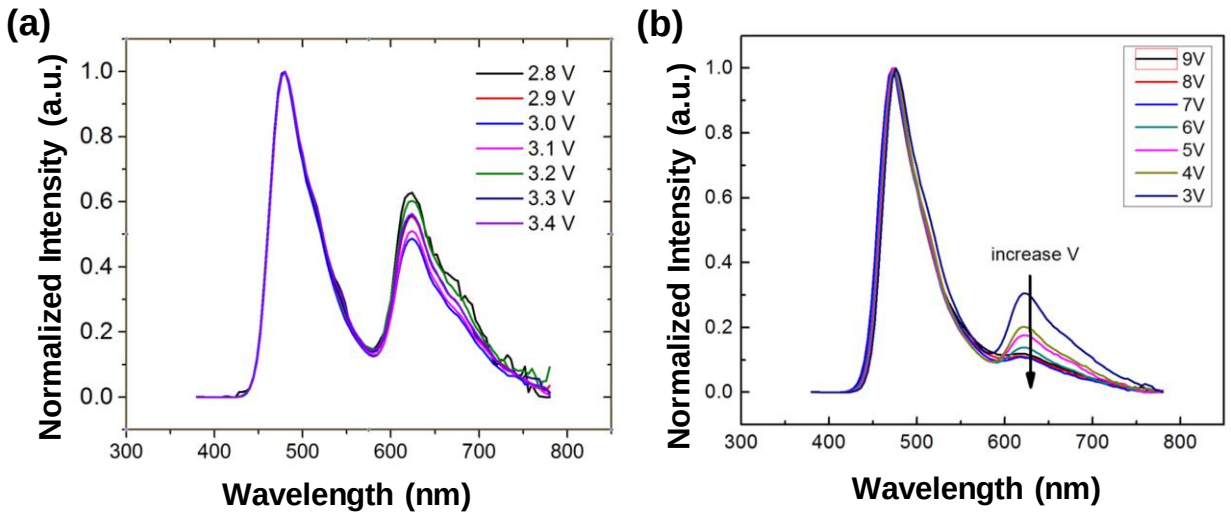

Figure 3.14: EL spectra of SCP diode under different driving voltages a) from 2.8 V to 3.4 V with the interval of 0.1 V, and b) from 3 V to 9 V with the interval of 1 V.

3.4 Conclusion

In summary, a SCP received from Cambridge Display Technology was characterized with optical spectra and cyclic voltammetry measurements to estimate its energy levels. The EL of this SCP in a device structure ITO|PEDOT|polymer|Al is white with the CIE coordinates of (0.36, 0.34) and a color temperature of 6247 K. The EL spectrum was deconvoluted into blue-green emission and a red emission, which peaked at 465 nm and 630 nm, respectively, ascribed to the exited monomers, excimers and electromers. The CIE coordinates of RGB primaries were measured to be (0.68, 0.32), (0.27, 0.64), and (0.09, 0.22), respectively, about 73% of NTSC.

The SCP light-emitting diodes were demonstrated to be gate tunable by fabricating a PE layer on top of a porous thin Al cathode of the PLED. The white EL of EG-OLET increased from 0.3 cd/m^2

at -4 V, to around 6500 cd/m^2 at 7 V, with an optical contrast of around 20,000, corresponding to a maximum C.E. of 6 cd/A at positive V_g and a zero efficiency at negative V_g. These results were explained by the improved electron injection, which was due to the formation of ohmic contact between porous Al eletrode and electrochemical n-doped SCP; futhermore, the ohmic contact was stabilized by gate potential redistributed ions of PE, analogous to the operating mechanism in light-emitting electrochemcial cells.[114][115]

The white EL spectra of EG-OLET were recorded with gate potential that varied from 0V to 8V with an interval of 2 V. The normalized spectra based on blue-green emission peaks show the decreasing red emissions attributed to electric excited excimers and electromers when the gate voltage went up. These results indicate that the generation of electromers might be favored at a carriers imbalanced condition, besides the conformation effect of SCP.[82][98]

Chapter 4 . A Transparent Perovskite Light Emitting Touch-Responsive Device

4.1 Introduction

Sensors have been widely studied for applications in healthcare, human-activity monitoring, and robotics, and have proven to be a vital tool in detecting and collecting data for various forms of activities. Among these, tactile sensors acquire information through physical touch.[116][117][118] A tactile sensor may measure properties such as temperature, vibration, texture, shape, and force.[119] The common responses used in tactile sensors include capacitive, piezoresistive, piezoelectric, inductive, and optical responses.[119] These sensors generally require additional electronics to receive and display the output readings from the sensors, incurring a complicated system that includes physical analog sensor data acquisition, embedded data processing, and end user interactive visual application.[120] The capacitive touch sensor installed on virtually all smartphones is perhaps the most notable example. The required computations, control circuits, and optical readouts lead to high manufacturing cost and limit the application breadth of the sensors. An alternative method to receive a direct output signal without the need of wiring complicated external electrical components is through an instantaneous optical feedback.[121]

Sensor feedback through visual means are not new, but the technology behind powering and creating these visual components are continuously evolving. Light-emitting diodes have recently set the standard for what a visual component could be in terms of illuminance, longevity, and accuracy, while organometal halide perovskite has recently been actively investigated as the new emissive material thanks to their high absorption coefficient, wide absorption wavelength range,

tunable bandgaps, high color purity, high ambipolar charge mobility, and extended carrier lifetime.[122][24][10] The highest external quantum efficiency (EQE) reported so far for the perovskite light emitting diodes (PeLED) is 8.53%.[123][6][124] The organometal halide perovskite can easily be solution processed, and the process does not require high temperatures.[125][11] These characteristics make the organometal halide perovskite an important material for the next generation large-area, pixelated information displays.[126][127]

Here we introduce a light emitting touch-responsive device (LETD) that integrates an organometal perovskite light emitter and a transiently formed electrical contact to achieve instantaneous visualization of pressure mapping. The pero LETD is composed of two laminated layers via a spacer: the bottom layer is a sandwich structure of substrate/ITO/PEDOT:PSS/$MAPbBr_3$:PEO, where ITO (indium tin oxide) is a transparent electrode, PEDOT:PSS is the hole injection layer, and $MAPbBr_3$:PEO (a composite of methylammonium lead bromide and polyethylene oxide) is the emissive layer. The top layer is a transparent composite electrode comprised of silver nanowires (AgNW) embedded in the surface of polyurethane (PU) to provide a smooth and stable electrode surface. The LETD is rigid when a glass slide is used as the substrate and flexible when the glass slide is replaced with a polyethylene terephthalate (PET) film. Local pressure applied to the AgNW-PU composite electrode puts it in contact with the $MAPbBr_3$:PEO layer to form an instantaneous electrical connection and produces electroluminescent emission from the perovskite nanocrystals in the $MAPbBr_3$:PEO layer. This pero LETD can thus produce an instantaneous readout of the pressure, and the mechanism can be extended for touch tracking and mapping.

A critical element of the electroluminescence is the ability to form a stable electrical contact when the top composite electrode is pressed to make contact with the $MAPbBr_3$:PEOlayer; this enables charges (electrons here) to be injected from the electrode into the semiconductor layer. In

conventional thin-film electronic devices, the metal-semiconductor interface is usually formed permanently during the device fabrication. Numerous studies have been focused on how to improve the interface quality in order to achieve high device functionality. Our LETD is the first semiconductor device where the metal-semiconductor interface is transiently and reversibly formed. The transience of the interface is also investigated.

4.2 Experimental Section

4.2.1 Materials

N,N-dimethylformamide (DMF) (anhydrous, 99.8%), 2,2-dimethoxy-2-phenylacetophenone (photoinitiator), and poly(ethylene oxide) (average Mw≈600,000) were purchased from Sigma-Aldrich. Lead(II) bromide (99.999%) was purchased from Alfa Aesar. The methylammonium bromide was purchased from "1-Material Inc." Low conductivity poly(3,4-ethylenedioxythiophene): poly(styrenesulfonate) (PEDOT:PSS) (CleviosTM P VP AI 4083) was purchased from H.C. Starck Inc. Silver nanowires were from Zhejiang Kechuang Advanced Materials Co. Siliconized urethane acrylate oligomer (UA) and an ethoxylated bisphenol A dimethacrylate (EBA) were supplied by Sartomer. All materials were used as received.

4.2.2 Fabrication of Perovskite LETD

A final concentration of 500 mg/mL Br-pero precursor solution was prepared by dissolving $PbBr_2$ and MABr in a 1:1.5 ratio in DMF.[128] PEO was dissolved in DMF to obtain a final concentration of 10mg/mL. The Br-pero precursor and PEO precursor then mixed for 2 hours at 60°C under

ambient conditions. After assimilating, the two precursors were mixed in a desired ratio and stirred under 60°C for 30 minutes before use. The ITO/glass substrates (10 ohm/sq) were cleaned subsequently with acetone, detergent water, deionized water, acetone, and 2-propanol for 60 minutes with sonication, and then they were dried with air and treated with oxygen plasma at 100 W power for 2 minutes before use. The PEDOT:PSS solution was spin-coated onto the ITO/glass or ITO/PET at 4000 rpm and annealed at 120 °C for 20 minutes. Next, the MABr-$PbBr_2$-PEO precursor was spin-coated at 2000rpm, followed by 3 minutes annealing at 60°C. The 100 μm transparent Scotch double-sided tape was used as the spacer and was placed on two sides of the substrate. Lastly, the transparent AgNW-PU electrode was laminated on top of the spacer and resulted in a transparent perovskite light emitting touch-response device.

4.2.3 Fabrication of AgNW-PU Composite Electrode

A thin uniform film of AgNW with 20 Ω/□ sheet resistance was prepared by spreading a dispersion of AgNW (0.5 wt %) with Meyer rod onto a releasing substrate. Then the AgNW film was annealed for 8 minutes at 165°C. Next, a precursor solution consisting of 100 weight parts of UA, 20 parts of EBA, and 1 part of the photoinitiator was coated on top of the AgNW film.[47] The coatings were then sent to a UV lamp and cured at 2.5 W/cm^2 intensity. After the film was cured, the transparent composite electrode with AgNW incorporating into PU substrate was then peeled off from the releasing substrate.

4.2.4 Characterization of $MAPbBr_3$:PEO Film, Perovskite LETD, and AgNW-PU Electrode

Scanning electron microscope (SEM) images were taken by a JEOL JSM-6710F scanning electron microscope. Atomic force microscope (AFM) images were performed by a Bruker dimension icon scanning probe microscope. Photoluminescence (PL) spectra were carried out by using Photon Technology International Spectrophotometer. Absorbance spectra were collected by Shimadzu UV-1700 spectrophotometer.

The pero LETD was fabricated and tested under ambient environment. Pero LETD was driven and the electrical reading was recorded with a Keithley 2400 and Keithley 2000 SourceMeter unit. All characterization tests were performed at room temperature.

The Young's modulus of the AgNW-PU electrode was measured with a TA RSA3 DMA. A rectangular shaped film sample with a thickness of 90 μm and a width of 5 mm was loaded onto the DMA with an active length of 10mm. A tensile stress-strain curve was measured at a stretching rate of 1 mm s^{-1} at room temperature.

4.3 Results and Discussion

4.3.1 LETD Device Fabrication

The LETD was fabricated under ambient conditions from solutions, according to the schematic in Figure 4.1. The LETD device resembles a typical pero LED structure but with one major difference: the top electrode and the emissive $MAPbBr_3$:PEO layer are separated via a spacer. The top

electrode is a AgNW-PU transparent composite prepared via a transferring process that embeds the nanowires in the surface layer of the PU film.[47] The composite electrode exhibits low sheet resistance (~10 Ohm/sq) and low surface roughness (R_a ~2.3 nm) and retains the mechanical flexibility of the PU film. The composite electrode could be physically manipulated (i.e. bent or twisted) without losing its surface conductivity. The lower section of the LETD was constructed by successively spin-coating PEDOT:PSS and the pero precursor solution on an ITO/substrate. The pero precursor solution contains PEO, lead bromide ($PbBr_2$), and methylammonium bromide (MABr) co-dissolved in DMF at appropriate ratios to form pinhole-free $MAPbBr_3$:PEO composite films. Obtaining a small pero grain size in the composite film is essential in limiting the diffusion length (L_D) of the excitons and decreasing the possibility of exciton dissociation into electrons and holes.[124] Finally, a spacer of 100 μm was used to laminate the top electrode and the $MAPbBr_3$:PEO composite film, creating a gap that serves as a pressure module for the device. The top and side views of the resulting LETD device are shown in the inset of Figure 4.1.

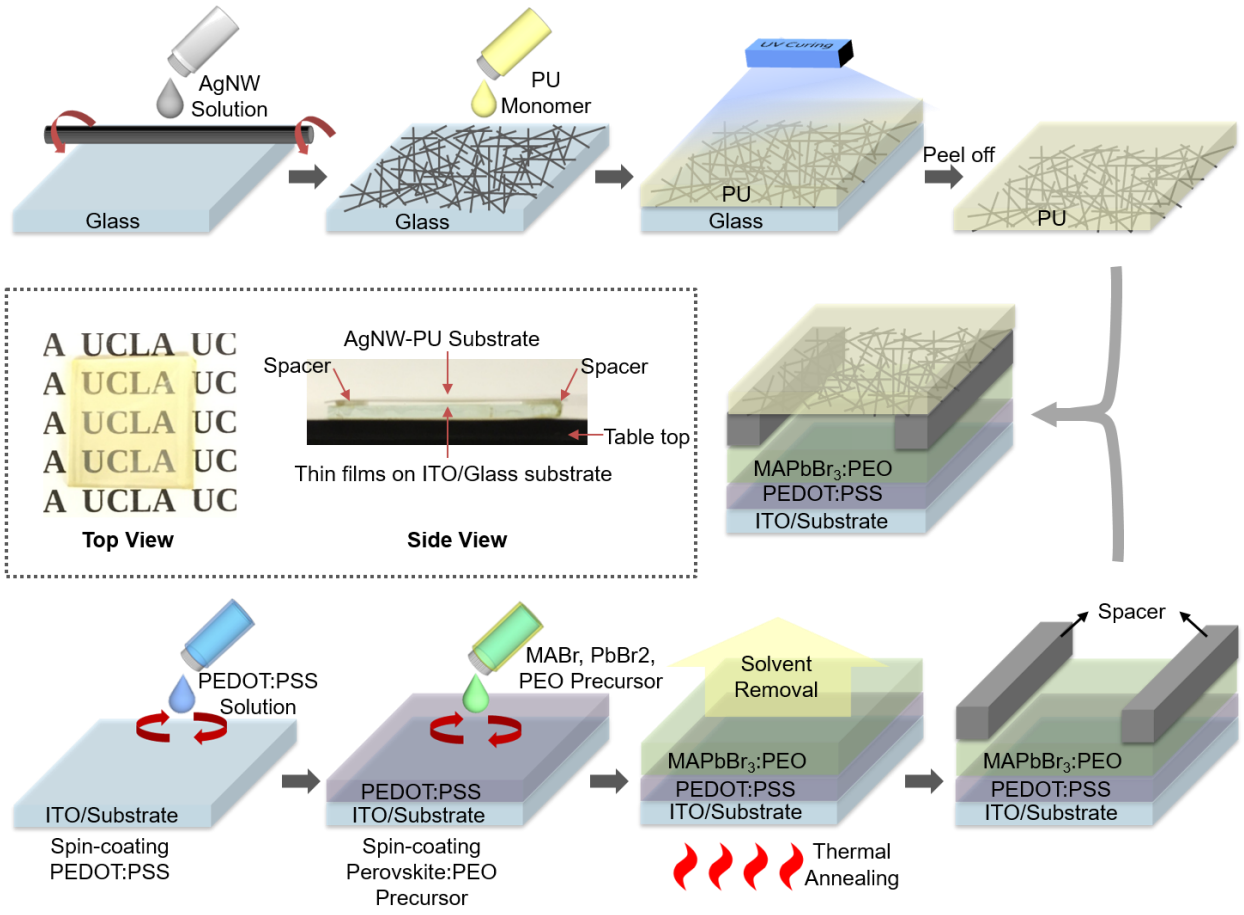

Figure 4.1: Schematic illustration of the fabrication of a perovskite LETD. Inset: Photographs of an LETD viewed from top and side.

4.3.2 AgNW Composite Electrode

The transparent composite electrode of PU and AgNW is necessary as the top electrode to obtain pressure mapping. Silver nanowire's ability to form a highly conductive percolation network at high transmittance and its high mechanical flexibility make it an ideal candidate as the conductive material for the top electrode of the pero LETD.[129][130] Due to the minute amount of AgNWs embedded on the surface of the PU, the mechanical properties of the composite are still determined

by the PU itself, which has an elastic modulus of 31 MPa and elongation at break of 116% (Figure 4.2). The hydrogen bonding moieties in PU offer strong binding with AgNW, which enables a complete transfer of AgNW during preparation of the composite electrode and preserves the AgNW percolation network in the surface of the PU film.[47] As a result, the AgNW network remained intact during repeated 3M Scotch® adhesive tape peeling tests as well as during constant bending and stretching tests. After 100 cycles of repeated adhesion and peeling, the sheet resistance of the AgNW-PU composite electrode remained unchanged.[47] Repeated stretching up to 16% strain on the AgNW-PU electrode resulted in only a small increase in sheet resistance; the sheet resistance returned to its original value when the AgNW-PU electrode reverted to its original dimensions.[131] The thickness of the PU film is approximately 100 μm in this study for ease of handling, pressure sensitivity, and location mapping resolution. Considering that the stability of AgNW has been a concern by many in the field, we tested the stability of the AgNW-PU electrode with successive exposure to 2-propanol (IPA) and acetone, and observed little degradation of sheet resistance.[131] In addition, the thermal stability of the AgNW electrode was also tested at 150°C for 240 hours; it was found that the sheet resistance remained the same. A possible explanation may be that the inter-nanowire junction is better protected in the composite electrode than those exposed on the substrate surface.[62]

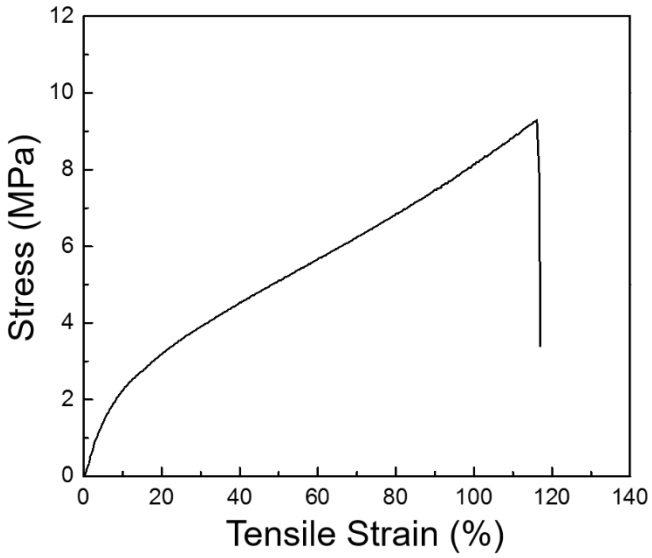

Figure 4.2: Stress-Strain curve of AgNW-PU at room temperature.

4.3.3 $MAPbBr_3$:PEO Composite Film

The bottom layer of the LETD is comprised of a $MAPbBr_3$:PEO composite film. Ideally, the pero grain size should be controlled to restrict the diffusion length (L_D) of the excitons to decrease the possibility of exciton dissociation into the electrons and holes. PEO was chosen here because its hydrophilic property enabled the perovskite precursor solution to spread out smoothly, which helped to increase the nucleation density of perovskite.[22] Furthermore, PEO hindered diffusivity of the perovskite precursor at the solvent drying stage during the spin-coating process, which led to a small grain size and smoother surface.[23] By spin-coating a mixed solution of the PEO additive and the perovskite precursor at a desired speed, smaller pero grains were obtained, thus created a pinhole free pero film. With an optimal $MAPbBr_3$:PEO weight ratio of 1:0.3 in DMF, along with the one-step-spin coating method, a 200 nm thick $MAPbBr_3$:PEO composite film was attained - as

shown in the cross-sectional scanning electron microscope image (SEM) in Figure 4.3a. A detailed study on pero film morphology and grain size in relation to $MAPbBr_3$/PEO ratio was performed (Figure 4.4). It was found that as the PEO concentration increased, the pero crystal size became smaller, while the surface coverage of the film improved. At the optimized $MAPbBr_3$:PEO weight ratio of 1:0.3, the grain size of $MAPbBr_3$ reached under 20 nm in diameter while the surface coverage of the pero film was larger than 90%, as indicated in Figure 4.3b. The average surface roughness (R_a) of the $MAPbBr_3$:PEO (1:0.3) composite film was below 3 nm for a 200 nm film. Adding PEO in the pero precursor solution here was impeccable to slow down the growth and aggregation of the perovskite crystals, thus promoting a smooth and uniform film and preventing device shorting or current leakages.[22][132] Besides PEO's effect on pero grain size, Zhao et al. reported that PEO also served as a scaffold to crosslink with neighboring pero grains to form a composite network that protected the pero film from humidity.[133] Lastly, Li et al showed that the interaction between -OH and Br- groups enhanced the dispersion of perovskite in the PEO polymer matrix.[60] In Figure 4.5, the smooth $MAPbBr_3$:PEO composite film was verified by an atomic force microscope (AFM) image. The UV-vis absorption and photoluminescence (PL) emission spectra of the $MAPbBr_3$:PEO composite film are shown in Figure 4.6. Intense green emission was observed under 350 nm excitation with peak wavelength at 529 nm and full width at half maximum (FWHM) at 18 nm. The FWHM is the narrowest reported thus far for green PeLED.[134]

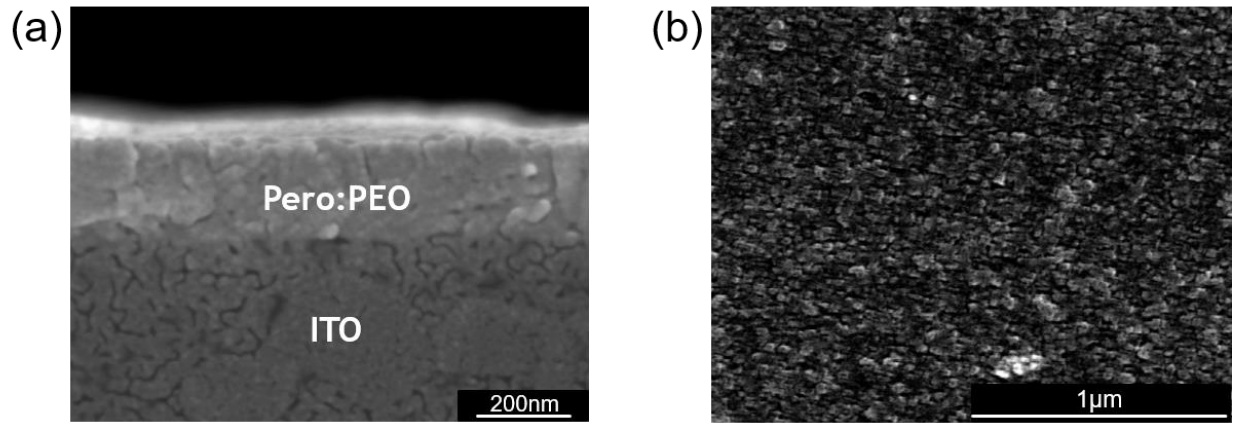

Figure 4.3: Characterization of a MAPbBr3:PEO (1:0.3 weight ratio) film on ITO: (a) cross-sectional SEM image, (b) top down SEM image

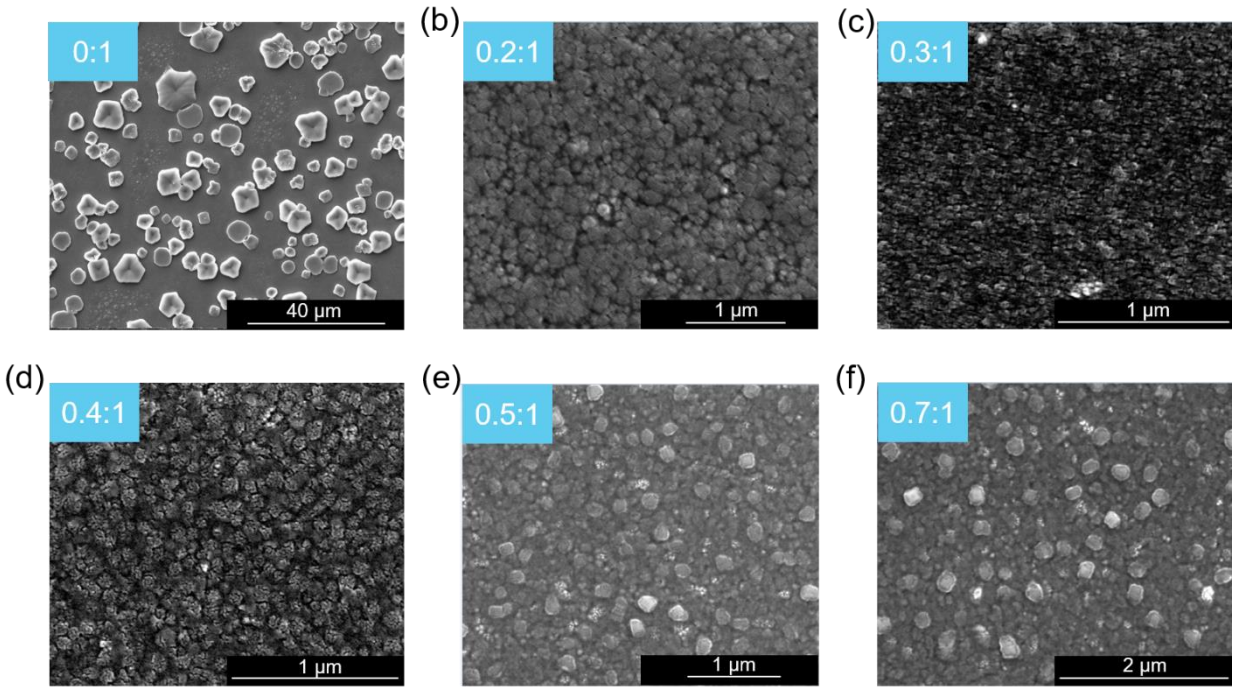

Figure 4.4: SEM images of PEO/Pero composite thin films with PEO/Pero ratio of (a) 0:1, (b) 0.2:1, (c) 0.3:1, (d) 0.4:1, (e) 0.5:1, (f) 0.7:1.

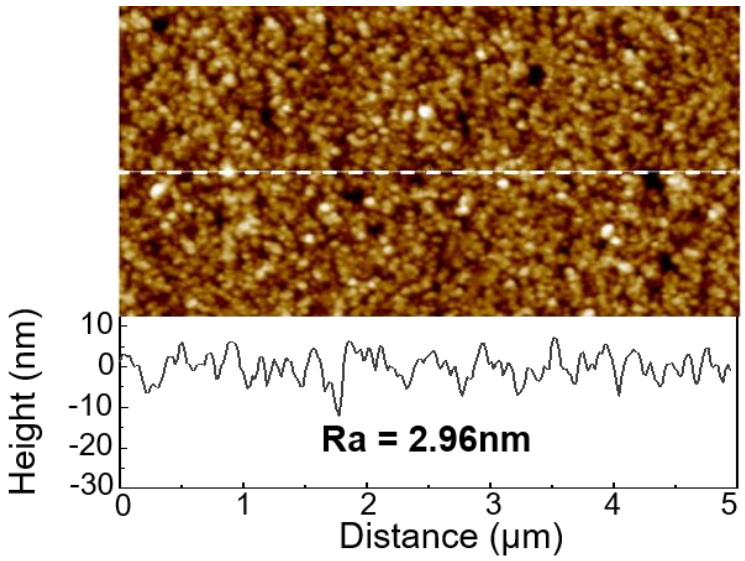

Figure 4.5: AFM image of a $MAPbBr_3$:PEO (1:0.3 weight ratio) film on ITO.

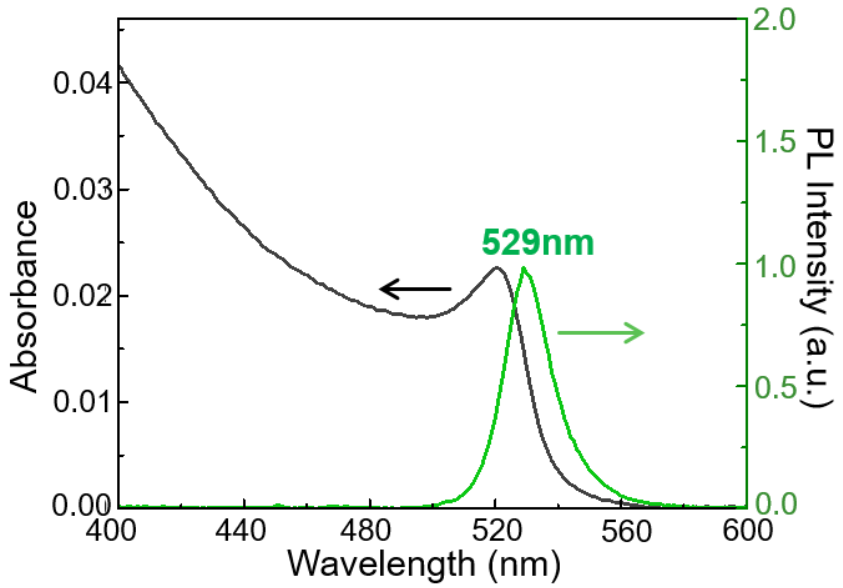

Figure 4.6: Absorbance and photoluminescence spectra of the $MAPbBr_3$:PEO composite film.

4.3.4 LETD's Operating Mechanism

The operational mechanism of the LETD is illustrated in Figure 4.7. When pressure was applied onto the AgNW-PU surface, a convex, out-of-plane deformation was created in the composite electrode that enabled the AgNWs to make contact with the pero film. The voltage applied between the ITO and the composite electrode forced the injection of electrons from the AgNWs, and holes from the ITO into the pero film. The recombination of the electrons and holes produced excitons, which radiatively decayed to produce photons as determined by the bandgap of the $MAPbBr_3$ nanocrystals (2.3 eV).[122] When the pressure was removed, the AgNW-PU electrode returned to its original flat shape, the AgNWs were detached from the pero film, and thus, the photon production was terminated. The LETD showed instantaneous light emission in the region that pressure was exerted, as shown in Figure 4.8a, and remained in the "OFF" state in areas without pressure applied. In addition, once the electrical contact was formed, the LETD provided consistent current and luminance under constant voltage supply.

To assess the pressure sensitivity of the LETD, dynamic pressure measurements were performed. A series of forces were applied on the LETD under 3 V, and the output current remained constant (Figure 4.8b). In addition, the luminance intensity remained unchanged with the applied forces. The results indicated that the electrical contact between the AgNWs and the pero film was insensitive to the applied pressure, as long as they are physically attached.

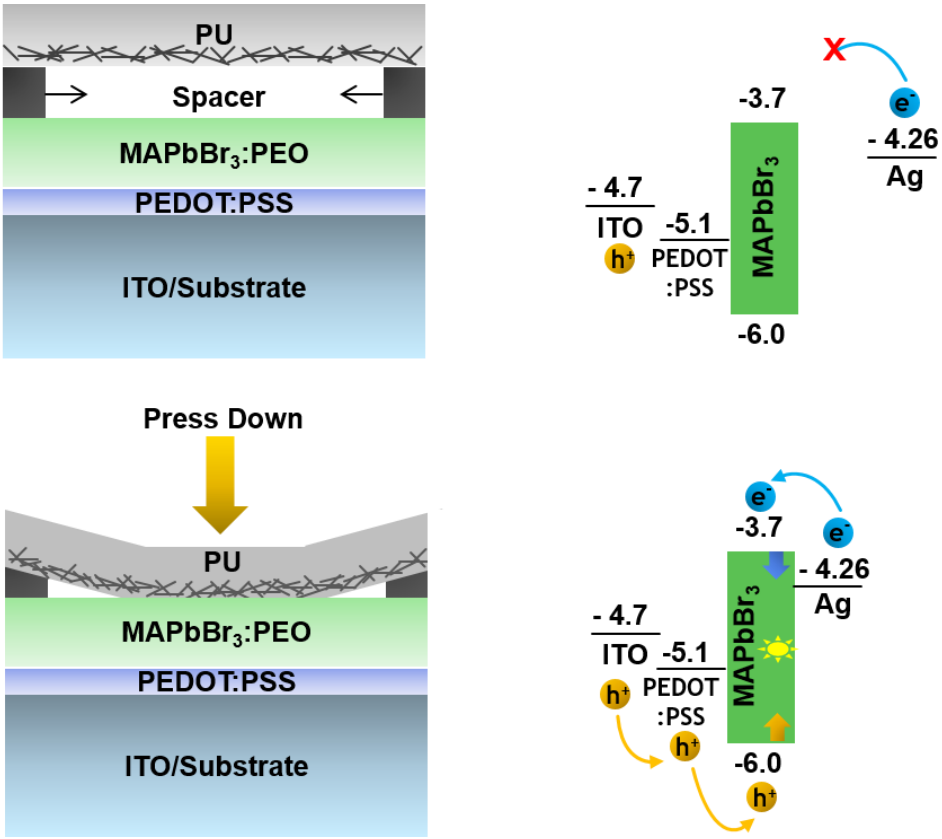

Figure 4.7: Schematic illustration of switching an LETD and the band diagrams of the materials involved.

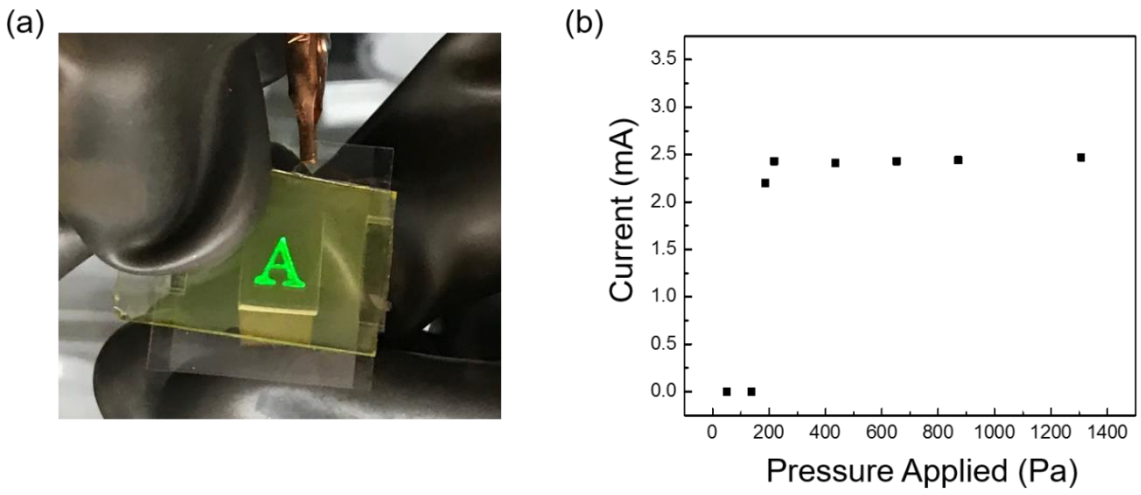

Figure 4.8: (a) Photograph of an LETD under 4 V bias when an "A"-shape stamp is pressed onto the surface of the AgNW-PU top electrode. (b) Transient current response at low to high pressure range.

4.3.5 LETD Device Performance

The LETD was constructed by a layered structure of ITO/PEDOT:PSS/$MAPbBr_3$:PEO/AgNW-PU, where ITO served as the anode and AgNW as the cathode. The luminance (L)-voltage (V)-current density (J) characteristics of the green LETD are shown in Figure 4.9a. The LETD has a low turn-on voltage of 2.5 V with luminance over 1000 cd/m^2 at 6 V. The electroluminescence (EL) spectrum of the pero LETD (Figure 4.9b) demonstrated an ideal color-saturated green emission with peak maximum at 532 nm, Commission Internationale de l'Eclariage (CIE) color coordinates of (0.19, 0.77) and a narrow FWHM of ~21 nm. The slight red-shift observed in the EL spectrum when compared with the PL spectrum (Figure 4.9b) may be due to a small shift of

electron states to lower energies while the hole states shift to higher energies when an external electric field is applied.[135]

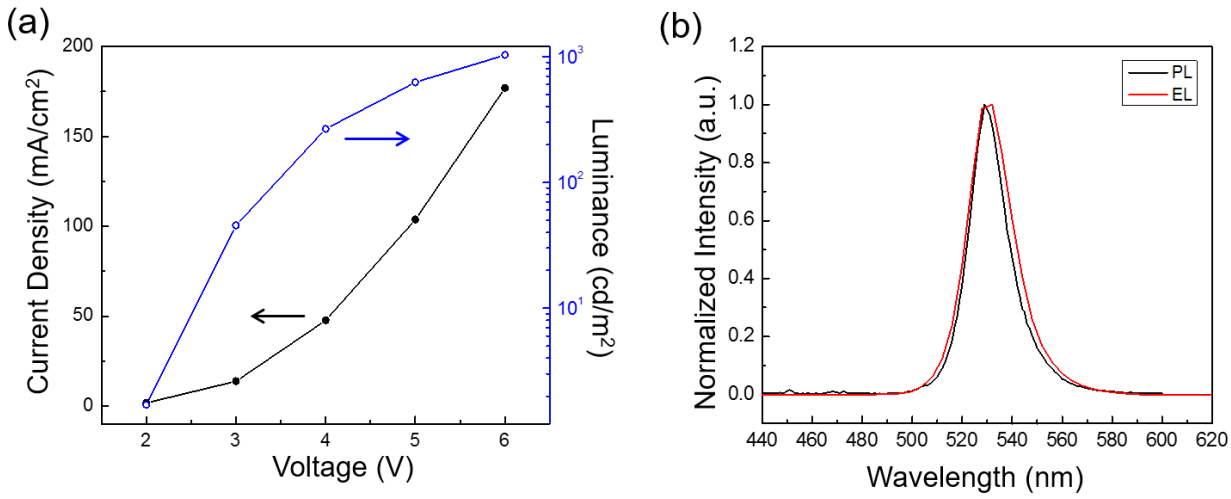

Figure 4.9: (a) L-V-J characteristic of the LETD. (b) Comparison between (black) PL spectrum of $MAPbBr_3$:PEO film and (red) EL spectrum of the pero LETD.

4.3.6 Cyclic Test of LETD Layer Contact

To demonstrate that the physical contact between the AgNW and the pero film was formed instantaneously when an external pressure was applied, the output current signals were recorded under continuous loading and unloading of an external pressure under a constant velocity. Figure 4.10a shows the measured luminance during 1100 cycles of repeated pressure ON and OFF under a frequency of 1.67 Hz; the brightness of the LETD device remained stable and no decrease in luminance was observed. The current response over the continuous loading and unloading cycles also remained stable (Figure 4.10b). The unwavering device performance after repeated attaching and detaching of the contact between AgNW and the $MAPbBr_3$:PEO layer can be accredited to the

robustness of the electrodes and the emissive layer. Incorporating AgNW into PU provided a sturdy, reliable, and compliant electrode, which was confirmed by the Scotch tape test, while the PEO additive in the pero layer resulted in a pinhole free and smooth perovskite emissive layer with sufficient cohesive force to prevent detachment of the $MAPbBr_3$ nanocrystals. Together, these two aspects contributed to the robustness of the LETD, and enabled stable contact forming and deforming over 1000 times.

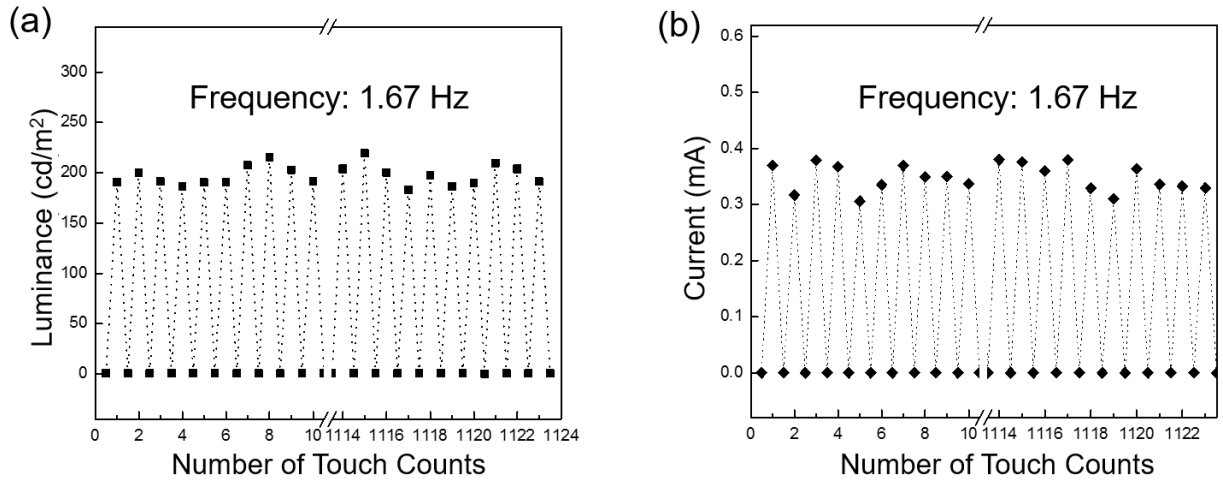

Figure 4.10: Durability test of an LETD with mechanical load applied repeatedly at 1.67 Hz. The output is presented with (a) luminance variation and (b) current variation.

4.3.7 Transient AgNW-Perovskite Interface

A metal/semiconductor contact is usually either an Ohmic contact or a Schottky contact formed permanently during device fabrication. An Ohmic contact is characterized by a linear current-

voltage (I-V) curve in both forward and reverse bias, and there is no electric field drop at the metal/semiconductor interface during charge injection. A Schottky contact, on the other hand, is distinguished by its rectifying property where the current is limited by the amount of charges injected from the electrode to the semiconductor instead of the carrier mobility.[136] In order to study the electrical contact formed instantaneously between the silver nanowires and the perovskite semiconductor interface, a Ag/$MAPbBr_3$:PEO/Ag structure was fabricated to bring the silver metal and the $MAPbBr_3$:PEO film into permanent contact. The detail architecture of the Ag/PEO:Pero/Ag device is illustrated in Figure 4.11. The PEO:Pero solution was first spin-coated onto a cleaned glass substrate, then it was thermal annealed at 60° C for 3 minutes. Next, Ag was thermally evaporated at a pressure < 10^{-6} mbar with thickness of 100 nm with shadow mask. The distance between the two Ag electrodes is 50 μm.

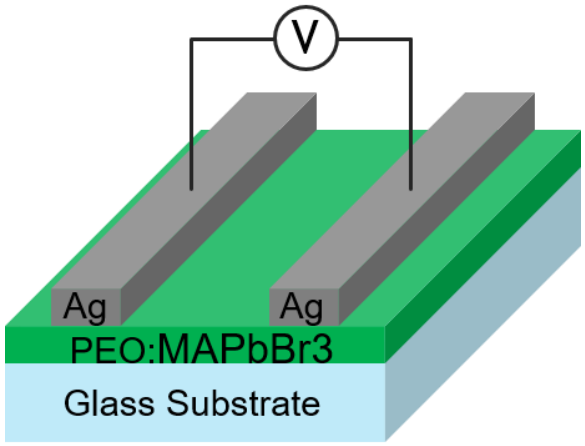

Figure 4.11: Illustration of Ag/$MAPbBr_3$:PEO/Ag device.

The I-V characteristic of the Ag/$MAPbBr_3$:PEO/Ag thin film was measured by a conventional two-probe method and is displayed in Figure 4.12a. Here, the contact between silver and perovskite semiconductor was shown to be of the Schottky type. Figure 4.12b shows the energy band diagram of the Ag/pero/Ag system, and Figure 4.12c illustrates the electrical circuit of the back-to-back diodes.

The I-V curve shown in Figure 4.12a has previously been observed by Chiquito et al. and portrayed as a back-to-back Schottky barrier based on the usual thermionic emission theory for metal/semiconductor/metal devices.[137] The formation of the Schottky barrier at each interface was due to the difference in the work functions of silver and perovskite as shown in Figure 4.12b.[138][139] Here, the energy barrier between the LUMO (or bottom of conduction band) of perovskite and silver was 0.54eV. Unlike the conventional Schottky barrier, this back-to-back Schottky diode exhibited a symmetric IV response, and electron injection was suppressed by the Schottky barrier under this configuration.[140][141]

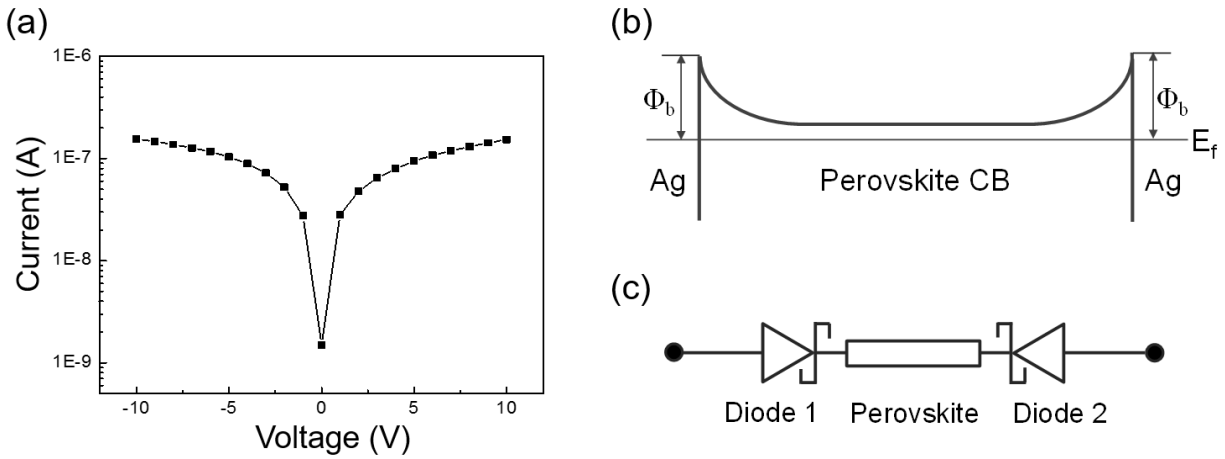

Figure 4.12: (a) Semi-log graph for I-V characteristic measured on an Ag/$MAPbBr_3$:PEO/Ag device. (b) Energy band diagram of the Ag/$MAPbBr_3$:PEO/Ag device (only the conduction band

is shown). Φ_b is the Schottky barrier height between silver and $MAPbBr_3$. (c) Illustration of a back-to-back contact as two diodes in the blocking direction.

4.3.8 Mechanical deformation of AgNW-PU Transparent Electrode

In order to create an instantaneous Schottky contact between the electrode and the pero composite layer, the pressure loading has to be large enough to deform the AgNW-PU electrode to touch the $MAPbBr_3$:PEO film below it. When a load with a small contact area was applied onto the AgNW-PU electrode, the AgNW-PU electrode deformed into a square-base pyramid shape (Figure 4.13). Here, the elastic modulus of the AgNW-PU transparent electrode was calculated to be 31 MPa from the tensile stress-strain curve (Figure 4.2) measured under room temperature at a stretching rate of 1 mm s^{-1}. The deformation of the composite electrode was biaxial. The mechanical modeling of this biaxial deformation is described in the following section. Given a 100 μm air gap, the minimum pressure to create a Schottky contact between the electrode and the pero composite layer is 0.55 MPa. The minimum pressure required to create an instantaneous Schottky contact at different air gap heights are calculated. (Figure 4.14). It was also determined that once the minimum pressure was reached to form the electrical contact, the performance of the pero LETD was insensitive to further pressure loading.

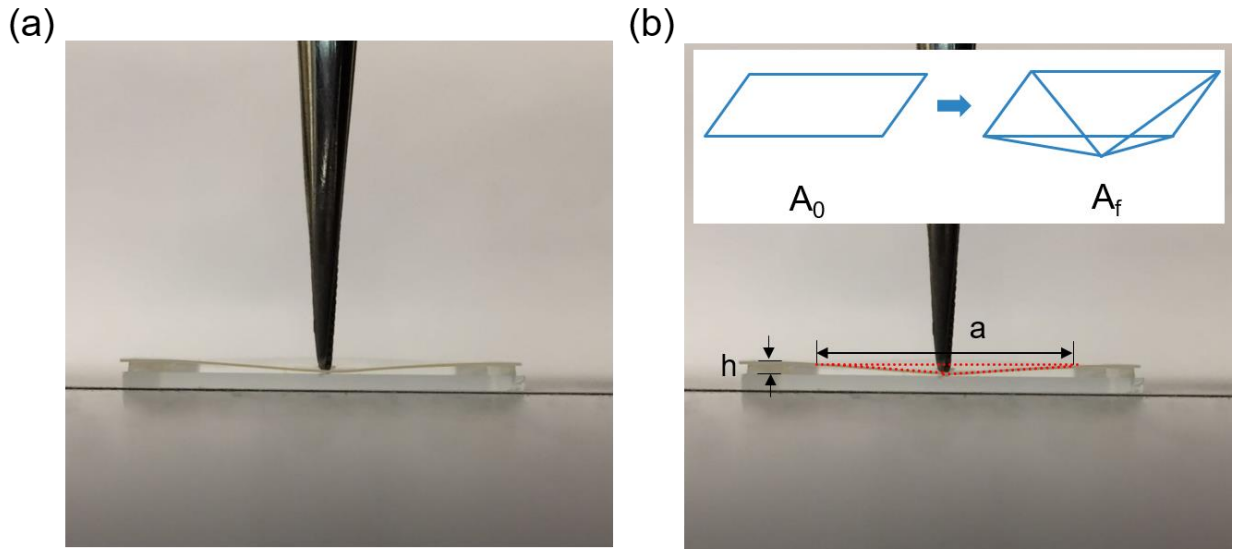

Figure 4.13: Deformation of AgNW-PU transparent electrode created by a tweezer's tip pointing down onto the LETD device. A deformation shape of a square-base pyramid is observed here. Stress Diagram is shown in the Inset Figure.

Mechanical Analysis of AgNW-PU Deformation.

Figure 4.13 shows that when pressure was exerted onto a small region of the AgNW-PU transparent electrode, the electrode deformed into a trapezoid shape when a stable contact was made with the pero film below. From Figure 4.13, the point contact area was relatively small compared to the AgNW-PU film; the deformation created by this point contact was treated as a square-based pyramid shape for ease of calculation. This allows the calculation of the total area expansion of the AgNW-PU electrode when pressure was applied. The area expansion and the measured elastic modulus of the electrode then allowed the calculation for the required pressure to create a stable Schottky contact.

I. Total area expansion of the AgNW-PU transparent electrode. The area strain of AgNW-PU substrate can be calculated by following Equation (4.1):

$$Area\ Strain\ (\%) = \%\ of\ area\ change = \frac{Af - A_0}{A_0} \times 100\% \qquad (4.1)$$

where A_0 is the original area of the AgNW-PU film before deformation, and A_f is the total area of the film after deformation. The AgNW-PU film was in a square shape with its edge (a) being 15mm. A_0 is the area of the square film and was calculated to be 225 mm^2. Assuming the air gap height (h) is 0.1 mm, A_f can be computed by finding the total surface area of the 4 triangles of the square-based pyramid, and it was calculated to be 225.02 mm^2. The area strain was then calculated as 0.89%. In this calculation, we assumed that the thickness of the electrode stayed constant during the deformation.

II. Biaxial Elastic Modulus. In order to calculate biaxial stress, the biaxial elastic modulus must be determined. Since the film thickness was small compared to the total LETD thickness, and the lateral dimensions of the AgNW-PU were much greater than the film thickness, the biaxial elastic modulus (M) can be correlated to the Young's modulus (E) by [142]

$$M = \frac{E}{1-\upsilon} \qquad (4.2)$$

where υ is the poisson ratio. Young's modulus of the electrode was measured to be 31 MPa by DMA, and the poisson ratio for elastomer was ~0.5. Thus, the biaxial elastic modulus was calculated to be 62 MPa. The elastic modulus was calculated from the tensile stress-strain curve in Figure S1. From the stress-strain curve, it can be observed that within 8% strain, stress increased linearly with strain. All the calculated strains were within 8%; thus, the calculated E can be used in the calculation here.

III. Calculation of Biaxial Stress. By knowing the biaxial strain and biaxial elastic modulus, biaxial stress can be calculated according to Equation (4.3).

$$\sigma = M \cdot \varepsilon \qquad (4.3)$$

where σ is the biaxial stress; this is also the minimum pressure required to create a Schottky contact for the pero LETD. The minimum required pressure was calculated to be 551 Pa. In Figure 4.14, the minimum required pressure for various air gap heights was also calculated and shown in the plot.

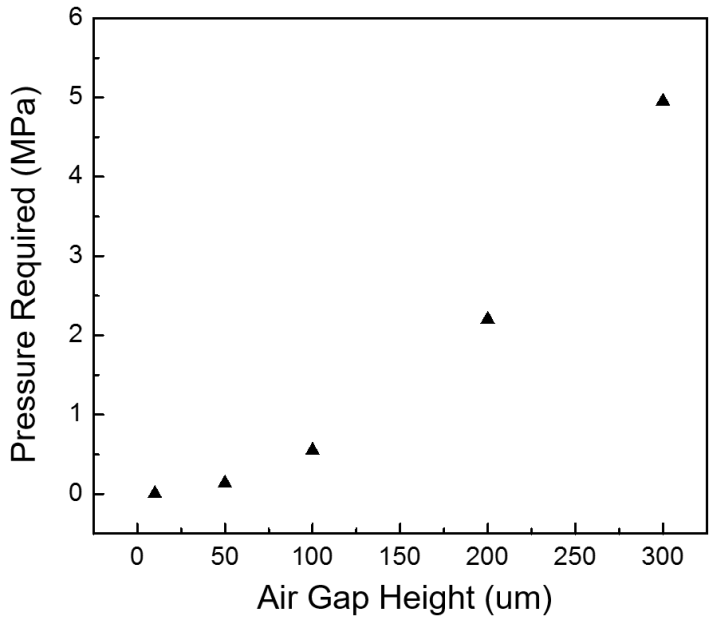

Figure 4.14: Calculated pressure required to make a stable contact based on different air gap heights.

4.3.9 Instantaneous Pattern Recognition

To demonstrate the sensitivity and precision of the pero LETD, a series of patterns were introduced to the device. The interactive LETD was able to visually display a high-resolution image of pressure distribution as seen in Figure 4.15. Letter stamps in the form of U, C, L, and A were used to apply pressure patterns onto the LETD while the LETD was under a constant supply of 4 V. When pressure was exerted, the imprints of the stamps pushed down on the AgNW-PU composite electrode surface, which encountered the pero emissive layer and emitted green light corresponding to the pattern of the stamps. It was important for the stamp surface to be smooth and parallel to the LETD during the stamping action in order to achieve sharp and uniform lighting images as shown in Figure 4.15.

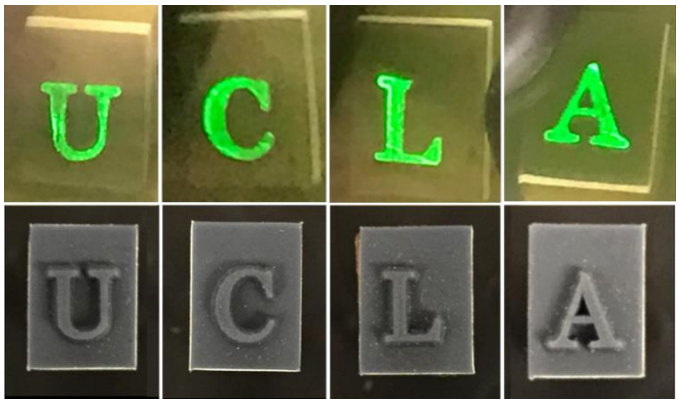

Figure 4.15: Demonstration of an LETD by loading UCLA letter stamps against the PU surface of the LETD. The top row shows the electroluminescence images of the stamps. The bottom rows are the stamps used.

LETDs were also fabricated in which the AgNW network in the composite electrode was patterned into the numbers 1 through 4 (Figure 4.16). The electrode patterning was done by spray coating the AgNW solution over a contact mask. The bottom layer of the LETD was prepared the same way as previously described. When a pressure was uniformly applied onto a specific location, the number pattern would light up accordingly (Figure 4.16).

When ITO/PET was used as the substrate, the LETD became flexible. Figure 4.17 shows a flexible LETD bent to a 1 inch-diameter and attached to a small vial. When a pressure pattern was applied with a letter stamp "T", the letter T emanated green light. It is worth noting that in this LETD, the composite pero film was under tension, but this had no effect on its electroluminescence. This further confirmed that the PEO matrix held the $MAPbBr_3$ grains cohesively together and that there was no shifting of pero grains due to bending.

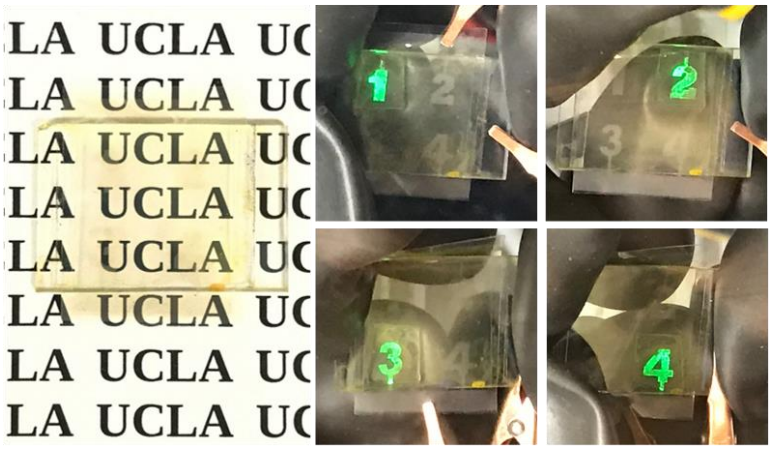

Figure 4.16: A LETD with AgNW electrode patterned into numbers 1 through 4. When pressure is applied on the specific locations, the 1, 2, 3, or 4 shape lights up accordingly.

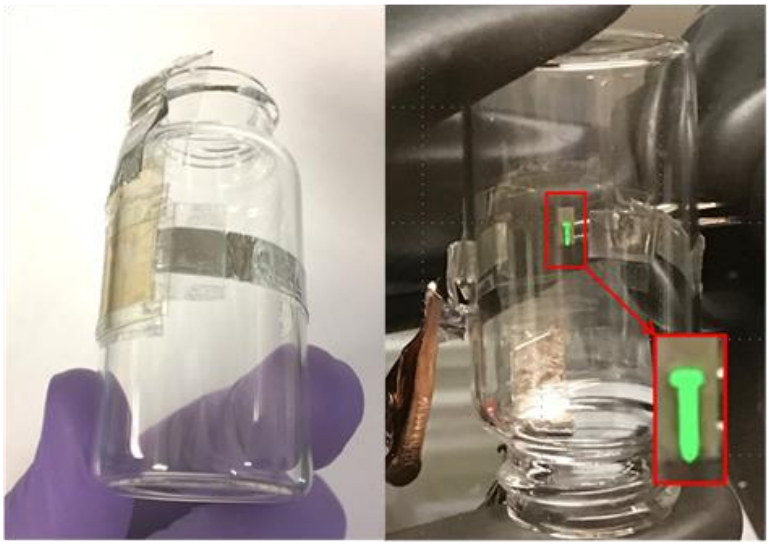

Figure 4.17: A transparent flexible LETD wrapped to a 1 inch-diameter vial (Left) and glowing in the form of letter ‘T’ when stamped (Right).

4.3.10 Pixelated LETD

An array of a pixelated LETD was fabricated by patterning the spacer between the composite electrode and the $MAPbBr_3$:PEO layer. The spacer was patterned into a grid with 1 x 1 mm^2 pitch, 0.2 mm spacer line width and 0.04 mm thickness.

A rigid system with an array of 10 x 10 pixels was assembled as shown in Figure 4.18a. Figure 4.18b demonstrates a 16 x 16 array of a flexible pero LETD based on an ITO/PET substrate attached to a 1 inch-diameter vial. The area pressed by a fingertip produced green light emission showing the individual pixels turned on. The $MAPbBr_3$:PEO layer was under tension in this LETD device and the electroluminescence remained stable. This pixelated LETD could be bent to a 6

mm diameter (Figure 4.18b). The pixel size could be made to as small as 200 μm limited by the resolution of the laser cutter used to pattern the spacer.

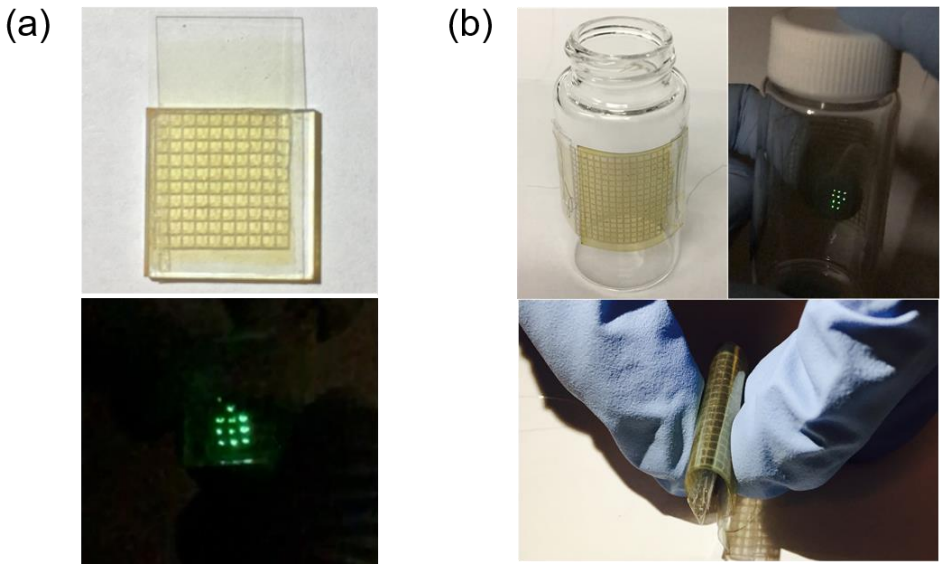

Figure 4.18: Optical photographs of (a) a rigid 10 x 10 LETD array and (b) a flexible 16 x 16 LETD array (total area: 1 x 1 inch^2), localized light emission upon finger pressing, and the array bent to 6 mm diameter. The emissive area pixel size is 0.8 mm x 0.8 mm.

4.4 Conclusion

In summary, we have successfully demonstrated the first LETD based on the integration of a perovskite-polymer composite emissive layer and a AgNW-PU composite electrode touch interface. The LETD provides an easily viewable light emission to show the pattern and motion of applied pressure. The LETD is made possible due to the instantaneous formation of a Schottky

contact between the cathode AgNW and the perovskite emissive layer when a force is exerted to bring the metal and semiconductor in contact. The electrical contact is transiently formed, but stable when the pressure is kept on, and can be formed repeatedly and reversibly. In addition, the PEO additive forms a protective matrix around the perovskite nanocrystals, which holds the $MAPbBr_3$ grains cohesively together and enables stable electroluminescence under bending. The pero touch response device may find applications in robot-object interaction, fingerprint identification, motion detection, interactive wall paper, and interactive clothing.

Chapter 5 . Stretchable Perovskite Light Emitting Diodes

5.1 Introduction

The rise of flexible electronics has brought along what is expected to be the next generation in electronics application, the stretchable electronic. With the ability to mechanically expand, stretchable displays can be used in foldable smart phones, wearable clothing, collapsible lamps, and even wearable healthcare electronics.[143–149] Due to their ability to withstand high mechanical deformation, stretchable displays can be applied on any irregular surface. In addition, their unique characteristic of being able to collapse increases the portability of large displays.

The first stretchable LED was fabricated in 2009 by mounting an array of microscale inorganic LEDs onto a rubber substrate.[150] During that same year, similar work was done with the integration of rigid OLEDs onto a CNT-rubber substrate[151]. Both devices demonstrated high stretchability and high efficiency under strain. Other methods such as employing ultrathin substrates or corrugated substrates to make LEDs have been reported. The stretchable devices were able to reversibly compress and extend back to their original lengths.[152][153] Another mechanism was achieved by intrinsically stretchable LEDs, where all the materials used in the device were stretchable. Yu et al. first reported intrinsically stretchable blue PLEDs, which could be stretched up to 45%.[154] Liang et al. also reported intrinsically stretchable polymer light-emitting electrochemical cells (PLECs), which could be stretched up to 120% and remained functional after 1000 stretch-release cycles.[47] Unfortunately, both of these devices have high turn-on voltage, and the highest luminance was reached at 12 V for the blue PLED and 21 V for the PLEC. Another

drawback of both intrinsically stretchable lighting devices is that they require high power consumption.

Organometal halide perovskite has recently attracted great attention in optoelectronics due to its properties of high color purity, high absorption coefficient, tunable bandgaps, and high ambipolar charge mobility[10,24,124,155]. The first perovskite light-emitting diode (PeLED) was reported by Tan et al.[127], and within only two years, its efficiency has approached that of an OLED device at 8.53% EQE[124]. In addition, perovskite can be solution processed and is cost effective. All these characteristics make perovskite an appealing candidate for display applications. The first stretchable PeLED was reported by Bade et al. earlier in 2017.[155] This PeLED was fabricated with perovskite-PEO composite emitter and a PEDOT:PSS-PEO composite electrode on a PDMS substrate; the device was able to be stretched up to 40%. Unfortunately, PEO is known to have a small elastic range (<5%), which is due to its high crystallinity (>60 %); as a result, the perovskite-PEO emissive layer has low stretchability and poor stability under strain. Moreover, an organic semiconductor intrinsically has lower conductivity than metal, therefore, the conductivity of the anode electrode can be improved.

Inspired by Bade et al.'s work, we report a stretchable perovskite light-emitting diode using an organometal perovskite blended with polyethylene glycol diacrylate (PEG) and silicon acrylate (PDMS) as the stretchable light emitting film. PEG is chosen here because it assists in spreading out perovskite grains and hinders the diffusivity of perovskite precursors at the solvent drying stage, which results in a smooth film where the perovskite grains eventually distribute over the entire film. In addition, the PDMS matrix serves as the elastic connector and held the film together, while providing stretchability to the pero emissive film. The stretchable PeLED has the device structure of AgNW-PU/PEO-modified PEDOT:PSS/PEG:PDMS:$MAPbBr_3$/EGaIn, where AgNW

is an anode electrode, PEO-modified PEDOT:PSS is the hole injection layer, PEO:PDMS:$MAPbBr_3$ (a composite of methylammonium lead bromide, polyethylene oxide, and silicon acrylate) is the emissive layer, and EInGa (eutectic indium-gallium metal) is the cathode. The composite electrode (anode) is comprised of a thin AgNW network embedded in the surface of the rubbery poly(urethane acrylate) (PU) matrix to provide an ultra-smooth, highly transparent, highly conductive, and highly stretchable electrode substrate. The stretchable PeLED can be turned on at 3.4 V and reaches the maximum luminance at 207 cd/m^2 at 8V.

5.2 Experimental Section

5.2.1 Materials

N,N-dimethylformamide (DMF) (anhydrous, 99.8%), 2,2-dimethoxy-2-phenylacetophenone (photoinitiator), and poly(ethylene oxide) (average Mw≈5,000,000), poly(ethylene oxide) (average Mw≈5,000,000), poly(ethylene glycol) diacrylate (average Mw≈20,000) and indium-gallium eutectic (Ga-In) (99.99%) were purchased from Sigma-Aldrich. Lead(II) bromide (99.999%) was purchased from Alfa Aesar. The methylammonium bromide was purchased from "1-Material Inc." Low conductivity poly(3,4-ethylenedioxythiophene): poly(styrenesulfonate) (PEDOT:PSS) (CleviosTM P VP AI 4083) was purchased from H.C. Starck Inc. Silver nanowires were from Zhejiang Kechuang Advanced Materials Co. Siliconized urethane acrylate oligomer (UA), an ethoxylated bisphenol A dimethacrylate (EBA), and an aliphatic silicon acrylate (PDMS) were supplied by Sartomer. All materials were used as received.

5.2.2 Fabrication of AgNW-PU Composite Electrode

AgNWs were first uniformly dispersed in an organic solution at 0.5 wt%. A Meyor rod was used to coat thin layers of AgNW on a cleansed releasing substrate until a uniform film of 20 Ω/□ sheet resistance was achieved. The AgNW film was annealed at 165°C for 8 minutes before use. A co-monomer precursor consisting of UA, EBA, and PI in the ratio of 100:20:1 was coated on top of the AgNW film. Next, the sample was set under a UV lamp and cured at 2.5 W/cm^2 intensity. Finally, the cured AgNW-PU composite electrode was peeled off from the releasing substrate.

5.2.3 Fabrication of Stretchable Perovskite LED

The AgNW-PU composite electrode was cleansed with IPA and distilled (DI) water before use. PEO was dissolved in DMF to achieve a concentration of 10 mg/mL. After the PEO precursor was well mixed, the PEDOT:PSS solution was mixed with the PEO precursor at a desired ratio and stir-mixed overnight. The prepared composite PEDOT:PSS solution was first spin-coated onto the AgNW-PU electrode at 4000 rpm and annealed at 120°C for 20 minutes on a hotplate. The Br-pero precursor solution was prepared by dissolving $PbBr_2$ and MABr in a 1:1.5 molar ratio in DMF to achieve a final concentration of 500 mg/mL. PDMS was dissolved in DMF to obtain a final concentration of 10 mg/mL. The Br-pero precursor, PEG precursor, and PDMS precursor were then mixed at an ideal ratio. All solutions were stir-mixed under 60°C overnight before use. This composite pero precursor was spin-coated on top of the PEDOT:PSS-PEO film at 2000 rpm. Thermal annealing at 120°C for 3 minutes was followed immediately. Ga-In Eutectic mental was dropped onto the surface of the composite pero film, serving as the cathode electrode.

5.2.4 Characterization of PEG:PDMS:$MAPbBr_3$ Film

SEM images were taken by a JEOL JSM-6710F scanning electron microscope. Atomic force microscope images were captured by a Bruker Dimension Fastscan scanning probe microscope. Photoluminescence spectra were carried out by using a Photon Technology International Spectrophotometer. Absorbance spectra were collected by a Shimadzu UV-1700 spectrophotometer. The stretchable pero LED was driven and the electrical readings were recorded by a Keithley 2400 and Keithley 2000 Source Meter unit. The device performance was tested inside a nitrogen filled glovebox with oxygen and moisture levels lower than 0.1 ppm. The electroluminescence spectrums were carried out by using a photoresearch PR655. All the characterization tests were performed at room temperature.

5.3 Results and Discussion

5.3.1 Stretchable PeLED Device Fabrication.

The stretchable PeLED was fabricated according to the schematic in Figure 5.1. The AgNW-PU transparent composite electrode was first prepared via a transferring process that inlaid the nanowires in the surface layer of PU film.[47] The AgNWs used in this work have a length to diameter aspect ratio of ~500, and the PU matrix is a copolymer of a siliconized urethane acrylate oligomer (UA) and an ethoxylated bisphenol A dimethacrylate (EBA). Both UA and EBA have high transparency; UA is chosen here to provide the composite electrode with excellent stretchability, while EBA provides a good bonding force between AgNWs and UA. The fabricated composite electrode has low sheet resistance (~10 Ω/□) at high transmittance (~87%). The

composite electrode's elongation at break is around 120%, and the Young's modulus is 31MPa. The strong bond between AgNWs and the PU matrix was established by the Scotch tape test; the sheet resistance of the composite electrode remained the same after taping and peeling off the adhesive from the composite electrode for over 100 cycles.

Based on the stretchable composite electrode, perovskite LED was fabricated on top of it by an all-solution processing procedure. The PEDOT:PSS solution was first mixed with PEO at a weight ratio of 3 to 1. The homogeneous PEDOT:PSS-PEO solution was spin-coated on top of the AgNW-PU composite electrode followed by thermal annealing at 130°C for 20 minutes. A precursor containing PDMS, PEO, and $MAPbBr_3$ (0.3:0.3:1 weight ratio) was then spin-coated onto the PEDOT:PSS-PEO film. The film was subsequently cured at 90°C for 5 minutes. EGaIn was applied on top as the cathode for testing the device performance.

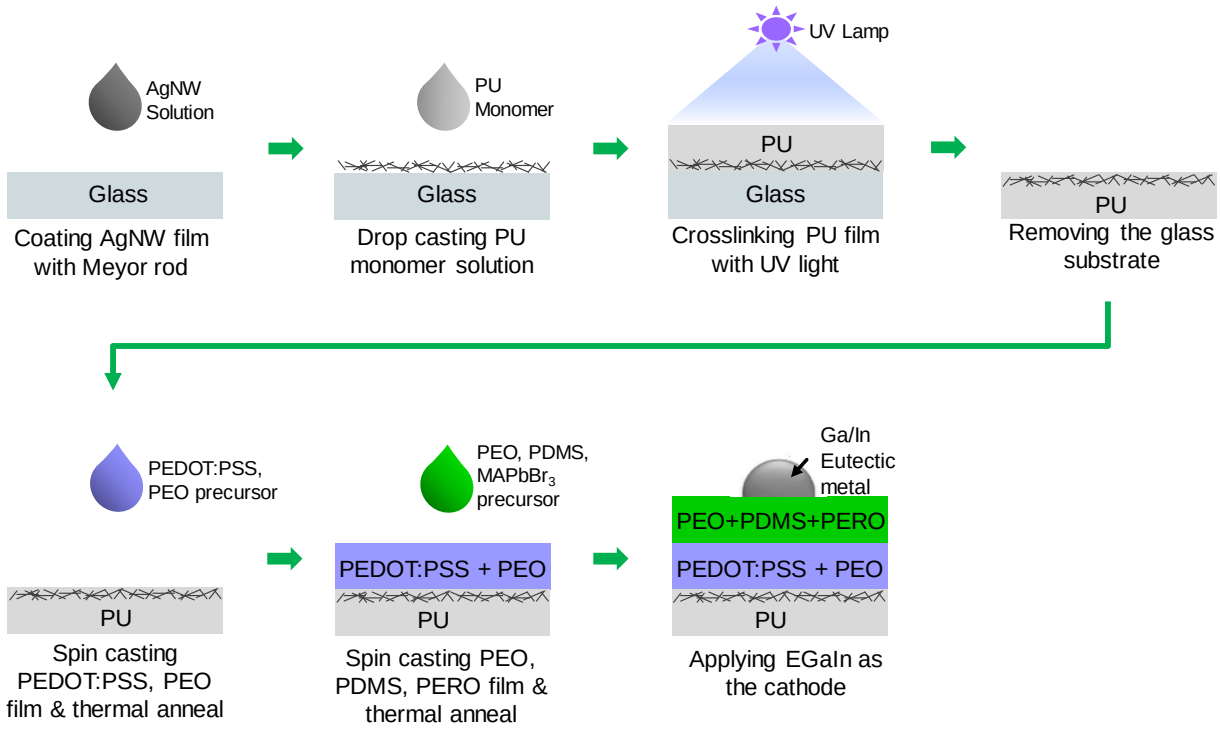

Figure 5.1: Illustration of the stretchable PeLED fabrication process.

5.3.2 PEG:PDMS:$MAPbBr_3$ Stretchable Film

The stretchable emissive layer consists of PEG, PDMS, and MAPbBr3 as illustrated in Figure 5.2. In the stretchable composite film, the PEG matrix helps to separate individual pero grains apart from one another, which results in a uniformly spread pero grain film. The PDMS matrix, on the other hand, serves as the elastic connector, providing stretchabiltiy to the pero composite film and holds the rigid $MAPbBr_3$ grains together. The acrylate groups appear in both PEG and PDMS polymer, forming crosslink networks and providing a mechanically stable film.

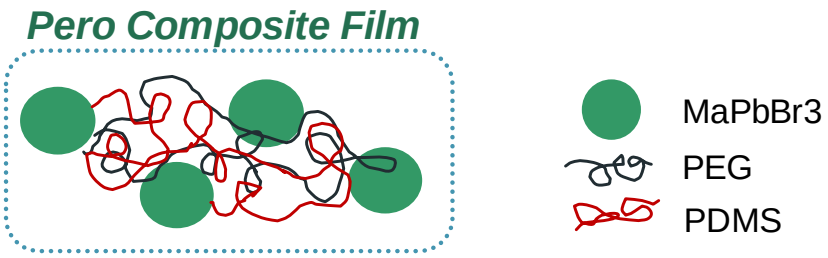

Figure 5.2: Schematic illustration of the stretchable pero composite film.

The PEG:PDMS:$MAPbBr_3$ composite thin films were achieved through a one-step spin-coating process from a precursor containing PEG, PDMS, MAPb, and $PbBr_2$ dissolved in DMF. $MAPbBr_3$ was used here as the green emitter, and the weight ratio of individual components were studied in Figure 5.3. The weight ratio of PEG and PDMS over the total weight of pero in the precursor is labeled. For example, the optimal ratio of 0.3:0.3:1represents that the weight of PEG and PDMS respectively equal 30% of the pero's weight in the precursor. For easy reference, the following labels will be used: X represents PEG, Y represents PDMS, and Z represents $MAPbBr_3$ in an

X:Y:Z configuration. The scanning electron microscope images of the morphology evolution of the stretchable perovskite emitting film is demonstrated in Figure 5.3. Figure 5.3a-c show the resulting film morphology from three precursors at 0.1:0.1:1, 0.3:1:1, and 0.5:0.5:1 ratios. The grain size of the perovskite reaches its minimum at a 0.3:0.3:1 ratio. The PL spectrum of the resulting films from three precursors are also shown in Figure 5.4. The trend observed was that the smaller the grain size, the larger the EL intensity. At a 0.3:0.3:1 ratio, the stretchable composite pero film had the minimum grain size and highest PL intensity. Figure 5.3d shows the film morphology of the film casted from the precursor containing only PDMS and $MAPbBr_3$. The image shows that no pero grains nucleated out from the 0:0.3:1 precursor; this was further confirmed by observing no PL from the film. The precursor with only PEG and $MAPbBr_3$ in a 0.3:0:1 precursor produced small pero grains as shown in Figure 5.3e. The morphology of the copolymer of PEG and PDMS film is also studied in Figure 5.3f.

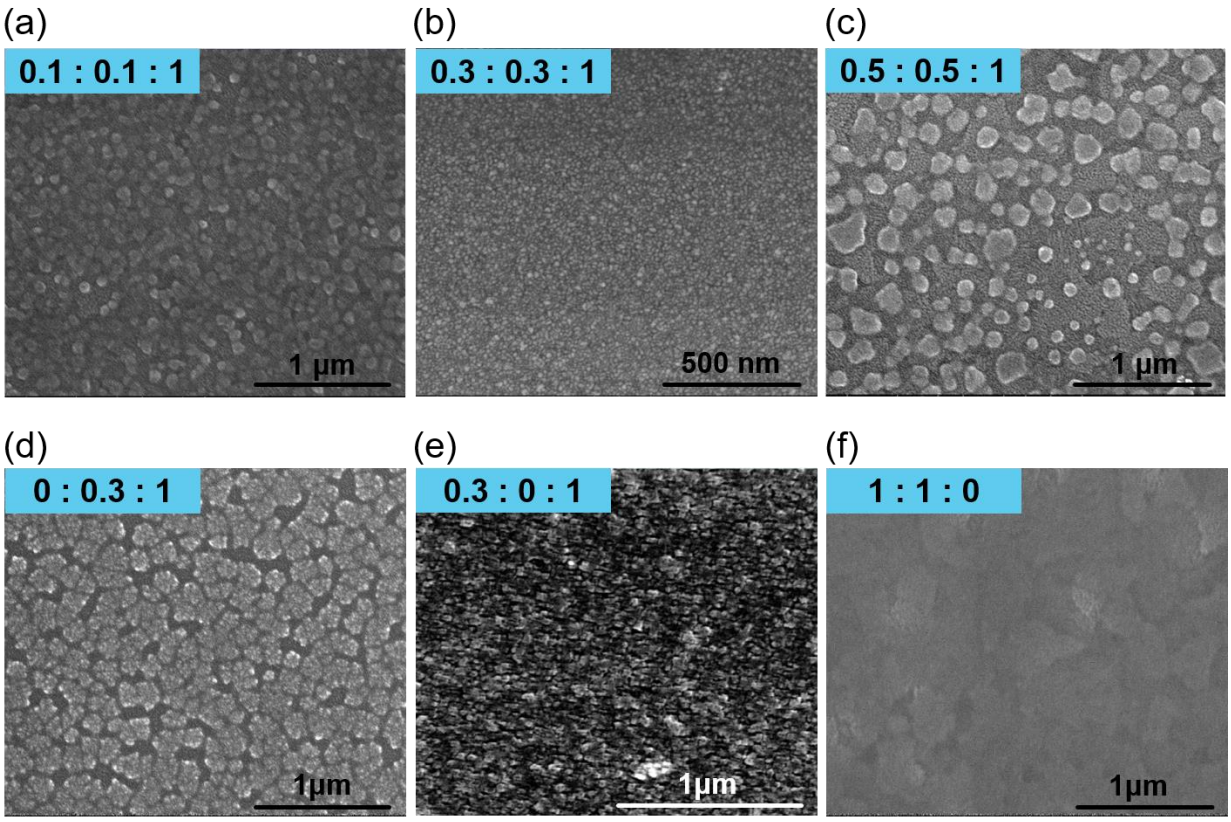

Figure 5.3: SEM images of the stretchable perovskite composite films with PEG:PDMS:MAPbBr3 (X:Y:Z) ratio a) 0.1:0.1:1, (b) 0.3:0.3:1, (c) 0.5:0.5:1, (d) 0:0.3:1, (e) 0.3:0:1, and (f) 1:1:0. The composite films were sitting on top of a glass substrate.

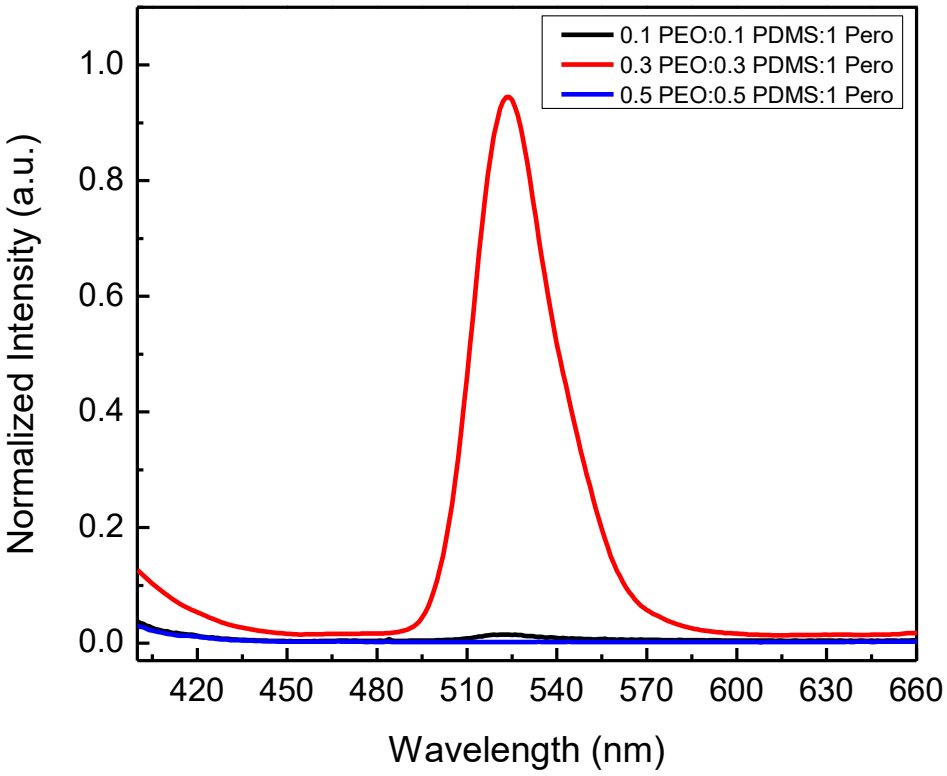

Figure 5.4: PL spectrum of the stretchable composite films with PEG:PDMS:$MAPbBr_3$ ratios of 0.1:0.1:1 (black), 0.3:0.3:1 (red), and 0.5:0.5:1 (blue).

The optical properties of the stretchable perovskite composite film were investigated and the absorption and PL spectra of the film are both shown in Figure 5.5. The composite pero film coated on glass exhibited a bright green light at 375 nm excitation wavelength with a PL peak located at 524 nm. The onset wavelength was approximately 520 nm, according to the absorption spectrum, which corresponds to a 2.4 eV direct bandgap of the Br-pero.

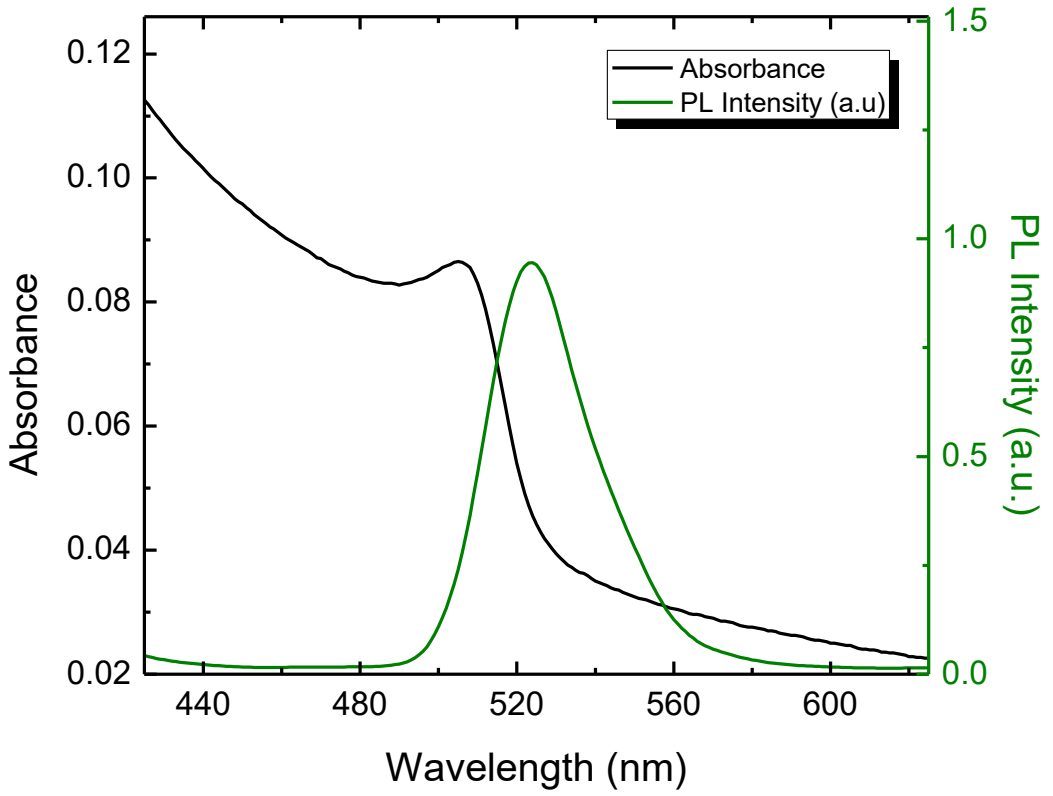

Figure 5.5: Absorption spectrum (black) and PL spectrum (green) of the PEG:PDMS:$MAPbBr_3$ composite thin film at 0.3:0.3:1 ratio.

Unlike a perovskite only film, the composite perovskite film exhibited an ultra-smooth surface due to the addition of the copolymer matrix. Atomic force microscopy was used here to study the surface of the optimized stretchable composite film (0.3:0.3:1), and the average surface roughness was found to be lower than 2 for a 90 nm film. The AFM image of the stretchable pero composite film is shown in Figure 5.6.

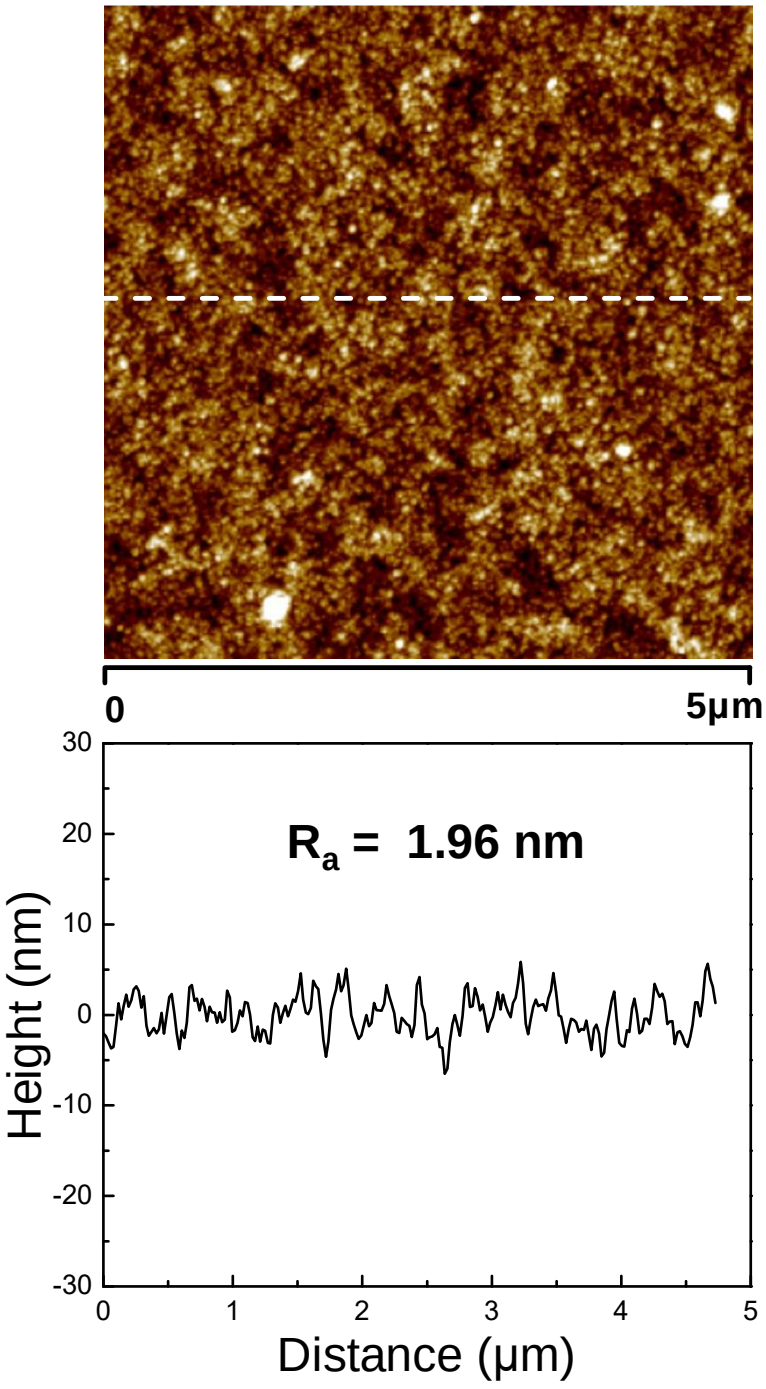

Figure 5.6: AFM image of a PEG:PDMS:$MAPbBr_3$ (0.3:0.3:1) film on glass.

The photographs of the PEG:PDMS:$MAPbBr_3$ film on PU under 365 nm UV irradiation can be found in Figure 5.7. The stretchable pero composite film was stretched from 0% to 50%, and a uniform green emission was found even when the film was stretched to 50%. The optical properties of the stretchable film were studied by using PL. The PL intensity of the stretchable composite film under 0% and 50% were both collected by PR655 and the results are shown in Figure 5.8. The intensity peaked at 532 nm for both unaltered and stretched films. Compared with the unaltered film, a decrease in PL intensity was observed when the composite film was stretched to 50%. This can be explained by the decrease in perovskite grain density when the film was stretched, which resulted in lower PL intensity. The scanning electron microscopy in Figure 5.9 confirms the decrease in the pero grain density before and after stretching to 50%. The PEG:PDMS:$MAPbBr_3$ composite film was spin-coated onto PEDOT:PSS-PEO/AgNW-PU, and the surface morphology of the unaltered film is shown in Figure 5.9a. A dense perovskite film that was smaller than 100nm was spread out across the film in the unaltered film. After stretching to 50%, the distance between the pero grains increased, resulting in the total number of pero grains within the same area of the film to decrease.

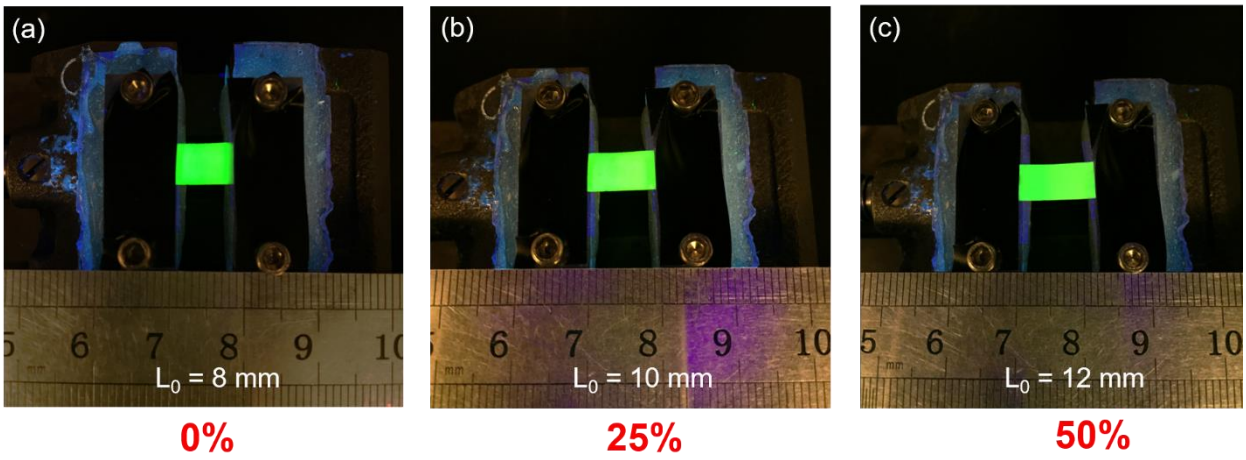

Figure 5.7: Photographs of the PEG:PDMS:MAPbBr3 composite film on the PU substrate under 365 nm UV irradiation when stretched to (a) 0%, (b) 25%, and (c) 50%.

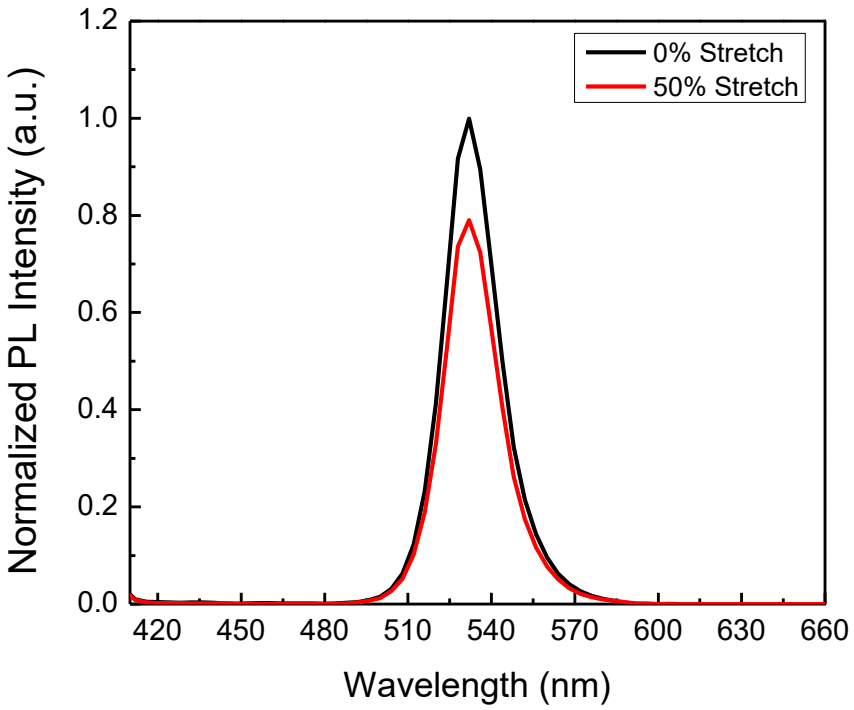

Figure 5.8: PL spectra of the PEG:PDMS:$MAPbBr_3$ stretchable composite film before (black) and after (red) 50% strain.

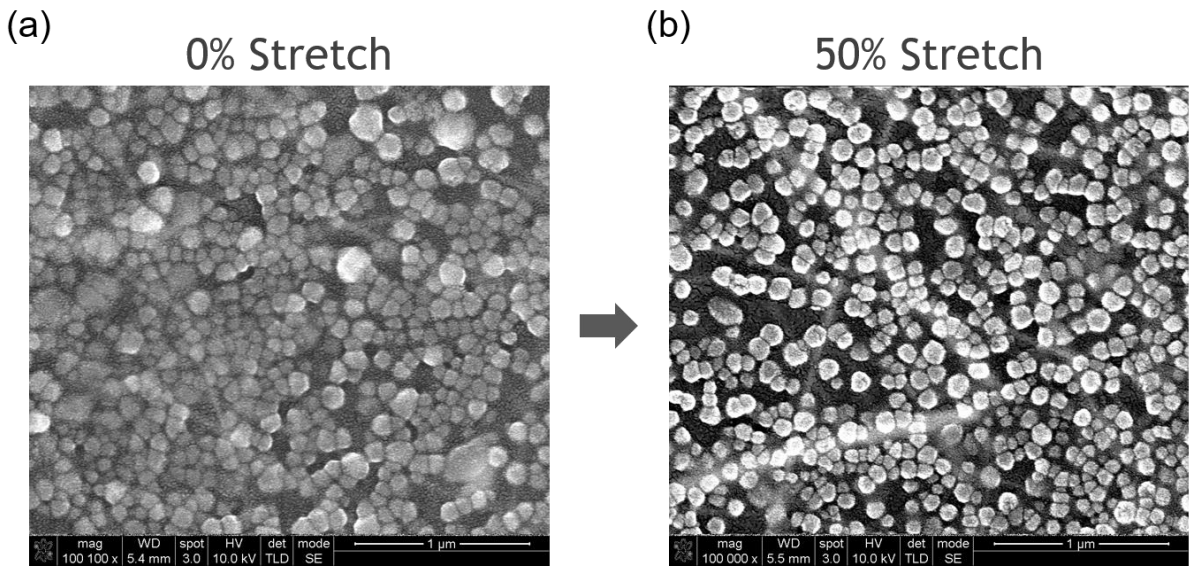

Figure 5.9: SEM images of PEG:PDMS:$MAPbBr_3$ stretchable composite film on PU under (a) 0% and (b) 50% strain.

5.3.3 Stretchable Pero LED Device Performance

After optimizing the PEG:PDMS:$MAPbBr_3$ composite film, the stretchable LED device was constructed on top of the AgNW-PU stretchable substrate. PEO was added into PEDOT:PSS to form a homogenous solution to create a hydrophilic surface and enhance the nucleation rate for the perovskite composite precursor. It was experimentally found that when the PEDOT:PSS and PEO weight ratio was 3:1, the composite pero film from the precursor resulted in a uniform film. The stretchable PeLED has a device structure as follows: AgNW-PU/PEDOT:PSS-PEO composite/PEG:PDMS:$MAPbBr_3$ composite/EGaIn. The anode electrode here is AgNW, and the cathode electrode is EGaIn. The active area here is defined by the size of the EGaIn electrode, and it was ~2 mm in diameter. The luminance (L)- voltage (V)- current density (J) characteristics of

the green stretchable PeLED before stretching are shown in Figure 5.10. The stretchable PeLED turned on at 3.4 V (defined at 10 cd/m^2), reaching over 200 cd/m2 at 8 V. The stretchable PeLED was clamped on both sides and subjected to uniform strains on both sides. EGaIn was first applied on top of the 0% stretch device and stayed on the composite pero film during the stretching. The photographs of a working stretchable PeLED are shown in Figure 5.11. It can be seen that the PeLED remains functional from 0% to 60% stretch with decreasing luminance. This is consistent with the PL results where the decrease in luminance was due to the decrease of pero grain density in the same given lighting area. Furthermore, the decrease in luminance under stretching condition is also result from an increase in resistance of the AgNW-PU electrode when it's under stretched.

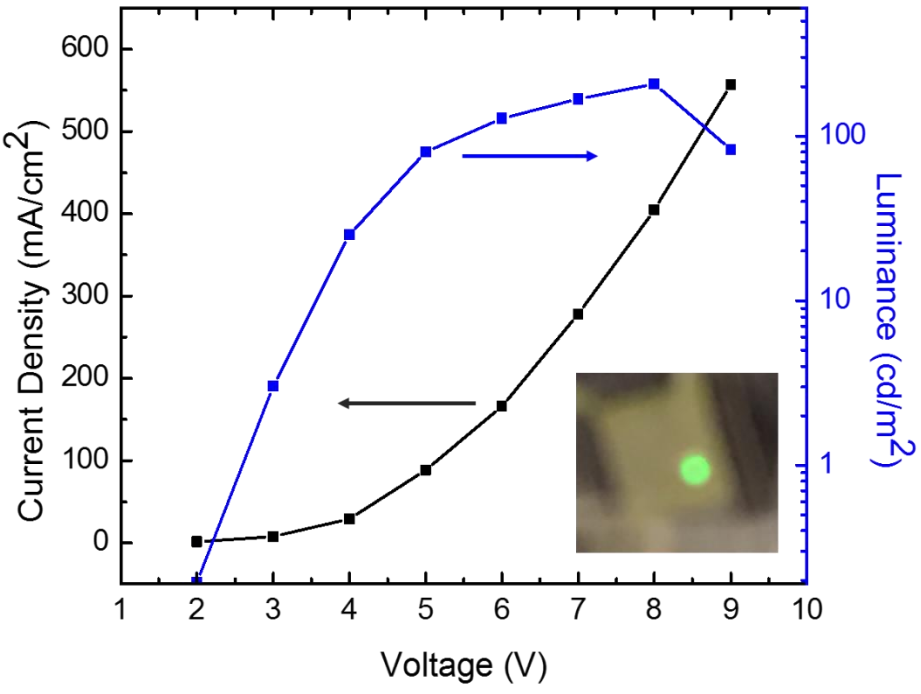

Figure 5.10: L-V-J characteristics of the stretchable PeLEDbefore stretching. (inside) A photograph of the green emission of the PeLED under 4V.

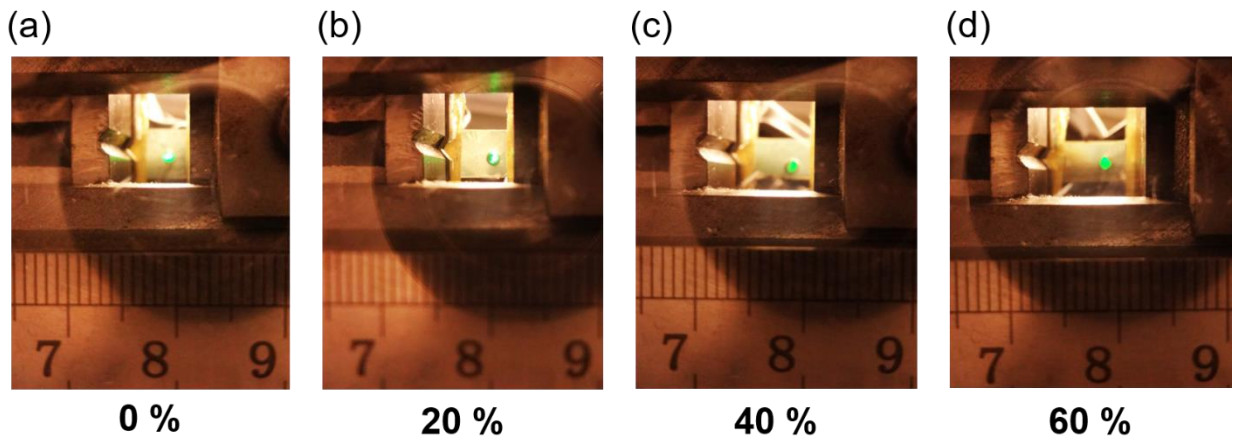

Figure 5.11: Stretchable PeLED under 5 V bias when stretched under (a) 0%, (b) 20%, (c) 40%, and (d) 60%.

5.4 Conclusion and Future Work

We have demonstrated that a functional stretchable PeLED can be fabricated using an all-solution-based process. The stretchable PeLED includes a stretchable anode electrode (AgNW-PU), a PEDOT:PSS-PEO composite hole transporting layer, and a stretchable composite emitting layer (PEG:PDMS:$MAPbBr_3$). The composite anode electrode provides high conductivity, high transmittance, and high mechanical stability. The PEG:PDMS:$MAPbBr_3$ composite layer is intrinsically stretchable where PEG serves as the dispersant for pero grains, PDMS serves as the elastic connectors for the film, and PEG:PDMS:$MAPbBr_3$ emits green light. The device remains functional when stretched up to 60%. This work shows the potential of PeLED in stretchable lighting applications.

However, to bring the stretchable PeLED to commercial products, the cathode electrode needs to be made with stretchable materials and must be easy to handle. The possible solutions are laminating a AgNW-PU top electrode or spray coating AgNW electrode on top of the PEG:PDMS:$MAPbBr_3$ composite film as the cathode. With both methods, a fully transparent stretchable PeLED would be possible. Afterwards, a cycling test to show reversible lighting under strain will need to be performed; this will be possible after permanently attaching the top electrode to the PEG:PDMS:$MAPbBr_3$ composite film.

Chapter 6 . Conclusion and Future Remarks

6.1 Conclusion

Solution processed emitters, particularly conjugated polymers and organometal halide perovskites, have displayed promising properties in lighting applications. In this dissertation, both types of solution-processed emitters have been applied in light emitting devices with innovative device structures and have substantiated their ability to be used in large-area and low-cost optoelectronic applications.

In Chapter 2, a white conjugated polymer emitter was utilized in a flexible light emitting diode with high light out-coupling efficiency. The flexible nanocomposite electrode included silver nanowires embedded in the surface of the polymer substrate, while barium strontium titanate nanoparticles were uniformly dispersed in the polymer substrate. The nanoparticles served as the scattering center, which altered the emitted light propagation path inside the substrate, thereby increasing the light extraction efficiency. In addition, by replacing the ITO electrode with AgNW, light trapping due to refractive index mismatch was prevented. The white emissive polymer fabricated on the flexible nanocomposite electrode achieved a maximum external quantum efficiency of 27.3%, which is a 95% enhancement over the white PLED fabricated on the conventional ITO/glass substrate. The use of white conjugated polymers on the nanocomposite electrode paves the way for high-efficiency flexible PLEDs with low fabrication cost.

A new type of optoelectronic device, the OLET, was also fabricated using white conjugated polymers. In Chapter 3, a vertical organic light-emitting transistor made from electrolyte and porous aluminum electrode was demonstrated. The device combined a phosphorescent OLED and

a transistor with a capacitive electrolyte dielectric. The luminance of the device can be modified from 0.1 to 10,000 cd/m^2 by varying the gate potential (-6 V to 10 V). This strategy introduces new possibilities for fabricating highly integrated organic optoelectronic devices, as evidenced by a fully functional seven-segment display that employed this technology.

A second type of solution processed emitter, the perovskite, was also incorporated in the newly-introduced light emitting, touch-responsive device for instantaneous visualization of pressure mapping. In Chapter 4, the LETD, which integrated a perovskite-polymer composite emissive layer and a flexible AgNW-PU composite transparent electrode, was reported. The composite emissive layer contained methylammonium lead bromide ($MAPbBr_3$) nanocrystals uniformly dispersed in a polyethylene oxide (PEO) matrix; it emitted an intense green luminescence that peaked at 529 nm. When a local pressure was applied, a Schottky contact was formed instantaneously between the metal and the emissive layer, and electroluminescence was produced at voltages as low as 2.2 V and reached 1030 cd/m^2 at 6 V. The transparent LETD had approximately 60% transparency. It was able to be bent to a 6 mm radius when polyethylene terephthalate was used as the substrate. The pero LETD has a fast response and can be pixelated to offer new applications in robotics, motion detection, finger print devices, and interactive wallpapers.

The introduction of flexible electronics has brought a new contender to the world of optoelectronics, the stretchable optoelectronic. Chapter 5 presented a stretchable perovskite light-emitting diode that assimilated a stretchable AgNW-PU composite electrode and a stretchable composite perovskite emitter. By also incorporating a PEG polymer, perovskite growth was slowed and uniformly dispersed perovskite grains in the polymer matrix was possible. The PDMS matrix served as the interconnector between individual perovskite grains and provided

stretchability to the emissive film. The stretchable PeLED remained functional even when stretched to 60%. The discovery of these distinctive features exposes perovskite to countless stretchable light applications.

6.2 Outlook and Future Works

This dissertation has demonstrated the potential of both conjugated polymers and perovskites to be used in commercial lighting applications. Both types of emitters are attractive due to their color tunability ability to scale for large-area lighting applications, and their low manufacturing cost. However, material development is still needed- the current conjugated polymer emitters and perovskite emitters still have yet to achieve the same device performance as that of thermal vapor evaporated SMOLEDs. Solution-processed PLEDs usually have very simple device structures; this can be attributed to the fact that there are a limited number of materials that can withstand the solvent attack from the advancing layers. As a result, the charge injection of holes and electrons are larger than those of thermal evaporated OLEDs. Developing materials that can withstand solvent attacks after being cast into a film will be the next essential objective. One viable solution would be to cultivate cross-linking conjugated polymers which would be to resistant organic solvents.

The next generation of light emitting devices are not only trending towards flexible, but stretchable devices as well. Thus far, many works have reported flexible optoelectronics using both conjugated polymers and perovskite emitters; however, not many literatures have discussed stretchable light emitting devices. One reason for the lack of research on stretchable devices may be the predicament of the solvent attack on stretchable polymer materials. Polyurethane is a major polymer class that provides high stretchability; however, the solvents that are used to dissolve both

conjugated polymers and perovskite emitters are predominantly highly polar. The solvents with high polarity tend to break bonds in the polyurethane and result in substrate swelling. Therefore, developing emitters that can be dissolved in solvents that do not attack the polymer substrate is crucial for the future of display applications.

Reference

[1] C. Sekine, Y. Tsubata, T. Yamada, M. Kitano, S. Doi, *Sci. Technol. Adv. Mater.* **2014**, *15*, 34203.

[2] M. S. AlSalhi, J. Alam, L. A. Dass, M. Raja, *Int. J. Mol. Sci.* **2011**, *12*, 2036.

[3] X.-Y. Deng, *Int. J. Mol. Sci.* **2011**, *12*, 1575.

[4] Gong, X. (2013) Polymer Light-Emitting Diodes (PLEDs): Devices and Materials, in Organic Optoelectronics (ed W. Hu), Wiley-VCH Verlag GmbH & Co. KGaA, Weinheim, Germany. doi: 10.1002/9783527653454.ch5

[5] Lucas Fugikawa Santos and Giovani Gozzi (2016). Electrical Properties of Polymer Light-Emitting Devices, Conducting Polymers, Dr. Faris Yılmaz (Ed.), InTech, DOI: 10.5772/64358.

[6] Q. Chen, N. De Marco, Y. Yang, T. Bin Song, C. C. Chen, H. Zhao, Z. Hong, H. Zhou, Y. Yang, *Nano Today* **2015**, *10*, 355.

[7] M. A. Green, A. Ho-Baillie, H. J. Snaith, *Nat. Photonics* **2014**, *8*, 506.

[8] G. Kieslich, S. Sun, A. K. Cheetham, *Chem. Sci.* **2014**, *5*, 4712.

[9] D. B. Mitzi, *J. Chem. Soc. Dalt. Trans.* **2001**, 1.

[10] S. A. Veldhuis, P. P. Boix, N. Yantara, M. Li, T. C. Sum, N. Mathews, S. G. Mhaisalkar, *Adv. Mater.* **2016**, 28, 6804.

[11] B. R. Sutherland, E. H. Sargent, *Nat. Photonics* **2016**, *10*, 295.

[12] Q. A. Akkerman, V. D'Innocenzo, S. Accornero, A. Scarpellini, A. Petrozza, M. Prato, L. Manna, *J. Am. Chem. Soc.* **2015**, *137*, 10276.

[13] L. C. Schmidt, A. Pertegas, S. Gonzalez-Carrero, O. Malinkiewicz, S. Agouram, G. M.

Espallargas, H. J. Bolink, R. E. Galian, J. Perez-Prieto, *J. Am. Chem. Soc.* **2014**, *136*, 850.

[14] G. E. Eperon, V. M. Burlakov, P. Docampo, A. Goriely, H. J. Snaith, *Adv. Funct. Mater.* **2014**, *24*, 151.

[15] J. Burschka, N. Pellet, S.-J. Moon, R. Humphry-Baker, P. Gao, M. K. Nazeeruddin, M. Grätzel, *Nature* **2013**, *499*, 316.

[16] Y. Chen, M. He, J. Peng, Y. Sun, Z. Liang, *Adv. Sci.* **2016**, *3*, 1500392.

[17] M. M. Tavakoli, L. Gu, Y. Gao, C. Reckmeier, J. He, A. L. Rogach, Y. Yao, Z. Fan, *Sci. Rep.* **2015**, *5*, 14083.

[18] Y. Chen, Y. Zhao, Z. Liang, *Chem. Mater.* **2015**, *27*, 1448.

[19] X. Li, M. I. Dar, C. Yi, J. Luo, M. Tschumi, S. M. Zakeeruddin, M. K. Nazeeruddin, H. Han, M. Grätzel, *Nat. Chem.* **2015**, *7*, 703.

[20] A. Dualeh, N. Tétreault, T. Moehl, P. Gao, M. K. Nazeeruddin, M. Grätzel, *Adv. Funct. Mater.* **2014**, *24*, 3250.

[21] D. Liu, L. Wu, C. Li, S. Ren, J. Zhang, W. Li, L. Feng, *ACS Appl. Mater. Interfaces* **2015**, *7*, 16330.

[22] C. Y. Chang, C. Y. Chu, Y. C. Huang, C. W. Huang, S. Y. Chang, C. A. Chen, C. Y. Chao, W. F. Su, *ACS Appl. Mater. Interfaces* **2015**, *7*, 4955.

[23] J. Li, X. Shan, S. G. R. Bade, T. Geske, Q. Jiang, X. Yang, Z. Yu, *J. Phys. Chem. Lett.* **2016**, *7*, 4059.

[24] S. G. R. Bade, J. Li, X. Shan, Y. Ling, Y. Tian, T. Dilbeck, T. Besara, T. Geske, H. Gao, B. Ma, K. Hanson, T. Siegrist, C. Xu, Z. Yu, *ACS Nano* **2016**, *10*, 1795.

[25] G. Li, Z. K. Tan, D. Di, M. L. Lai, L. Jiang, J. H. W. Lim, R. H. Friend, N. C. Greenham, *Nano Lett.* **2015**, *15*, 2640.

[26] M. Anaya, J. F. Galisteo-Lopez, M. E. Calvo, C. Lopez, H. Miguez, *J. Phys. Chem. C* **2016**, *120*, 3071.

[27] H. Gao, C. Bao, F. Li, T. Yu, J. Yang, W. Zhu, X. Zhou, G. Fu, Z. Zou, *ACS Appl. Mater. Interfaces* **2015**, *7*, 9110.

[28] B. Geffroy, P. le Roy, C. Prat, *Polym. Int.* **2006**, *55*, 572.

[29] J. H. Burroughes, D. D. C. Bradley, A. R. Brown, R. N. Marks, K. Mackay, R. H. H. Friend, P. L. Burns, A. B. Holmes, *Nature* **1990**, *347*, 539.

[30] S. Hameed, P. Predeep, M. R. Baiju, T. I. 7u, S. Hameed, *Rev.Adv.Mater.Sci* **2010**, *26*, 30.

[31] P. Bocchiaro, A. Zamperini, *RFID Technol. Secur. Vulnerabilities, Countermeas.* **2016**, DOI 10.5772/711.

[32] Y.-H. Kim, H. Cho, T.-W. Lee, *Proc. Natl. Acad. Sci.* **2016**, *113*, 11694.

[33] Y. H. Kim, H. Cho, J. H. Heo, T. S. Kim, N. S. Myoung, C. L. Lee, S. H. Im, T. W. Lee, *Adv. Mater.* **2015**, *27*, 1248.

[34] A. Hepp, H. Heil, W. Weise, M. Ahles, R. Schmechel, H. von Seggern, *Phys. Rev. Lett.* **2003**, *91*, 157406.

[35] J. S. Swensen, J. Yuen, D. Gargas, S. K. Buratto, A. J. Heeger, *J. Appl. Phys.* **2007**, *102*, 013103.

[36] C. Zhang, P. Chen, W. Hu, *Small* **2016**, *12*, 1252.

[37] Muccini, Michele, and Stefano Toffanin. *Organic Light-Emitting Transistors towards the next Generation Display Technology*. Wiley Blackwell, 2016.

[38] J. Veres, S. Ogier, G. Lloyd, D. De Leeuw, *Chem. Mater.* **2004**, *16*, 4543.

[39] J. T. Ye, S. Inoue, K. Kobayashi, Y. Kasahara, H. T. Yuan, H. Shimotani, Y. Iwasa, *Nat. Mater.* **2010**, *9*, 125.

[40] M. C. Gwinner, F. Jakubka, F. Gannott, H. Sirringhaus, **2012**, *1*, 1.

[41] B. B. Y. Hsu, C. Duan, E. B. Namdas, A. Gutacker, J. D. Yuen, F. Huang, Y. Cao, G. C. Bazan, I. D. W. Samuel, A. J. Heeger, *Adv. Mater.* **2012**, *24*, 1171.

[42] R. Capelli, S. Toffanin, G. Generali, H. Usta, A. Facchetti, M. Muccini, *Nat. Mater.* **2010**, *9*, 496.

[43] M. C. Gather, A. Köhnen, K. Meerholz, *Adv. Mater.* **2011**, *23*, 233.

[44] M. Thomschke, R. Nitsche, M. Furno, K. Leo, **2009**, 94, 083303.

[45] R. H. Friend, R. W. Gymer, A. B. Holmes, J. H. Burroughes, R. N. Marks, C. Taliani, D. D. C. Bradley, D. A. Dos Santos, J. L. Bredas, M. Logdlund, W. R. Salaneck, *Nature* **1999**, *397*, 121.

[46] H. Wu, J. Zou, F. Liu, L. Wang, A. Mikhailovsky, G. C. Bazan, W. Yang, Y. Cao, *Adv. Mater.* **2008**, *20*, 696.

[47] J. Liang, L. Li, X. Niu, Z. Yu, Q. Pei, *Nat. Photonics* **2013**, *7*, 817.

[48] S. Reineke, F. Lindner, G. Schwartz, N. Seidler, K. Walzer, B. Lüssem, K. Leo, *Nature* **2009**, *459*, 234.

[49] E. L. Williams, K. Haavisto, J. Li, G. E. Jabbour, *Adv. Mater.* **2007**, *19*, 197.

[50] L. Xiao, S. J. Su, Y. Agata, H. Lan, J. Kido, *Adv. Mater.* **2009**, *21*, 1271.

[51] C. Adachi, M. A. Baldo, M. E. Thompson, S. R. Forrest, *J. Appl. Phys.* **2001**, *90*, 5048.

[52] K. Leo, *Nat. Photonics* **2011**, *5*, 716.

[53] K. Hong, J.-L. Lee, *Electron. Mater. Lett.* **2011**, *7*, 77.

[54] W. H. Koo, S. M. Jeong, F. Araoka, K. Ishikawa, S. Nishimura, T. Toyooka, H. Takezoe, *Nature Photonics* **2010**, *4*, 222.

[55] M. C. Gather, S. Reineke, *J. Photon. Energy* **2015**, *5*, 57607.

[56] Y. Sun, S. R. Forrest, *J. Appl. Phys.* **2006**, *100*, 73106.

[57] Y. Sun, S. R. Forrest, *Nat. Photonics* **2008**, *2*, 483.

[58] B. K. Hong, H. K. Yu, I. Lee, K. Kim, S. Kim, J. Lee, *Adv. Mater.* **2010**, *22*, 4890.

[59] W. H. Koo, S. M. Jeong, S. Nishimura, F. Araoka, K. Ishikawa, T. Toyooka, H. Takezoe, *Adv. Mater.* **2011**, *23*, 1003.

[60] W. Brütting, J. Frischeisen, T. D. Schmidt, B. J. Scholz, C. Mayr, *Phys. Status Solidi* **2013**, *210*, 44.

[61] M. Thomschke, R. Nitsche, M. Furno, K. Leo, *Appl. Phys. Lett.* **2009**, *94*, 83303.

[62] S. Nanowire, L. Hu, H. S. Kim, J. Lee, P. Peumans, Y. Cui, **2010**, *4*, 2955.

[63] J.-Y. Lee, S. T. Connor, Y. Cui, P. Peumans, *Nano Lett.* **2008**, *8*, 689.

[64] L. Li, J. Liang, S.-Y. Chou, X. Zhu, X. Niu, ZhibinYu, Q. Pei, *Sci. Rep.* **2014**, *4*, 4307.

[65] A. Chutinan, K. Ishihara, T. Asano, M. Fujita, S. Noda, *Org. Electron.* **2005**, *6*, 3.

[66] J. L. Young, R. O. Nelson, *IEEE Antennas Propag. Mag.* **2001**, *43*, 61.

[67] J. Kim, J. Jang, M. Oh, J. Shin, D. Cho, J. Moon, J. Lee, *Opt. Express* **2014**, *22*, 711.

[68] Y. R. Do, Y. C. Kim, Y.-W. Song, C.-O. Cho, H. Jeon, Y.-J. Lee, S.-H. Kim, Y.-H. Lee, *Adv. Mater.* **2003**, *15*, 1214.

[69] I. D. Parker, *J. Appl. Phys.* **1994**, *75*, 1656.

[70] K. T. Kamtekar, A. P. Monkman, M. R. Bryce, *Adv. Mater.* **2010**, *22*, 572.

[71] T. J. Pounds, R. J. Wilson, I. Grizzi, T. Yamada, *SID Symposium Digest* **2007**, 38, 875.

[72] F. I. Wu, X. H. Yang, D. Neher, R. Dodda, Y. H. Tseng, C. F. Shu, *Adv. Funct. Mater.* **2007**, *17*, 1085.

[73] S. Wang, B. Zhang, X. Wang, J. Ding, Z. Xie, L. Wang, *Adv. Opt. Mater.* **2015**, *3*, 1349.

[74] J. Liang, L. Ying, F. Huang, Y. Cao, *J. Mater. Chem. C* **2016**, *4*, 10993.

[75] J. Liang, S. Zhao, X. F. Jiang, T. Guo, H. L. Yip, L. Ying, F. Huang, W. Yang, Y. Cao, *ACS Appl. Mater. Interfaces* **2016**, *8*, 6164.

[76] J. Liang, Z. Zhong, S. Li, X.-F. Jiang, L. Ying, W. Yang, J. Peng, Y. Cao, *J. Mater. Chem. C* **2017**, *5*, 2397.

[77] Y. Z. Lee, X. Chen, M. C. Chen, S. A. Chen, J. H. Hsu, W. Fann, *Appl. Phys. Lett.* **2001**, *79*, 308.

[78] M. L. Tsai, C. Y. Liu, M. A. Hsu, T. J. Chow, *Appl. Phys. Lett.* **2003**, *82*, 550.

[79] G. K. Ho, H. F. Meng, S. C. Lin, S. F. Homg, C. S. Hsu, L. C. Chen, S. M. Chang, *Appl. Phys. Lett.* **2004**, *85*, 4576.

[80] Y. M. Wang, F. Teng, Z. Xu, Y. B. Hou, S. Y. Yang, L. Qian, T. Zhang, D. A. Liu, *Appl. Surf. Sci.* **2004**, *236*, 251.

[81] S. P. Singh, Y. N. Mohapatra, M. Qureshi, S. Sundar Manoharan, *Appl. Phys. Lett.* **2005**, *86*, 113505.

[82] T. Ye, J. Chen, D. Ma, *Phys. Chem. Chem. Phys.* **2010**, *12*, 15410.

[83] F. P. Chen, B. Xu, Z. J. Zhao, W. J. Tian, P. Lu, I. Chan, *Chinese Phys. B* **2010**, *19*, 37801.

[84] L. Wen, F. Li, J. Xie, C. Wu, Y. Zheng, D. Chen, S. Xu, T. Guo, B. Qu, Z. Chen, Q. Gong, *J. Lumin.* **2011**, *131*, 2252.

[85] L.-C. Meng, Z.-D. Lou, S.-Y. Yang, Y.-B. Hou, F. Teng, X.-J. Liu, Y.-B. Li, *Chinese Phys. B* **2012**, *21*, 88504.

[86] D. G. Georgiadou, L. C. Palilis, M. Vasilopoulou, G. Pistolis, D. Dimotikali, P. Argitis, *RSC Adv.* **2012**, *2*, 11786.

[87] J. Kalinowski, G. Giro, M. Cocchi, V. Fattori, P. Di Marco, *Appl. Phys. Lett.* **2000**, *76*, 2352.

[88] J. Y. Li, D. Liu, C. Ma, O. Lengyel, C. S. Lee, C. H. Tung, S. Lee, *Adv. Mater.* **2004**, *16*,

1538.

[89] X. Xu, G. Yu, C. Di, Y. Liu, K. Shao, L. Yang, P. Lu, *Appl. Phys. Lett.* **2006**, *89*, 1.

[90] J. Kalinowski, M. Cocchi, D. Virgili, V. Fattori, J. A. G. Williams, *Adv. Mater.* **2007**, *19*, 4000.

[91] Z. Zhao, B. Xu, Z. Yang, H. Wang, X. Wang, P. Lu, W. Tian, *J. Phys. Chem. C* **2008**, *112*, 8511.

[92] S. Yang, M. Jiang, *Chem. Phys. Lett.* **2009**, *484*, 54.

[93] H. Zhu, Z. Xu, F. Zhang, S. Zhao, Z. Wang, D. Song, *Synth. Met.* **2009**, *159*, 2458.

[94] S. Wu, S. Li, Q. Sun, C. Huang, M.-K. Fung, *Sci. Rep.* **2016**, *6*, 25821.

[95] E. Angioni, M. Chapran, K. Ivaniuk, N. Kostiv, V. Cherpak, P. Stakhira, A. Lazauskas, S. Tamulevičius, D. Volyniuk, N. J. Findlay, T. Tuttle, J. V. Grazulevicius, P. J. Skabara, *J. Mater. Chem. C* **2016**, *4*, 3851.

[96] Z. Zhang, G. Li, Y. M. Jiacong Shen, *Mater. Chem. Phys.* **2003**, *82*, 613.

[97] Y. M. Wang, F. Teng, Z. Xu, Y. B. Hou, Y. S. Wang, X. R. Xu, *Appl. Surf. Sci.* **2005**, *243*, 355.

[98] M. Wei, G. Gui, Y. H. Chung, L. Xiao, B. Qu, Z. Chen, *Phys. Status Solidi Basic Res.* **2015**, *252*, 1711.

[99] J. Kalinowski, M. Cocchi, P. Di Marco, W. Stampor, G. Giro, V. Fattori, *J. Phys. D Appl. Phys.* **2000**, *33*, 2379.

[100] D. W. Zhao, Z. Xu, F. J. Zhang, S. F. Song, S. L. Zhao, Y. Wang, G. C. Yuan, Y. F. Zhang, H. H. Xu, *Appl. Surf. Sci.* **2007**, *253*, 4025.

[101] J. Liu, D. Chen, X. Luan, K. Tong, F. Zhao, C. Liu, Q. Pei, H. Li, *ACS Appl. Mater. Interfaces* **2017**, *9*, 12647.

[102] Y. Xiong, L. Li, J. Liang, H. Gao, S. Chou, Q. Pei, *Mater. Horiz.* **2015**, *2*, 338.

[103] Q. Pei, Y. Yang, *Chem. Soc.* **1996**, *118*, 7416.

[104] Y. Yang, Q. Pei, *J. Appl. Phys.* **1997**, *81*, 3294.

[105] A. Calzolari, B. Vercelli, A. Ruini, T. Virgili, M. Pasini, *J. Phys. Chem. C* **2013**, *117*, 26760.

[106] C. Chu, J. Ha, J. Choi, S. Lee, J. Rhee, D. Lee, J. Chung, H. Kim, K. Chung, *Advances* **2007**, 1118.

[107] Y. Cao, I. D. Parker, G. Yu, C. Zhang, a J. Heeger, *Nature* **1999**, *397*, 414.

[108] P. K. H. Ho, J.-S. Kim, J. H. Burroughes, H. Becker, S. F. Y. Li, T. M. Brown, F. Cacialli, R. H. Friend, *Nature* **2000**, *404*, 481.

[109] S. H. Kim, K. Hong, W. Xie, K. H. Lee, S. Zhang, T. P. Lodge, C. D. Frisbie, *Adv. Mater.* **2013**, *25*, 1822.

[110] T. Leijtens, G. E. Eperon, N. K. Noel, S. N. Habisreutinger, A. Petrozza, H. J. Snaith, *Adv. Energy Mater.* **2015**, *5*, 1.

[111] C. Hoven, R. Yang, A. Garcia, A. J. Heeger, T. Q. Nguyen, G. C. Bazan, *J. Am. Chem. Soc.* **2007**, *129*, 10976.

[112] K. Ueno, S. Nakamura, H. Shimotani, a Ohtomo, N. Kimura, T. Nojima, H. Aoki, Y. Iwasa, M. Kawasaki, *Nat. Mater.* **2008**, *7*, 855.

[113] X. Xu, G. Yu, Y. Ma, K. Shao, L. Yang, Y. Liu, *J. Lumin.* **2013**, *136*, 208.

[114] Q. Pei, G. Yu, C. Zhang, Y. Yang, A. J. Heeger, *Science* **1995**, *269*, 1086.

[115] P. Matyba, K. Maturova, M. Kemerink, N. D. Robinson, L. Edman, *Nat. Mater.* **2009**, *8*, 672.

[116] S. Gong, W. Schwalb, Y. Wang, Y. Chen, Y. Tang, J. Si, B. Shirinzadeh, W. Cheng, *Nat. Commun.* **2014**, *5*, 3132.

[117] T. Q. Trung, N. E. Lee, *Adv. Mater.* **2016**, *28*, 4338.

[118] S. Y. Kim, S. Park, H. W. Park, D. H. Park, Y. Jeong, D. H. Kim, *Adv. Mater.* **2015**, *27*, 4178.

[119] M. I. Tiwana, S. J. Redmond, N. H. Lovell, *Sensors Actuators, A Phys.* **2012**, *179*, 17.

[120] R. Ma, M. M. Menamparambath, P. Nikolaev, S. Baik, *Adv. Mater.* **2013**, *25*, 2548.

[121] C. Wang, D. Hwang, Z. Yu, K. Takei, J. Park, T. Chen, B. Ma, a Javey, *Nat Mater* **2013**, *12*, 899.

[122] H. Cho, S. Jeong, M. Park, Y. Kim, C. Wolf, C. Lee, J. H. Heo, A. Sadhanala, N. Myoung, S. Yoo, S. H. Im, R. H. Friend, T. Lee, **2015**, *350*, 1222.

[123] P. Docampo, T. Bein, *Acc. Chem. Res.* **2016**, *49*, 339.

[124] H. Cho, S.-H. Jeong, M.-H. Park, Y.-H. Kim, C. Wolf, C.-L. Lee, J. H. Heo, A. Sadhanala, N. Myoung, S. Yoo, S. H. Im, R. H. Friend, T.-W. Lee, *Science* **2015**, *350*, 1222.

[125] S. D. Stranks, H. J. Snaith, *Nat. Nanotechnol.* **2015**, *10*, 391.

[126] Y. H. Kahng, M.-K. Kim, J.-H. Lee, Y. J. Kim, N. Kim, D.-W. Park, K. Lee, *Sol. Energy Mater. Sol. Cells* **2014**, *124*, 86.

[127] Z.-K. Tan, R. S. Moghaddam, M. L. Lai, P. Docampo, R. Higler, F. Deschler, M. Price, A. Sadhanala, L. M. Pazos, D. Credgington, F. Hanusch, T. Bein, H. J. Snaith, R. H. Friend, *Nat. Nanotechnol.* **2014**, *9*, 1.

[128] J. Li, S. G. R. Bade, X. Shan, Z. Yu, *Adv. Mater.* **2015**, *27*, 5196.

[129] Z. Yu, L. Li, Q. Zhang, W. Hu, Q. Pei, *Adv. Mater.* **2011**, *23*, 4453.

[130] W. Hu, X. Niu, L. Li, S. Yun, Z. Yu, Q. Pei, *Nanotechnology* **2012**, *23*, 344002.

[131] Z. Yu, Q. Zhang, L. Li, Q. Chen, X. Niu, J. Liu, Q. Pei, *Adv. Mater.* **2011**, *23*, 664.

[132] H. Dong, Y. Li, S. Wang, W. Li, N. Li, X. Guo, L. Wang, *J. Mater. Chem. A* **2015**, *3*, 9999.

[133] Y. Zhao, J. Wei, H. Li, Y. Yan, W. Zhou, D. Yu, Q. Zhao, *Nat. Commun.* **2016**, *7*, 10228.

[134] X. Zhang, H. Lin, H. Huang, C. Reckmeier, Y. Zhang, W. C. H. Choy, A. L. Rogach, *Nano Lett.* **2016**, *16*, 1415.

[135] Z. Shi, Y. Li, Y. Zhang, Y. Chen, X. Li, D. Wu, T. Xu, C. Shan, G. Du, *Nano Lett.* **2017**, *17*, 313.

[136] J. A. Lee, Y. R. Lim, C. S. Jung, J. H. Choi, H. S. Im, K. Park, J. Park, G. T. Kim, *Nanotechnology* **2016**, *27*, 425711.

[137] A. J. Chiquito, C. A. Amorim, O. M. Berengue, L. S. Araujo, E. P. Bernardo, E. R. Leite, *J. Phys. Condens. Matter* **2012**, *24*, 225303.

[138] X. D. Feng, C. J. Huang, V. Lui, R. S. Khangura, Z. H. Lu, *Appl. Phys. Lett.* **2005**, *86*, 1.

[139] H. Chen, S. Yang, *Adv. Mater.* **2017**, DOI 10.1002/ADMA.201603994.

[140] J. Osvald, *Phys. Status Solidi Appl. Mater. Sci.* **2015**, *212*, 2754.

[141] J. Woo, H. Hwang, *ECS J. Solid State Sci. Technol.* **2016**, *5*, Q188.

[142] W. D. Nix, *Metall. Trans. A* **1989**, *20*, 2217.

[143] R. H. Kim, M. H. Bae, D. G. Kim, H. Cheng, B. H. Kim, D. H. Kim, M. Li, J. Wu, F. Du, H. S. Kim, S. Kim, D. Estrada, S. W. Hong, Y. Huang, E. Pop, J. A. Rogers, *Nano Lett.* **2011**, *11*, 3881.

[144] J. Viventi, D.-H. Kim, J. D. Moss, Y.-S. Kim, J. A. Blanco, N. Annetta, A. Hicks, J. Xiao, Y. Huang, D. J. Callans, J. A. Rogers, B. Litt, *Sci. Transl. Med.* **2010**, *2*, 24ra22.

[145] T. Someya, *Nat. Mater.* **2010**, *9*, 879.

[146] H. L. Filiatrault, G. C. Porteous, R. S. Carmichael, G. J. E. Davidson, T. B. Carmichael, *Adv. Mater.* **2012**, *24*, 2673.

[147] J. Liang, L. Li, D. Chen, T. Hajagos, Z. Ren, S.-Y. Chou, W. Hu, Q. Pei, *Nat. Commun.*

2015, *6*, 7647.

[148] S. Choi, H. Lee, R. Ghaffari, T. Hyeon, D. H. Kim, *Adv. Mater.* **2016**, *28*, 4203.

[149] W. Gao, S. Emaminejad, H. Y. Y. Nyein, S. Challa, K. Chen, A. Peck, H. M. Fahad, H. Ota, H. Shiraki, D. Kiriya, D.-H. Lien, G. A. Brooks, R. W. Davis, A. Javey, *Nature* **2016**, *529*, 509.

[150] L. D. Deformable, S. Park, Y. Xiong, R. Kim, P. Elvikis, M. Meitl, D. Kim, J. Wu, J. Yoon, C. Yu, Z. Liu, Y. Huang, K. Hwang, P. Ferreira, X. Li, K. Choquette, J. A. Rogers, *Science* **2009**, *325*, 977.

[151] T. Sekitani, H. Nakajima, H. Maeda, T. Fukushima, T. Aida, K. Hata, T. Someya, *Nat. Mater.* **2009**, *8*, 494.

[152] M. S. White, M. Kaltenbrunner, E. D. Głowacki, K. Gutnichenko, G. Kettlgruber, I. Graz, S. Aazou, C. Ulbricht, D. a. M. Egbe, M. C. Miron, Z. Major, M. C. Scharber, T. Sekitani, T. Someya, S. Bauer, N. S. Sariciftci, *Nat. Photonics* **2013**, *7*, 811.

[153] D. Yin, J. Feng, R. Ma, Y.-F. Liu, Y.-L. Zhang, X.-L. Zhang, Y.-G. Bi, Q.-D. Chen, H.-B. Sun, *Nat. Commun.* **2016**, *7*, 11573.

[154] Z. Yu, X. Niu, Z. Liu, Q. Pei, *Adv. Mater.* **2011**, *23*, 3989.

[155] S. G. R. Bade, X. Shan, P. T. Hoang, J. Li, T. Geske, L. Cai, Q. Pei, C. Wang, Z. Yu, *Adv. Mater.* **2017**, *29*, 1.